

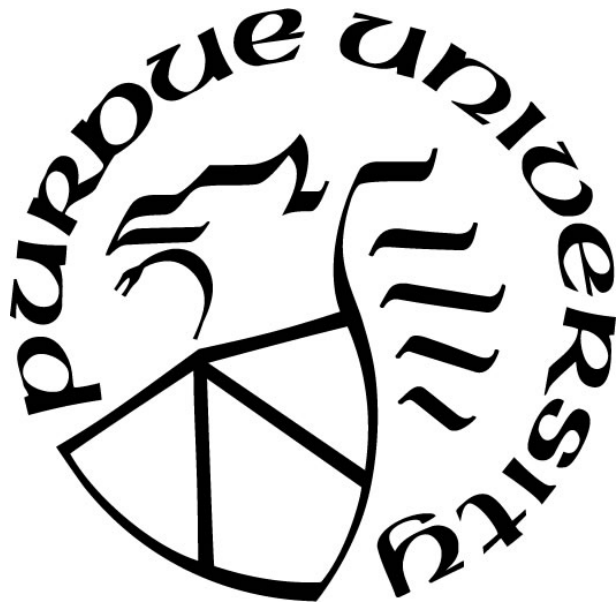
**COMBINED PHYSICS AND BMP SIGNALING NETWORK DYNAMICS
TO MODEL EARLY EMBRYONIC DEVELOPMENT IN ZEBRAFISH**

by
Linlin Li

A Dissertation

*Submitted to the Faculty of Purdue University
In Partial Fulfillment of the Requirements for the degree of*

Doctor of Philosophy



Weldon School of Biomedical Engineering

West Lafayette, Indiana

May 2021

**THE PURDUE UNIVERSITY GRADUATE SCHOOL
STATEMENT OF COMMITTEE APPROVAL**

Dr. David M. Umulis, Chair

Department of Agricultural and Biological Engineering
Weldon School of Biomedical Engineering

Dr. Adrian Buganza-Tepole

School of Mechanical Engineering
Weldon School of Biomedical Engineering

Dr. Tamara Kinzer-Ursem

Weldon School of Biomedical Engineering

Dr. Qing Deng

Department of Biological Sciences

Dr. Taeyoon Kim

Weldon School of Biomedical Engineering

Approved by:

Dr. George R. Wodicka

To my Mom, Congqing Feng
To my Dad, Lu Li
To my Husband, Jungmo Yang
who encouraged me to pursue my dream

To my boys, Logan and Dylan Yang

ACKNOWLEDGMENTS

First and foremost, I would like to express my sincere gratitude and appreciation to my advisor and committee chair Professor David M. Umulis for his professional guidance, full support, patience, motivation, kindness, and immense knowledge. His guidance helped me in all the time of research and writing of this thesis. He is not only an inspiring mentor but also a caring friend, who kept me on the right track and helped me grow both professionally and personally. I could not have imagined having a better advisor and mentor for my Ph.D. study.

Besides my advisor, I would like to thank the rest of my thesis committee. Prof. Adrian Buganza-Tepole guided me through the construction of the FEM model, patiently answered questions, and without his help I wouldn't have been able to finish the model. Additionally, Prof. Tamara Kinzer-Ursem, Prof. Qing Deng, and Prof. Taeyoon Kim provided valuable time and insightful comments and encouragement, and I am also grateful for the hard questions which incited me to widen my research from various perspectives. Also, I would like to thank the staff at the Weldon School of Biomedical Engineering especially Tammy Siemers and Sandra May, for everything they do to support students.

I would like to thank all the former and current members of our lab, particularly those who worked closely with me and gave valuable advice on the projects presented in this dissertation, including Dr. Xu Wang, Dr. Xiaoguang Zhu, Dr. Aasakiran Madamanchi, Dr. Yan Huang, Dr. Joyattee Sarker, Dr. Nimisha Bajaj, Dr. Ye Bu, Dr. Thembi Mdluli, Dr. Tzu-Ching Wu, Yan Luo, Lukasz Burzawa, Juan Andres Carvajal, Michelle Ingle, and Yixuan Liu, especially, Matthew Thompson, for all his good pieces of advice, kind help, and support during our paralleled Ph.D. time.

Last but not the least, I would like to thank my family: my Mom Congqing Feng and Dad Lu Li, for all their support to let their only daughter pursue her dream without any hesitation, my husband Jungmo Yang, for taking care of our twin sons through writing this thesis, and my sons Logan and Dylan who were born in the first year of my program, going all the way with me through this tough path and supporting me spiritually.

PREFACE

Two chapters of this dissertation (Chapter 3 and Chapter 4) have been published in peer-reviewed journals as noted at the start of the chapter. Minor changes in formatting and wording have been made for cohesive writing purposes.

TABLE OF CONTENTS

LIST OF TABLES	8
LIST OF FIGURES.....	9
ABSTRACT	13
1 INTRODUCTION.....	15
1.1 Early-stage Zebrafish embryo development.....	16
1.2 Bone morphogenetic proteins (BMPs) and Dorsal-Ventral (DV) patterning.....	17
1.3 Extracellular regulation of BMP	21
1.4 Mathematical Modeling of Pattern Formation	25
1.5 Scaling invariance in Zebrafish embryo.....	30
2 QUANTIFYING SPATIOTEMPORAL BMP SIGNALING, FEEDBACK TARGET GENE EXPRESSION IN ZEBRAFISH BLASTULA AND GASTRULA EMBRYOS	32
2.1 Quantifying spatiotemporal cell movement	32
2.1.1 Diffusion vs Advection	34
2.1.2 Apply cell movement map to finite element model	36
2.2 Quantification of Spatiotemporal P-Smad image data	38
2.3 Quantification of Spatiotemporal target gene expression with whole-mount mRNA scope experimental data.....	42
3 EVALUATION OF BMP-MEDIATED PATTERNING IN A 3D MATHEMATICAL MODEL OF THE ZEBRAFISH BLASTULA EMBRYO	48
3.1 Introduction	48
3.2 Method.....	51
3.3 Results	56
3.4 Discussion.....	62
4 ACCELERATION OF PDE-BASED BIOLOGICAL SIMULATION THROUGH THE DEVELOPMENT OF NEURAL NETWORK METAMODELS	64
4.1 Introduction	64
4.2 Machine learning and deep learning.....	66
4.3 Applications of machine learning to mathematical modeling	68
4.4 Mathematical modeling in developmental biology	71
4.5 Application on PDE acceleration through neural networks	75
4.6 Results	77

5	FINITE ELEMENT GROWING DOMAIN MODEL OF BMP-MEDIATED SIGNALING IN ZEBRAFISH EMBRYO	83
5.1	Methods	83
5.1.1	Remeshing scheme	84
5.1.2	FEM formula for convection-diffusion-reaction system.....	85
5.1.3	Finite element approximation.....	86
5.1.4	Governing equations.....	88
5.1.5	Model validation.....	90
5.2	Result.....	90
5.2.1	Wild type parameter screening.....	91
5.2.2	Domain change and advection play a role in BMP gradient formation	95
5.2.3	Examination the scaling invariance in BMP gradients formation along dorsal-ventral axis	97
5.2.4	Comparison of Finite difference approach and Finite Element approach	100
5.3	Discussion.....	102
6	CONCLUSION AND FUTURE WORK.....	104
6.1	Conclusion.....	104
6.2	Future Work.....	105
6.2.1	Stochastic study of downstream gene transcription with BMP signaling regulation.....	105
6.2.2	Combined with mechanics during epiboly.....	107
	APPENDIX A. SUPPLEMENTAL TO CHAPTER 2.....	110
	APPENDIX B. SUPPLEMENTAL FIGURES/TABLE.....	111
	REFERENCES.....	117
	PUBLICATIONS	129

LIST OF TABLES

Table 1.1. BMP signaling related mutants and phenotypes in zebrafish.....	20
Table 1.2. Major extracellular regulators of BMP signaling in zebrafish embryo.....	24
Table 3.1. List of the parameter ranges used in the computational model-based screen. Values range between the upper and lower bound.	56
Table 4.1. Comparing MLP models	77
Table 4.2. Comparing LSTM models.....	78
Table 5.1. Remeshing scheme	85

LIST OF FIGURES

Figure 1.1. Epiboly process in the zebrafish embryo adapted from [15] d, dorsal; dc, deep cells; dcm, deep cell margin; e-ysn, external yolk syncytial nuclei; ep, epiblast; hyp, hypoblast; i-ysn, internal yolk syncytial nuclei; vp, vegetal pole; yc, yolk cell. Black arrows show the general cell movement direction. Deep cells are shown in white, the EVL and YSL in blue and the yolk cells are shown in yellow.	16
Figure 1.2. Illustration of BMP signaling pathway, adapted from J. A. Dutko and M. C. Mullins [26]	18
Figure 1.3. A-F Mutants of dorsalization strength from C1 to C5 according to their strength, with 1 being the weakest and 5 the strongest. The strength of the phenotype is based on the degree to which the notochord, somites, and tail are affected. G, Ventrlazation mutant (picture adapted from Mullins (1996) [33] and Little (2004) [38])	19
Figure 1.4. BMP gradient distribution and potential mechanism of BMP modulators in zebrafish embryo. [blue box (BMP), red box (inhibitor), green box (activator), green/red box (inhibitor/activator), redline (inhibition), green line (promotion), green/red line (inhibition/activation), dashed line (potential interaction)].	21
Figure 1.5. French flag model	26
Figure 2.1. Cell movement trace fitting during epiboly, (A) Individual Cell traces map on the sphere, (B) Smoothed cell trace, (C) Overall cell movement map.....	33
Figure 2.2. Cell velocity map of velocity components on azimuth (A) and elevation (B) direction during epiboly. Use the azimuth angle, az, and the elevation angle, el, to define the spherical coordinates.....	34
Figure 2.3. Cell trace map on elevation (el) and azimuth (az) direction around 50% epiboly (A: 4.7-5.3 hpf) and 90% epiboly (B: 5.7-9hpf), color represents the Péclet number based on the cell velocity calculated every 15 min. hpf: hours post fertilization. 0 on the az axis represents the ventral end.	35
Figure 2.4 Lowess fit of the averaged velocity data. v1, velocity on x direction, v2, velocity on y direction, v4, velocity on z direction. v4, velocity magnitude.	36
Figure 2.5. Generation processes of the 3D dynamic cell velocity map at different stages. Column A represents the real cell movement data mapped onto a spherical surface. Column B represents the averaged spontaneous velocity on an evenly distributed point cloud over the surface. Column C represents the functionally fitted and smoothed 3D dynamic cell velocity map based on spherical coordinate. Column D shows the finite element mesh movement guided by the dynamic cell velocity map.	37
Figure 2.6. Data processing steps for P-Smad data. Color level indicates the intensity level at arbitrary unit.	39

Figure 2.7. Averaged P-Smad distribution for wild-type at 4.7hpf, 5.3hpf, 5.7hpf, 6.3hpf and 6.7hpf.....	40
Figure 2.8. Averaged P-Smad distribution for chd mutant at 4.7hpf, 5.3hpf, 5.7hpf, and 6.3hpf.....	40
Figure 2.9. P-Smad profile at the margin for wild-type and Chd mutant.....	41
Figure 2.10. P-Smad profile at central for wild-type and Chd mutant	41
Figure 2.11. Whole-mount RNAscope image of bmp2b, chordin, and sizzled mRNA distribution.	43
Figure 2.12. mRNA identification and noise of image processing scheme of the whole mount RNAscope experimental image. A. Original confocal image on a specific z-stack. B. mRNAs identified through hold method on a same z-stack. C. mRNAs identified over 3D space with noise D. Noise (Red) clearing process E. Noise cleaned data	44
Figure 2.13. Embryo data registration for blastula and gastrula stages.....	45
Figure 2.14. Averaged mRNA expression map for different proteins at individual development stages	46
Figure 2.15. Dynamic expression map interpolated on FEM mesh. A, expression map for bmp2b mRNA at 4.7hpf on spherical grid. B, Interpolated expression level of BMP on FEM mesh.	47
Figure 3.1. Whole mount experimental result of bmp2b (A), chd (B), nog (C) mRNA expression and nucleus positions (D), view from the animal pole. (E-G) Simulation input of expression area in WT for BMP, Chd and Nog, respectively. Yellow color indicates an area of production for each species. (H) Simplified BMP regulatory network used in this study.	52
Figure 3.2. (A) Spatial domain at 3.5 hpf, Red open edges represent the non-flux boundary condition. (B) Initial domain (blue) vs later stage embryo domain (orange). Here we illustrate a 14 (elevation) by 31 (azimuth) initial mesh that requires 7 growth steps from 30% to 50% epiboly. (C) Finite difference discretization.....	54
Figure 3.3. A, A' and A'', Normalized simulation result of a wild type case at 4.7 hpf, 5.3 hpf, and 5.7 hpf. B, B' and B'', Averaged and normalized P-Smad5 profile of 4.7 hpf, 5.3 hpf, and 5.7 hpf embryos. C, C' and C'', Relative differences between simulation results and P-Smad5 level. Positive error indicates the experimental data are higher than simulation results, negative error indicates the experimental data are lower than simulation results. The results show in this figure illustrated with 9x15 mesh in the initial domain.	57
Figure 3.4. BMP distribution of a single modeling simulation result compared with the P-Smad 5 profile. A, WT case profile in the margin region. B, WT case profile in the central region. C, Chordin LOF case on margin region. D, Chordin LOF case on the central region. All graphs are from ventral to dorsal as indicated below x-axis in C, D. Black color represents 4.7 hpf, Blue color represents 5.3 hpf, Red color represents 5.7 hpf. The shaded region indicates standard deviation for individual experimental data, represented by the dotted line. The x-axis indicates the radial position.	59
Figure 3.5. Local sensitivity analysis for unknown parameters. A, the production rate for BMP, Chd, and Nog. B, the Decay rate for Nog, BMP-Chd complex, and BMP-Nog complex. C,	

Diffusivity of Nog, BMP-Chd complex, and BMP-Nog complex. D, Tld processing rate of Chd and BMP-Chd complex (1/s), 2nd order constant for BMP/Chd (k1) and BMP/Nog (k2) (1/nM·s). For Figure A-D, the x-axis represents the parameters' value in the log scale. The y-axis represents the error of the simulation result for the normalized BMP ligand concentration compared to the normalized experimental P-Smad intensity. E, Relative maximum BMP concentration changes as secretion domains change with BMP, Chd, and Nog. The X-axis represents the proportion of secretion domain vs embryo length (SD/L). F. Normalized BMP profile at the margin and central line changed by a proportional range of BMP secretion. G. Normalized BMP profile on margin and central line changed by a proportional range of Chd secretion. X-axis represents the radial position from Ventral (left) to Dorsal (right). The Red line indicates a wider range of BMP or Chd secretion, respectively.62

Figure 4.1 PDE modeling (blue) and meta-modeling (yellow)66

Figure 4.2 MLP vs LSTM model architecture68

Figure 4.3 Illustration of the 1D vs 3D approach of PDE simulations on BMP concentration profile on Margin region/whole embryo region73

Figure 4.4 Comparison of protein distributions obtained by direct PDE simulation, MLP metamodel and LSTM metamodel plotted over the 1D domain parameterized by the nondimensional x coordinate, with $x = 0$ (0 micrometer) the ventral end and $x = 35$ (700 micrometers) the dorsal end on margin.79

Figure 4.5 Comparison of RMSD distribution among 70,000 validation MLP metamodel and LSTM metamodel80

Figure 4.6 Comparison between simulation and NN model of 3D growing domain model results with MLP model81

Figure 5.1. Flow chart of FEM model construction84

Figure 5.2. Surface mapping88

Figure 5.3. FEM model validation with COMSOL90

Figure 5.4. Finite elements simulation results in reflex of expression region obtain from mRNA expression map, concentrations for different species (BMP, Chd, BC, Nog, BC complex, BN complex and Sizzled) normalized individually.91

Figure 5.5. Column A, Averaged and normalized P-Smad5 profile at 4.7 hpf, 5.3 hpf, and 5.7 hpf and 6.3 hpf. Column B, Normalized simulation result of a wild type case 4.7 hpf, 5.3 hpf, and 5.7 hpf and 6.3 hpf. Column C, Relative differences between simulation results and P-Smad5 level. Positive error indicates the experimental data are higher than simulation results, negative error indicates the experimental data are lower than simulation results.93

Figure 5.6. Test of expression regions for finding the possible expression patterning induces the best-fitting simulation result on 3.5,4.7,5.7,6.3, and 8 hpf. A. Original BMP expression map obtained from the imaging of RNAscope experiment, B-D, the example of three different testing BMP expression map. E. Best-fitted result on marginal region, F, Best fitting result on the central

region. Smooth lines represent the FEM simulation results interpolate on the experimental data location, triangle indicated the averaged and normalized P-Smad5 level.94

Figure 5.7. Comparison of growing domain advection model (A) vs fixed domain diffusion only model (B) of BMP concentration profile in 3D lateral view. Red lines represent the growing domain simulation result of BMP concentration on marginal region and central region, Blue lines represent the fixed domain diffusion only simulation result of BMP concentration on marginal region and central region, for 4.7,5.3,5.7,6.3 hpf.96

Figure 5.8 A. Comparison between embryo size in real scale. Points cloud indicates the FEM mesh nodes on the specific embryo size. B. Relative BMP gradient reflex in real embryo length C, Relative BMP gradient reflex in normalized embryo length. For clear plotting, only the results from embryos with the radius of 250 μm , 300 μm , and 350 μm were shown in the figure.97

Figure 5.9 Relative BMP gradient for different size embryos at different development stage, 4.7hpf,5.3hpf, 5.7hpf, 6.3hpf, 6.7hpf and 8hpf. A, Plot in normalized embryo length B, Plot in real embryo length.98

Figure 5.10 Pointwise Scaling Error (SE) at different development stages, 4.7hpf,5.3hpf, 5.7hpf, 6.3hpf, 6.7hpf and 8hpf in WT and Sz1 mutant embryos results. Error bar indicates the maximum and minimum error over five different embryo sizes from 250 μm ~ 350 μm radius.99

Figure 5.11 Experimental P-Smad5 gradient profiles of WT and Cut embryo scale. (a) The animal and lateral views of P-Smad5 stained 6 hpf embryo point clouds after image processing with P-Smad5 labeling intensity in color. (b-c) P-Smad5 gradient profiles of WT (black) and Cut (red) embryos after filtration, at x/Lmax scale and x/L scale. Figure adapted from Huang (2019) [92] 100

Figure 5.12 Simulation result of FEM model..... 101

Figure 5.13 The BMP profile result comparison of FEM model vs Finite difference model101

Figure 6.1. Integrate with the stochastic study of downstream gene transcription with BMP signaling regulation 106

Figure 6.2. Cell level dynamic P-Smad level by the stochastic model 106

Figure 6.3. The multiplicative split of the deformation gradient to model growth 107

ABSTRACT

Embryonic development is a complicated phenomenon influenced by genetic regulation and biomechanical cellular behaviors. However, the relative influence of these factors on spatiotemporal morphogen distributions is not well understood. Bone Morphogenetic Proteins (BMPs) are the primary morphogen guiding the dorsal-ventral (DV) patterning of the early zebrafish embryo, and BMP signaling is regulated by a network of extracellular and intracellular factors that impact the range and signaling of BMP ligands. Recent advances in understanding the mechanism of pattern formation support a source-sink mechanism, however, it is not clear how the source-sink mechanism shapes patterns in 3D, nor how sensitive the pattern is to biophysical rates and boundary conditions along both the anteroposterior (AP) and DV axes of the embryo.

Throughout blastulation and gastrulation, major cell movement, known as epiboly, happens along with the BMP mediated DV patterning. The layer of epithelial cells begins to thin as it spreads toward the vegetal pole of the embryo until it has completely engulfed the yolk cell. This dynamic domain may influence the distributions of BMP network members. This project aims to investigate the multiscale regulatory network of the BMP signaling dynamics along with the biophysical deformation of the embryo tissue during epiboly.

In this study, we present a three-dimensional (3D) growing domain mathematical modeling framework to simulate the BMP patterning and epiboly process during the blastula to gastrula stage zebrafish embryo, with both finite difference and finite element approaching. These models provide a starting point to elucidate how different mechanisms and components work together in 3D to create and maintain the BMP gradient in the zebrafish embryo. We are interested in how the cellular movements impact the formation of gradients by contributing an advective term whereby the morphogens are swept with the moving cells as they move vegetally. Dynamic cell imaging data are used to quantify the cell movement during the epiboly. We evaluated the accuracy of the mesh updating compared to the advection caused by cell movement and its role in embryonic patterning. Quantitative whole-mount RNA scope data of BMP2b, Chordin, Noggin, Sizzled, and phosphorylated-SMAD data are collected and analyzed precisely to test the hypotheses of the gradient formation mechanism in our model. We also present a novel approach of Neuro Network model to accelerate the computationally intensive PDE simulations. Our goal is to develop a complete advection-diffusion-reaction model that incorporates all stages of zebrafish embryonic

development data. By combining the biophysics of epiboly with the regulatory dynamics of the BMP network, we can test complex models to investigate the consistent spatiotemporal DV patterning in the early zebrafish embryo.

1 INTRODUCTION

Nature's beauty blends in the formation of different structures and patterns of organisms. Amazed by nature's astonishing designs, people have studied the underlying phenomena and mechanisms of patterns throughout history. Pattern formation by morphogens drives the normal development of various processes such as limb development and organogenesis in animals [1]–[5]. '*Morphogen*' is a term coined by Alan Turing in 1952 when he predicted a chemical mechanism for biological pattern formation [6]. Now, morphogens are defined as signaling molecules that transport by diffusion [7] and act directly on cells to introduce intracellular signal transduction depending on their local concentrations [8]. Recent studies of morphogenesis highly focus on the chemical basis of morphogens, using the diffusion-reaction model and positional information model. These show us a glimpse of how morphogens contribute to the development and pattern formation of living tissue[9]. In zebrafish, patterns of gene expression along the dorsal-ventral (DV) body axis were regulated by Bone Morphogenetic Proteins (BMPs) [10]. In early embryonic development, BMP signaling patterns DV axis formation in both invertebrates and vertebrates [11], [12]. Recent advances in understanding the mechanism of pattern formation support a source-sink mechanism, however, it is not clear how the source-sink mechanism shapes patterns in 3D, nor how sensitive the pattern is to biophysical rates and boundary conditions along both the anteroposterior (AP) and DV axes of the embryo.

Throughout blastulation and gastrulation, major cell movement, known as epiboly, happens along with the BMP mediated DV patterning. This dynamic domain may influence the distributions of BMP network members. This project aims to investigate the multiscale regulatory network of the BMP signaling dynamics along with the biophysical deformation of the embryo tissue during epiboly.

1.1 Early-stage Zebrafish embryo development

Zebrafish, *Danio rerio*, has emerged as an essential model for studying pattern formation in developmental biology. One of the ultimate goals of developmental biology is to understand diseases better, and because zebrafish share approximately 75% similarity with the human genome [13], they are beneficial for studying human disease. Zebrafish also make great models for experimentation. Their embryos develop rapidly, are transparent, and are large enough to manipulate and observe through microscopic imaging during the entire embryonic stage. By using fluorescent markers, specific cells or regions can be detected by microscopic fluorescent imaging equipment. Thus, observing different mutants of zebrafish with fluorescent imaging can help explain how normal functions are affected by various factors during disease processes. These characteristics of zebrafish make them very suitable for generating data to apply in mathematical models and investigate the background mechanisms under the scope of BMP-mediated patterning in vertebrates.

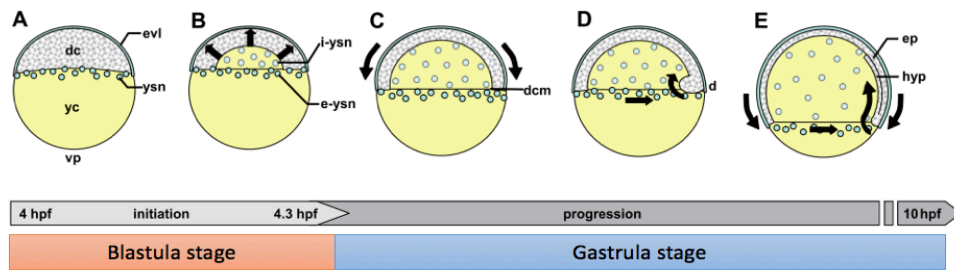


Figure 1.1. Epiboly process in the zebrafish embryo adapted from [15] d, dorsal; dc, deep cells; dcm, deep cell margin; e-ysn, external yolk syncytial nuclei; ep, epiblast; hyp, hypoblast; i-ysn, internal yolk syncytial nuclei; vp, vegetal pole; yc, yolk cell. Black arrows show the general cell movement direction. Deep cells are shown in white, the EVL and YSL in blue and the yolk cells are shown in yellow.

For a zebrafish embryo starting at the blastula stage, with the continuation of epiboly, cells proliferate and differentiate then move through involution, convergence, and extension until covering the whole sphere-like embryo [14]. The gastrula stage finishes at the end of the epiboly [14]. BMP signaling begins the patterning of ventral tissues at the onset of gastrulation [10]. During gastrulation, coordinated cell movements organize the germ layers and establish the major body axes of the embryo [15]. The most important and distinct cell movements during the gastrula

stage are epiboly. Epiboly begins at the end of the blastula stage and continues through the whole gastrula stage which is characterized as a thinning and expanding of cell layers [16]. Figure 1.1 describes the overall cell movement trend during epiboly. (A) At the later blastula stage, the enveloping layer (EVL) and yolk syncytial layer (YSL) has been created and the deep cells form a flat interface with the underlying yolk cell. (B) Upon epiboly initiation, the yolk cell domes, and deep cells move radially outwards, forming a cap of cells over the yolk. (C-E) During the progression phase, the blastoderm continues to thin, expanding its surface area to envelop the yolk cell. (D) Once the blastoderm has covered approximately 50% of the yolk, deep cell epiboly temporarily pauses as cells begin to converge dorsally and gastrulation begins. (E) Concurrent with the other gastrulation movements, the deep cells, EVL and YSL move towards the vegetal pole in a coordinated manner, eventually closing the blastopore. The significant cell movement during epiboly might play a role in BMP gradient formation since the cells secreting BMPs and their regulators are moving as well. Additionally, the advection of extracellular fluid caused by cell movement may also influence the BMP gradient.

1.2 Bone morphogenetic proteins (BMPs) and Dorsal-Ventral (DV) patterning

Pattern formation in zebrafish is regulated mainly by Bone Morphogenetic Proteins (BMPs), a kind of morphogen. By regulating the activities of series-downstream genes, BMPs play a significant role in tissue patterning throughout the body (both in vertebrates and invertebrates)[17]. BMPs are a critical member of the TGF (transforming growth factor β , TGF- β) superfamily, which was originally discovered for their bone formation capabilities. More than fifteen BMPs have been discovered. Depending on the amino acid or nucleotide similarity, these BMPs can be divided into different subcategories: BMP2/4, BMP5-8, BMP9/10, and BMP12-14[18]. BMP2/4/7 have been proven to play an essential role during the embryogenesis of zebrafish [19]–[21]. BMP signaling is essential for early embryonic development and patterning processes, cell proliferation, differentiation, and even apoptosis [22]–[27]. As a result, the study of BMP-mediated regulation during development is a vital part of developmental biology.

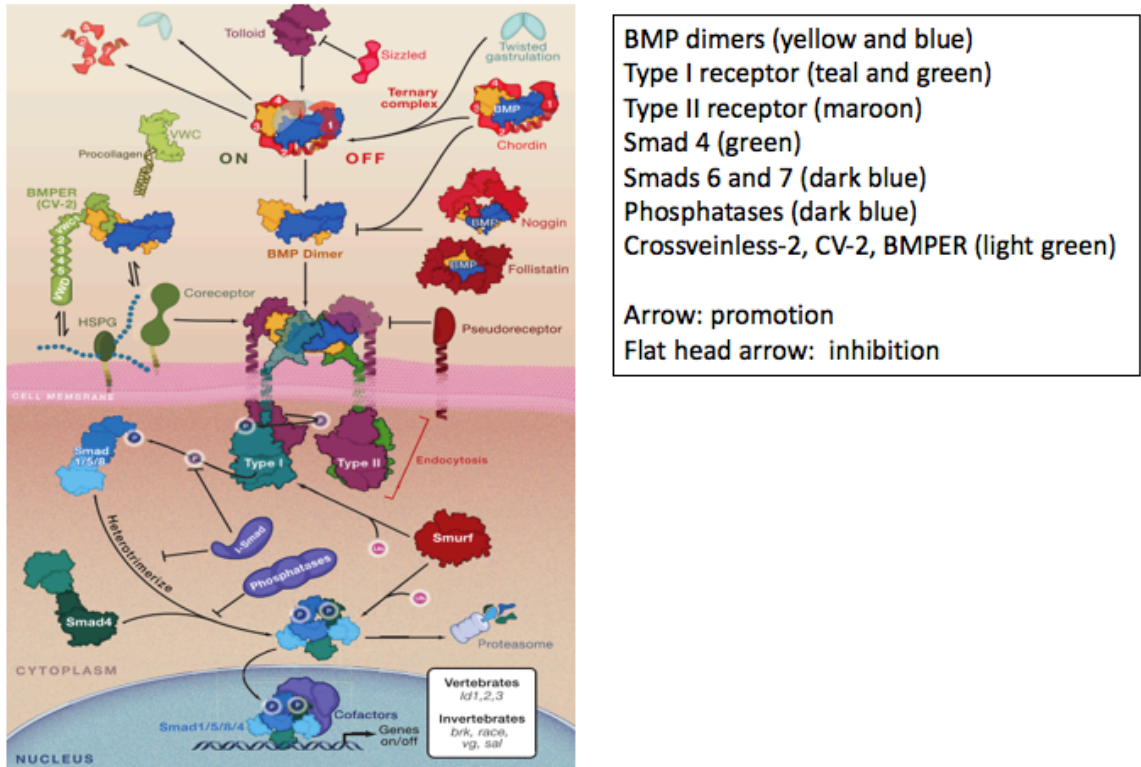


Figure 1.2. Illustration of BMP signaling pathway, adapted from J. A. Dutko and M. C. Mullins [26]

BMP signaling is propagated by the binding of BMP dimers to serine/threonine kinase receptors on the cell membrane. Figure 1.2 gives an overall illustration of the extracellular to the intracellular BMP-signaling pathway. Activated Type I and II receptors form higher order tetrameric complexes further phosphorylates Smad proteins (Smad1, Smad5 in zebrafish, and Smad8), promoting Smad molecule release from the cell membrane receptors. Then Smad binds Smad4 molecules in the cytoplasm, and the bound complex accumulates in the nucleus and regulates differential gene expression. Inside the nucleus, the Smad complex binds with other DNA-binding proteins and directly regulates the transcription of target genes [17], [25], [27], [28].

The normal BMP signaling pathway is similar between invertebrates (e.g., *Drosophila*) and vertebrates (e.g., zebrafish). However, the regulation mechanism of the BMP signaling can be slightly different in various species. The first stage of early embryonic development that both invertebrates and vertebrates require BMP signaling is the patterning of the Dorsal-Ventral (DV) axis [11], [12]. Researchers have shown that BMPs affect the DV patterning of zebrafish, *Xenopus*,

and *Drosophila* embryos by using a gradient-based mechanism, in which different levels of BMP signaling can activate different expressions of the gene[29]. However, BMP signaling affects the DV patterning differently in different species. In *Drosophila*, BMP signaling has been found to pattern dorsal cell fate. In contrast, in zebrafish and *Xenopus*, BMP signaling patterns ventral cell fate, and the patterning of the dorsal side requires suppression of BMPs[30].

It has been reported that dorsoventral pattern mutants have mutations in genes encoding BMPs or proteins involved in the modification or transduction of BMP signaling[31]. Table 1.1 lists some mutants and their phenotypes related to BMP signaling regulators. Null mutations cause the strong dorsalization of swirl (*swr*), snailhouse (*snh*), lost-a-fin (*laf*), and somitabun (*sbu*) mutants in *Bmp2b*[32], *Bmp7*[31], [33], the *Bmp* type I receptor *Alk8* [34] and the *Bmp*-regulated transcription factor *Smad5* [35], respectively. The strong ventralization of *dino* mutants, on the other side, is caused by a null mutation in *Chordin*[36]. The weak dorsalization of *minifin* (*mfu*) mutants is due to null mutations in *Tolloid*[33], [37]

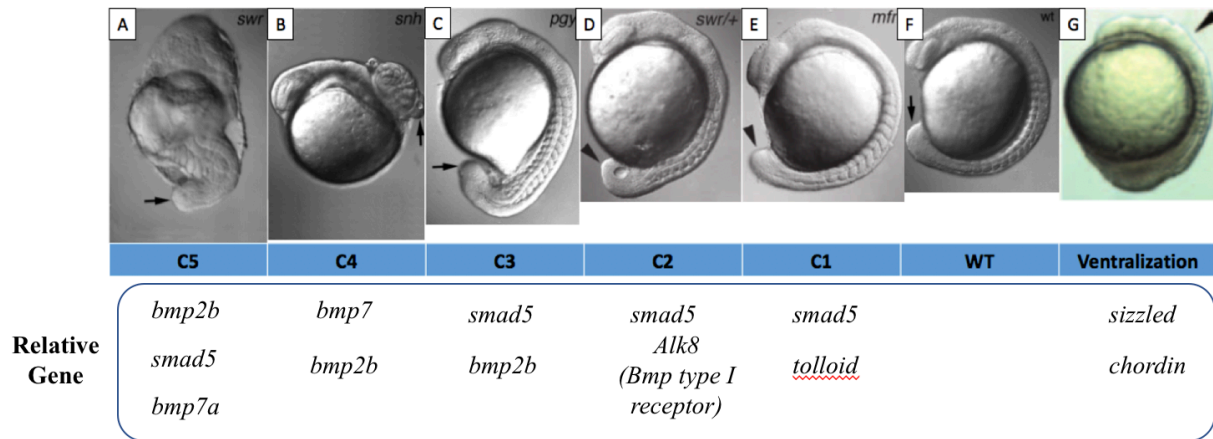


Figure 1.3. A-F Mutants of dorsalization strength from C1 to C5 according to their strength, with 1 being the weakest and 5 the strongest. The strength of the phenotype is based on the degree to which the notochord, somites, and tail are affected. G, Ventralization mutant (picture adapted from Mullins (1996) [33] and Little (2004) [38])

Table 1.1. BMP signaling related mutants and phenotypes in zebrafish

Mutant name	Alleles	Relative Gene	Phenotype	References
<i>swirl (swr)</i>	<i>tc300</i> <i>ta72</i>	<i>bmp2b</i>	Dorsalization (C5)	[31]–[33], [39]
<i>somitabun (sbn)</i>	<i>dtc24</i>	<i>smad5</i>	Dorsalization (C5)	[31], [33]
<i>snailhouse (snh)</i>	<i>ty68a</i>	<i>bmp7</i>	Dorsalization (C4)	[31], [33]
<i>aubergine</i>	<i>sb1aub</i>	<i>bmp7a</i>	Dorsalization (C5)	[40]
<i>piggytail (pgy)</i>	<i>dty40</i> <i>dti216</i> <i>tc227a</i> <i>tm124a</i> <i>ta206</i> <i>tx223</i>	<i>smad5</i>	Dorsalization (C3-C4) Dorsalization (C2-C3) Dorsalization (C1-C2) Dorsalization (C1) Dorsalization (C1) Dorsalization (C1)	[33], [41]
<i>minifin (mfn)</i>	<i>tv9b</i> <i>tc263a</i> <i>tt203a</i> <i>ty130a</i> <i>tb241c</i> <i>tf211a</i> <i>tf215a</i> <i>tn217b</i>	<i>tolloid</i>	Dorsalization (C1)	[31], [33], [37]
<i>lost-a-fin (laf)</i>	<i>tm110b</i>	<i>Alk8</i> (<i>Bmp type I receptor</i>)	Dorsalization (C2)	[31]–[34]
<i>wirligig</i>	<i>dta72</i> <i>tc300a</i>	<i>bmp2b</i>	Dorsalization	[33]
<i>Mercedes (mes)</i>	<i>tz209</i> <i>tm305</i>	<i>sizzled</i>	Ventralization	[42], [43]
<i>dino (din)</i>	<i>tm84</i> <i>tt250</i>	<i>chordin</i>	Ventralization	[36], [39], [42]

In the zebrafish embryo, the BMP signaling is significantly modulated by its extracellular modulators, Chordin, Noggin1, Follistatin-like1b (Fstl1b), and ADMP on the dorsal side, and Bmp1a, Tolloids, Twsg1a, CV-2, and Sizzled on the ventral side. Chordin, Noggin1, and Follistatin-like 1b (Fstl1b) work as antagonists. Tolloids and ADMP work as activators; Twsg1a and CV-2 can play the roles of both antagonist and activator; sizzled can attune BMP signaling in an indirect way [26].

1.3 Extracellular regulation of BMP

BMP signaling regulation in zebrafish embryos is a complex network. Despite advances in the understanding of individual regulators of BMP signaling, the interaction network of how these factors regulate and interact with each other spatially and temporally to generate the robust BMP gradient that patterns DV tissues is not well understood. The primary goal of our study is the characterization of the contribution of extracellular modulators and intracellular feedback regulators in establishing and controlling BMP signaling along the dorsal-ventral (DV) embryonic axis, and the determination of BMP signaling corresponds to the space and time-dependent patterns of gene expression.

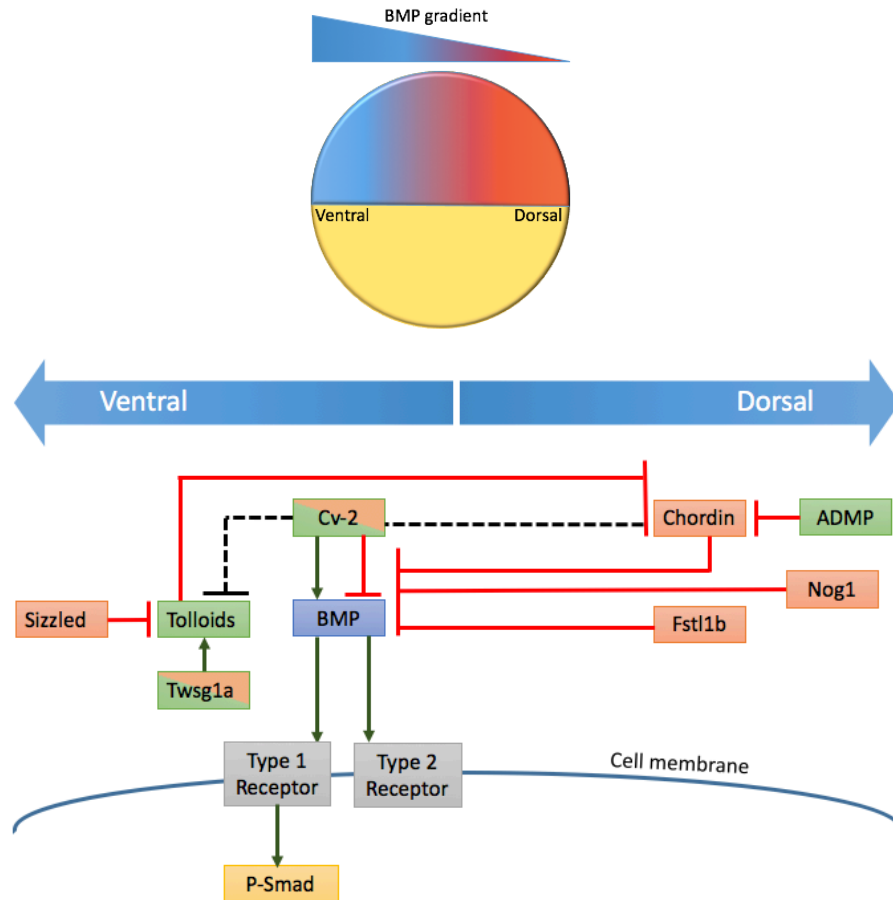


Figure 1.4. BMP gradient distribution and potential mechanism of BMP modulators in zebrafish embryo. [blue box (BMP), red box (inhibitor), green box (activator), green/red box (inhibitor/activator), redline (inhibition), green line (promotion), green/red line (inhibition/activation), dashed line (potential interaction)].

In the zebrafish embryo, the BMP signaling is significantly modulated by its extracellular modulators, Chordin, Noggin 1, Follistatin-like 1b (Fstl1b) and ADMP on the dorsal side, and Bmp1a, Tolloids, Twsg1a, CV-2 and Sizzled on the ventral side. Chordin, Noggin 1, and Follistatin-like 1b (Fstl1b) work as antagonists. It has been proven that the depletion of antagonists can cause the *Xenopus tropicalis* to lose neural tissue and dorsal mesoderm completely[44]. Bmp1a and Tolloids work as activators; Twsg1a and CV-2 can play the roles of both antagonist and activator; sizzled can attune BMP signaling also in an indirect way[26]. The details of each modulator and background mechanism are listed below.

Chordin (Chd), the antagonist, Chordin (homolog of Sog in *Drosophila*) modulates BMP signaling by blocking with receptors for ligand binding extracellularly, thus the signal transition is obstructed[29], [45], [46]. Chordin is secreted before the start of gastrulation, which is a key modulator since it also interacts with other extracellular modulators (Sizzled, Twisted gastrulation (Tsg), CV-2, and Tolloid) to affect the BMP signaling gradient and DV patterning. It is also suggested that the BMP2b/Chordin gradient guides the anteroposterior patterning of endoderm in zebrafish embryos by regulating the expression of gene her5[20].

Noggin (Nog) & Follistatin-like 1b (Fstl1b) are both antagonists, which are not found in invertebrate genomes. Noggin and Follistatin work similarly to Chordin which can bind with BMP ligand to modulate BMPs. However, unlike Chordin, they cannot be modulated by additional extracellular regulators. Besides, Noggin is also produced by the organizer at the start of gastrulation[46].

Tolloid (Tld) works as the antagonist of the BMP antagonist. As BMP antagonists can degrade the accumulation of BMPs, other molecules are also needed to prevent the over-accumulation of antagonists. Consequently, Tolloid promotes BMP signaling and ventral cell fate by mediating cleavage of Chordin. Wagner and Mullins suggested that *tolloid* acts upstream of *chordin*; the strongest phenotype of Tolloid overexpression is equivalent to a *chordin* mutant[47] (Table 3). Nevertheless, Tolloid cannot inhibit other BMP antagonists such as Noggin. Thus other than as a regulator of Chordin, Tolloid plays no other role in the early zebrafish embryo[45]. Furthermore, experiments have proven that knock-downs of both *tlll* and *bmp1a* lead to a result in strongly dorsalized phenotypes[48].

Sizzled (Szl), another antagonist of BMP signaling, depends on the presence of Chordin and Tolloid for function. Sizzled is a competitive inhibitor of Tolloid, by binding Tolloid, Sizzled can

inhibit the activator Tolloid and prevent Tolloid-mediated degradation of Chordin. In this way, Sizzled can drop the level of BMP signaling indirectly[49]. Inomata et al studied scaling of DV patterning in *Xenopus* embryo and suggested that chordin degradation is dynamically controlled by secreted Chordin proteinase inhibitor Sizzled through an axis-wide feedback mechanism [50]. Tuazon et al investigate the Sizzled role in zebrafish embryo DV patterning and proved that sizzled being induced by BMP signaling and Sizzled's role as a feedback inhibitor of Bmp1a/Tolloid.[51] However, they found that Sizzled alone may not play a role in establishing the early BMP gradient, and Sizzled and Tolloid likely shape the BMP gradient later in gastrulation to correctly pattern tail tissues.

Antidorsalizing Morphogenetic Protein (ADMP), a BMP family member, is produced on the dorsal side and could cause this specification. De Robertis gives a hypothesis in 2006 that a dorsally produced BMP plays a role in the specification of ventral fate[52]. The gene of ADMP is expressed at the gastrulation stage of zebrafish along the dorsal axis. Through a mechanism similar to BMPs, ADMP can bind Chordin and Tsg. Thus by the degradation of dorsal BMP antagonist, ADMP can work as an activator of the function of BMP signaling[53]. Table 2 gives a summary of the major extracellular modulators and their known mechanisms in regulating BMP signaling.

Crossveinless-2 (CV-2), a member of the cysteine-rich (CR) domain family is also known as BMPER in vertebrates[54]. Despite significant research, the mechanism of CV-2 is still not clear. A widely accepted view is that CV-2 can act both as an activator and an inhibitor in vertebrate BMP signaling pathways depending on the species and molecular environment [26], [55]–[57]. There are two types of existing models to explain that how CV-2 modulates BMP signaling. One is presented by Serpe et al., who suggests that by the complex interaction with BMP and BMP receptor, CV-2 can either prevent or promote BMP binding to their receptor, depending on the concentration and binding affinities of CV-2 [55], [57]. Another hypothesis indicates that the CV-2 can interact with Chordin and Tsg to achieve the function of promoting or inhibiting BMP signaling[58], [59].

Twisted gastrulation (Tsg1) is similar to CV-2, Tsg could also play the roles of both activator and antagonist on a biochemical basis[5], [38], [55]. Tsg can bind to Chd and BMP ligand independently or in a BMP-Chd-Tsg complex[60]. Tsg can promote BMP signaling by promoting the process of Tolloid cleavage Chordin. However, if Tolloid is absent it can inhibit the BMP signaling. Furthermore, in different organisms and environments, the working function of Tsg can

be different. Little and Mullins found that increased Tsg leads to relatively dorsalized phenotypes in wild-type zebrafish embryos[38]. Thus, it leads to the conclusion that instead of playing the role of both activator and inhibitor, in zebrafish, Tsg only promotes the ventral cell fate[30].

Besides, BMP signaling can also be regulated by the extracellular matrix, cell membrane co-receptors, and inhibitory pseudo receptors. For the TGF- β family of ligands, there are a total of seven Type I receptors (ALK1-7) and four Type II receptors. Three Type I receptors, BMPR-1A (ALK3), BMPR-1B (ALK6), and ActR-1A (ALK2), bind BMPs. Also, three of the four Type II receptors, BMPR-2, ActR-2A, and ActR-2B, interact with BMPs [61]. The Type-II receptor BMPR2 is capable of activating the Type I receptor BMPR1 and further transducing the signal to Smad molecules within the cell.

Table 1.2. Major extracellular regulators of BMP signaling in zebrafish embryo

Regulator	Known effects on BMP signaling	Position	Mechanisms	Reference
Chordin (Chd)	Antagonist	Dorsal	Binds BMPs	[20], [30], [45], [46]
Noggin (Nog)	Antagonist	Dorsal	Binds BMPs	[46]
Sizzled (Szl)	Antagonist	Ventral	Binds the Tolloid-related enzymes to inhibit Tolloid	[49]
Tolloid (Tld)	Activator	Ventral	Cleaves of Chordin	[45], [47]
ADMP	Activator	Dorsal	Binds Chordin and Tsg	[52], [53]
Pinhead	Activator	Ventral	Binds Chordin and Tsg	[62]
Follistatin (Fst)	Antagonist	Dorsal	Binds BMPs	[46]
Cv12 (BMPER)	Antagonist Activator	Ventral	Hypothesis 1: either prevents or promotes BMP binding to their receptor Hypothesis 2: interacts with Chordin and Tsg	[26], [54]–[59]
Tsg1	Antagonist Activator	Ventral	Promotes BMP binding to Chordin or cleaves Chordin through Tolloid	[5], [30], [38], [55], [60]

1.4 Mathematical Modeling of Pattern Formation

Mathematical models have been employed for decades to help understand biological development. Modeling of biochemical networks can help to integrate experimental knowledge into a coherent picture and to test, support, or falsify hypotheses about the underlying biological mechanisms [63]. For a system as complex as a developing animal embryo, it is almost impossible to analyze every single spatiotemporal element and give a meaningful prediction. A common strategy is to omit some details of the system and give an overall simple mathematical modeling, which can still be effective in describing a complex system[64]. Mathematical studies of BMP morphogen effects on patterning development have been rigorously performed for decades, but a comprehensive spatiotemporal model of zebrafish is still lacking.

There is a long history of studying the mechanism underlying the developmental pattern formation through the spatial distribution of an extracellular morphogen, which works as a navigator for a naïve cell to find their fate by transducing at a distinct level[7], [65], [66]. The reaction-diffusion model which is established by Alan Turing is the first morphogen-based mathematical modeling that can rationalize the development of spatial patterns [64]. Normally, we consider a morphogen that is produced on a source and spreads to target tissues by diffusion and is degraded by modulators[67]. The morphogen (BMP) concentration gradient can be defined as spatially and temporally by the reaction-diffusion equation. In Turing's reaction-diffusion model, he describes the concentration of morphogens over time by a partial differential equation, which obeys Fick's law of diffusion.

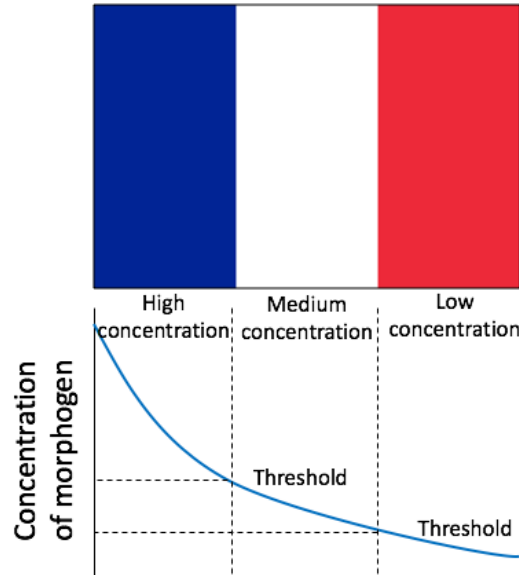


Figure 1.5. French flag model
(high morphogen concentration in blue, the medium in white, and low in red).

The Positional Information (PI) model developed by Wolpert in 1969 is a mechanism that gives a concept of cells, which have their knowledge of their specific positional information, and this information is independent of molecular differentiation[66]. Wolpert illustrated his concept of positional information by adopting the image of the tri-colored French flag, where high morphogen concentration is closest to the source and low morphogen concentration is furthest from the source. Show as Figure 1.5, the different stripes of the “flag” represent the different thresholds by which various concentrations affect the cell state differently [66]. This model is widely used to explain the mechanism of pattern development [68], [69].

Mathematical models of BMP signaling focus on finding the mechanism of BMP concentration gradient formation. As more molecules are involved in the processes of pattern formation and BMP signal transduction, an increased need is found for understanding the mechanism between BMP regulators and how the components work together to regulate gene expression and phenotype of an organism[70], [71].

To model the BMP signaling network we need to model the embryo tissue as well. The complexity of the embryo structure, and its internal interactions between the living cells, is difficult to render into a relatively simple mathematical model. Therefore, the description of the cell behaviors inside the embryo directly decides the quality and consistency of the mathematical

model.[72] Generally, there is two main approaches: continuous and discrete model. Continuous signaling models use reaction-diffusion equations to model large biochemical networks by describing the cell interactions without precisely depicting single cells[72]. Resolving cells, and possibly subcellular structures explicitly requires complex meshing and moving boundaries, thus leading to relatively high computational complexity[73]. The typical widely applied discrete model of cellular modeling is the agent-based model; the cells are treated as distinct objects or agents and are allowed to move, divide, and die individually according to biophysically-based rules[74]. Normally, the agent-based model restricts the positions and orientations of the cells in regular lattices to save on computational cost, though some the agent-based methods may not restrict[74]. In this review, I focus on the continuous model, specifically the reaction-diffusion-equation-based model since it is more widely applied to the pattern formation mechanism.

Some mathematical models of morphogenesis focus on the morphogen transport mechanism itself. Muller gives an overall description of seven types of mechanisms that may happen during morphogen transport: (1) free diffusion, (2) hindered diffusion, (3) tortuosity combined with transient binding, (4) facilitated diffusion, (5) shuttling, (6) transcytosis, and (7) transport with cytonemes [75], [76]. Not only is the diffusion of BMP complex, but how the regulators degrade or promote the BMP gradient is also a complex process; it may include several mechanisms, like linear or nonlinear degradation and feedback process through different loops. Next, some existing models of the BMP signaling will be analyzed to give a view of the current state of the art in this area.

Compared to zebrafish, BMP signaling regulation and its mathematical models have been extensively studied in *Drosophila*. As mentioned before, gradient-based mechanisms for BMP gradient are similar between zebrafish and *Drosophila* embryos. Even though the BMP patterning in *Drosophila* patterns dorsal cell fate but the underlying mechanisms share commonalities, for instants, Screw (Scw) and Decapentaplegic (Dpp) in *Drosophila* are BMP class ligands, short gastrulation (Sog) is a Chordin homolog, and Tld and Tsg also exist in *Drosophila* embryo. Due to the leak of literature in the mathematical model of BMP signaling in zebrafish, the study of *Drosophila* systems still can reasonably support the zebrafish system.

Drosophila, commonly known as fruit flies, is one of the most useful organisms in biological studies [68], [77], [78]. In this system, mathematical modeling has been especially valuable in explaining a variety of experimental results. The development of *Drosophila* can be divided into

two phases: the embryonic phase and the larval phase. Pattern formation in both of these phases has been studied by using mathematical models. Bicoid, the first protein proved to act as a morphogen in *Drosophila*, has been considered to be involved in early anterior-posterior (AP) patterning [79]. Dpp is involved in both the embryonic dorsal-ventral (DV) patterning and the AP patterning of wing imaginal disc [80], [81]. Here, I only focus on the models relative to BMPs and its homologs.

Early models have focused on extracellular regulators only [78], [82], [83]. Eldar presented a model of transport of the Scw and Dpp into the dorsal midline. The regulators include Sog, Tld, and Tsg. Similar to Chordin, Sog works as an inhibitor and is a key point in this model. The model explained the robustness under the BMP gradient under the condition of partial loss of molecules in the system. It concluded that the robustness relies on the excess store of BMPs and the shuttling of BMP by inhibitors [78]. Later in 2005, Lou presented a similar model about Dpp/Sog system and focused more on the steady-state configuration. These two mathematical models both described the extracellular patterning network and were developed to identify the parameter regions and what types of biophysical parameters are needed. However, no experiments have been done to validate the model [77].

Researchers have found that intercellular feedback is also important to the regulation of BMP signaling. Wang and Ferguson presented a model including intercellular feedback, which encourages ligand binding that relies on previous signaling levels. By introducing the intracellular feedback, spatial bistability of two stable states of BMP-receptor interaction can be observed [82]. The concept of bistability was then improved by Umulis et al. in 2006 by including positive feedback of a cell surface BMP-binding protein (SBP), such as CV-2 [83]. As mentioned in the earlier section, CV-2 can act as both an antagonist and an activator, which have been proved both experimentally and mathematically by Serpe in modeling the BMP signaling of *Drosophila* wing disc pattern formation [57]. The contribution of a feedback function included in the model is an increased understanding of how cells modify both their own interpretation of the signal and the signal levels of other cells in the tissue.

As the models of BMP signaling grow more complex and incorporate more components, the limitations of the geometry are revealed. The importance of geometry in mathematical models has been widely studied. Thus, there is an increased need for 3D models in studying both the spatial and temporal aspects of embryo-scale modeling [84]. In 2010, Umulis et al. presented a three-

dimensional organism-scale model of BMP-based patterning in *Drosophila* embryo. Different mechanisms combined with geometry and scale-invariances have been tested in this model. The results show high agreement with experimental image data, leading to the conclusion that a three-dimensional model is essential to understanding the mechanisms that guide tissue patterning [68]. The inclusion of three-dimensional geometry is important for the realistic modeling of a complex embryonic shape.

The mathematical study of BMP signaling intensively studies in *Drosophila*, however, fewer models have been studied in zebrafish. In our previous work, we developed a data-based 1-D model to investigate the mechanisms of BMP-mediated DV patterning in blastula embryos to early gastrula embryos at 5.7 h post-fertilization (hpf) before the initiation of BMP-mediated feedback [85]. In this study, we simulated BMP gradient formation along the margin line at the embryo and used the quantitative measurements of spatial-temporal P-Smad5 profile to inform our model selection. This study support Chordin majorly sharpening BMP gradient by a source-sink mechanism rather than a counter gradient mechanism.

Geometric Previous work in *Drosophila* focused on a three-dimensional organism-scale model of BMP and gap gene patterning in the *Drosophila* embryo [8], [68], [86]. To date, there are few mathematical models for zebrafish embryonic development and only one that developed a 3D approximation by Zhang et al. to study the role of Chordin in regulating BMP signaling in zebrafish [87]. This model focused on the blastula stage from 30% epiboly to the early gastrula shield stage (around 50% epiboly), however, it did not include growth, was not compared to data, and suggested a mechanism of BMP shuttling that has now been shown not to function in the embryo [85].

In our current study, we seek to add growth and 3D patterning to the model to test mechanisms of patterning in 3D. The 3D model provides multiple advantages to 1D models [51], [88] which allows us to use all the data from imaging instead of a subset and improves model discrimination. To consider the cell movement during epiboly; this problem turns to be a moving domain and advection active problem. The simulation of time-dependent advection-diffusion-reaction equations is required in various applications. A typical simulation of processes that involve a chemical reaction in a flow field is modeled by a non-linear system of time-dependent advection-diffusion-reaction equations for the concentrations of the reactants and the products. These equations are strongly coupled such that inaccuracies in one concentration directly affect all other

concentrations. We present two different methods to solve this problem. My first approach is using a mass adding finite difference scheme, to represent the realistic embryo geometries my other approach is a finite element scheme in ALE formulations with moving boundaries and interfaces. In the Chapter 3 and Chapter 5, we will discuss these two types of mathematical approaches separately.

Our proposed 3D feedback models for later stages of development will be critical in understanding the mechanisms of BMP pattern formation in the zebrafish embryo, the role of feedback, and provide new insight into how morphogen gradients evolve in a rapidly changing tissue.

1.5 Scaling invariance in Zebrafish embryo

Generally, scale invariance represents a key feature of a system that keeps consistent when scale by size or other factors. In organisms, within the same or relative species, the tissues and organs may vary by size but similar in morphology, which appears to be scaled in a pattern. In pattern formation, a morphogen forms a non-uniform spatial distribution over a field of cells and the concentration gradient further triggered the underlying gene expression eventually control the forming of the tissue and organ pattern. The pattern scale invariance is maintained through the signaling network robustness during the morphogen gradient formation under perturbations. It has been an enduring question in current biology that what mechanism leads to the robustness of that regulate scaling of patterns in the organism during development. In our current case of BMP mediate DV patterning, a Recent study shows scale invariance has been found in both vertebrates and invertebrates, including *Drosophila* and *Xenopus* [90], [91], however, the mechanisms that regulate gradient scaling remain controversial.

In the *Drosophila* embryo, dorsal exterior patterning by Decapentaplegic (Dpp), the fly homolog of the secreted mammalian BMP2/4 signaling molecules, reveals scaling between closely related species and between individuals within a species [68]. Particularly, between *Drosophila melanogaster* and related species, the larger *Drosophila virilis*, and the smaller *Drosophila busckii*. the ratio of average Dpp/BMP- induced pMad pattern constantly width-to-embryo length [91], considering as interspecies scaling invariance. Meanwhile, individual embryos with different sizes within those species maintain this constant ratio as well [68]. Also, the study of scaling invariance in the zebrafish embryo shows that the intraspecies embryos maintain scaling of the Dpp/BMP

signaling gradient in the face of experimental reductions in embryo size of up to 30% [92]. To understand the underlying mechanism for the scaling invariance, Inomata, etc. performs Computational and experimental studies in *Xenopus* embryos, show that the scaling mechanisms in early *Xenopus* embryos highly depend on the stabilizes of Chordin degradation which is controlled by embryo-size-coupled Sizzled accumulation dynamically [50]. BMP-mediated pattern formation is valuable for understanding the mechanisms and requirements of scale invariance, an example of biologically achieved robustness.

2 QUANTIFYING SPATIOTEMPORAL BMP SIGNALING, FEEDBACK TARGET GENE EXPRESSION IN ZEBRAFISH BLASTULA AND GASTRULA EMBRYOS

2.1 Quantifying spatiotemporal cell movement

BMP signaling plays a crucial role in patterning the ventral cell fate through gastrulation where the regions of the embryo over which BMP is patterning are rapidly changing as the cells stream and converge (Figure 1.1). Cell flow may contribute to morphogen dispersion through active transport, where we consider the influence of advection on reaction-diffusion dynamics. Morphogen transport is influenced by advection in addition to the diffusion of the ligand as a potential source of gradient shaping dynamics. One of the core questions we want to answer through this study is how the cell movement during epiboly affects the BMP gradient formation. We first estimated the potential role of advection in shaping the gradient-based on our estimates for diffusion and the rates of cell movement in early development. Keller et al. presented a digital embryo of zebrafish embryos during the first 24 hours of development, and it provides a database of cell position, divisions, and migratory tracks [93]. Cell migration trace data from 3.5 to 9.6hpf has been collected through the digital embryo dataset, including time-dependent cell positional data and a MATLAB cell tracking code provided by Keller et al. We created our framework to analyze the cell movement trend and the significance of advective transport. We also calculated the average instantaneous cell velocities during the early blastula and gastrula stages and created a general cell velocity map which can be read by our growing domain finite element model to generate the advective transport of the proteins through the cell movement in our advection-diffusion and reaction model.

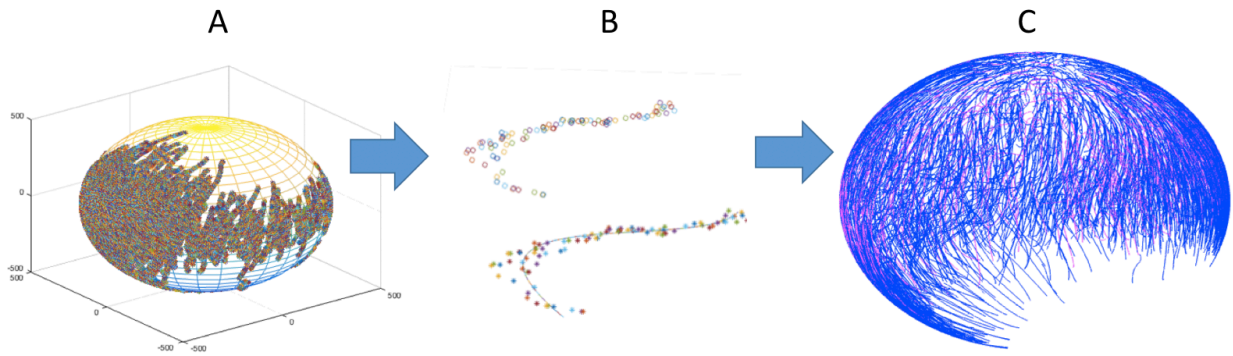


Figure 2.1. Cell movement trace fitting during epiboly, (A) Individual Cell traces map on the sphere, (B) Smoothed cell trace, (C) Overall cell movement map

To ignore the individual differences of embryo shape, we consider the embryo as a spherical shape ideally (Figure 2.1). Individual cell traces have been mapped to the standard sphere and fitted to a smooth parametric function to extract the overall trend of the cell movement during epiboly.

We then calculated the cell movement along the azimuth and elevation directions through spherical coordinates and found that the average velocity on elevation direction is much higher than the velocity on azimuth direction. This indicates that the majority of cells move directly from the animal pole toward the vegetable pole during the epiboly. Figure 2.2 shows the map of the instantaneous angular velocity on azimuth and elevation direction based on all the cell traces data we have obtained. We also found that before 30% epiboly the cells close to the animal pole are more like to move randomly. After 40% epiboly and with the start of gastrulation, the cell velocity has a dramatic increase, and the majority of the cells are moving straight toward the vegetal pole. Also, after 50% epiboly, the cell movement polarized along with the DV patterning is ongoing. In particular, the cells in the dorsal region move relatively faster than the cells located in the ventral region. Thus, the closed point of epiboly does not locate exactly 180 degrees from the vegetal pole.

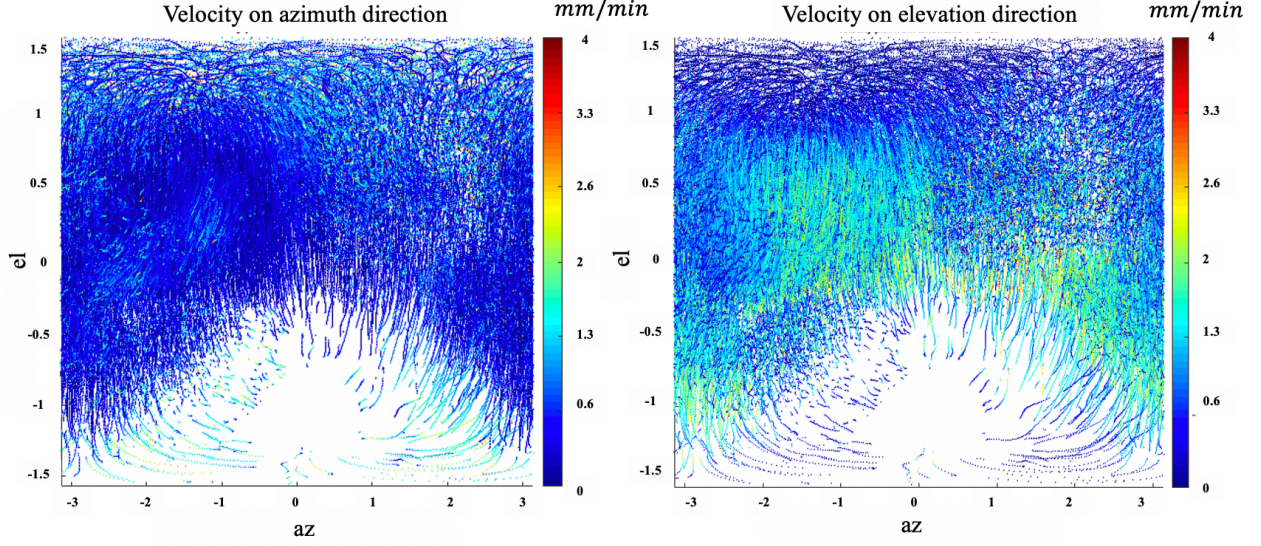


Figure 2.2. Cell velocity map of velocity components on azimuth (A) and elevation (B) direction during epiboly. Use the azimuth angle, az , and the elevation angle, el , to define the spherical coordinates.

2.1.1 Diffusion vs Advection

To decide whether the advective transport caused by the cell movement or diffusive transport dominates the BMP concentration profile during blastula stages, we estimated the average Péclet number based on the cell tracing data from 4.7 to 5.3 hpf.

The Péclet number (Pe) is a dimensionless number that represents the ratio of the advection rate over the diffusion rate in an advection-diffusion transport system [94]. The Péclet number (in terms of timescales for each process) is defined as:

$$Pe = \frac{\text{advective transport rate}}{\text{diffusive transport rate}} = \frac{\tau_D}{\tau_A}$$

where $\tau_D = \frac{L^2}{D}$ and $\tau_A = \frac{L}{v}$, Thus

$$Pe = \frac{Lv}{D}$$

v represents linear flow velocity; L represents the characteristic length of the flow and D is the diffusion constant. In this study, one-quarter of the embryo radius was used as the characteristic

length due to the average distance traveled for components considering the spatially distributed sources.

Figure 2.3 illustrates the cell trace by 5.7 hpf on a 2D map of elevation and azimuth directions, the color scale represents the Péclet number based on the cell velocity. The median blastula stage Peclet number is 0.428 among all trackable cell traces in the embryo, Figure 2.3A. Looking at only the region near the margin (where the DV axis specification occurs), it is 0.380. These numbers support the assumption of diffusion dominance prior to 50% epiboly. With a Péclet number in the measured rates for the blastula stage, the time scale for diffusion is about 2-3 times lower than for advection, suggesting that the advective term is a minor contributor to flux. Thus, for the blastula stage embryo, we can assume this problem as a moving domain non-advection problem. However, later during gastrulation, we found that the Péclet number is approximately equal to or larger than 1 throughout the entire embryo, suggesting that the advective term is a major contributor to flux, suggesting the need to account for both advection and diffusion.

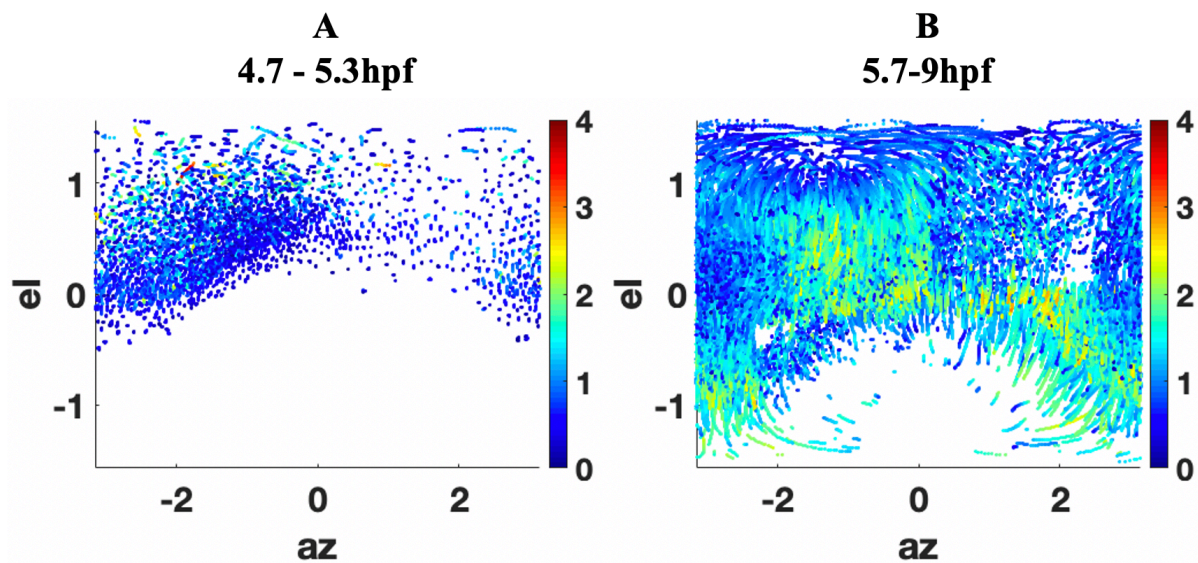


Figure 2.3. Cell trace map on elevation (el) and azimuth (az) direction around 50% epiboly (A: 4.7-5.3 hpf) and 90% epiboly (B: 5.7-9hpf), color represents the Péclet number based on the cell velocity calculated every 15 min. hpf: hours post fertilization. 0 on the az axis represents the ventral end.

2.1.2 Apply cell movement map to finite element model

To translate cell movement data into our growing domain finite element model as the driver of advective transport during DV patterning and epiboly, a 3D dynamic cell velocity map on the spherical domain was generated based on the analysis in the previous section. This map will encompass the mesh growth in our growth domain finite element model. Details related to mathematical aspect of embedding cell velocity map into finite element scheme will be discussed in Chapter 3.2.

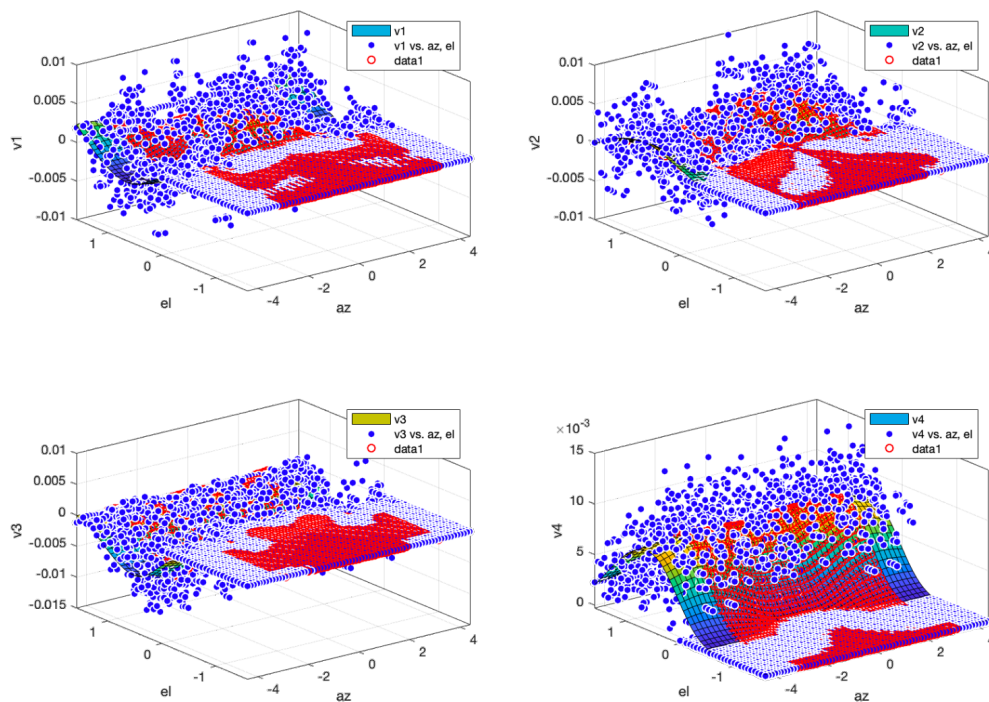


Figure 2.4 Lowess fit of the averaged velocity data. v_1 , velocity on x direction, v_2 , velocity on y direction, v_4 , velocity on z direction. v_4 , velocity magnitude.

We calculated the individual cell velocity every 15 min based on the cell traces obtained from Chapter 2.1.1. An evenly distributed point cloud was generated for obtaining the average velocity trend through the sphere. Then the averaged velocity data was fitted by the Lowess smooth function in MATLAB show as Figure 2.4. An overlapping region has been added at the end of azimuth direction to keep the consistency of velocity trend after the fitting to spherical coordinates. Illustrated in Figure 2.5 C, we obtained a smooth velocity map based on spherical coordinates, and

into total 19 frames of the velocity map were generated through 3.5hpf to 9hpf. To apply the velocity data in to mesh movement with the finite element mesh, we embedded the velocity map to our finite element simulation frame. In the single time increment during the FEM simulation, the node will read the closed velocity scale based on its spherical position and calculate the displacement for the next time step. Due to the large deformation during epiboly, a remeshing scheme will be applied during the simulation. Details about the remeshing method will be discussed in Chapter 3.2.1.

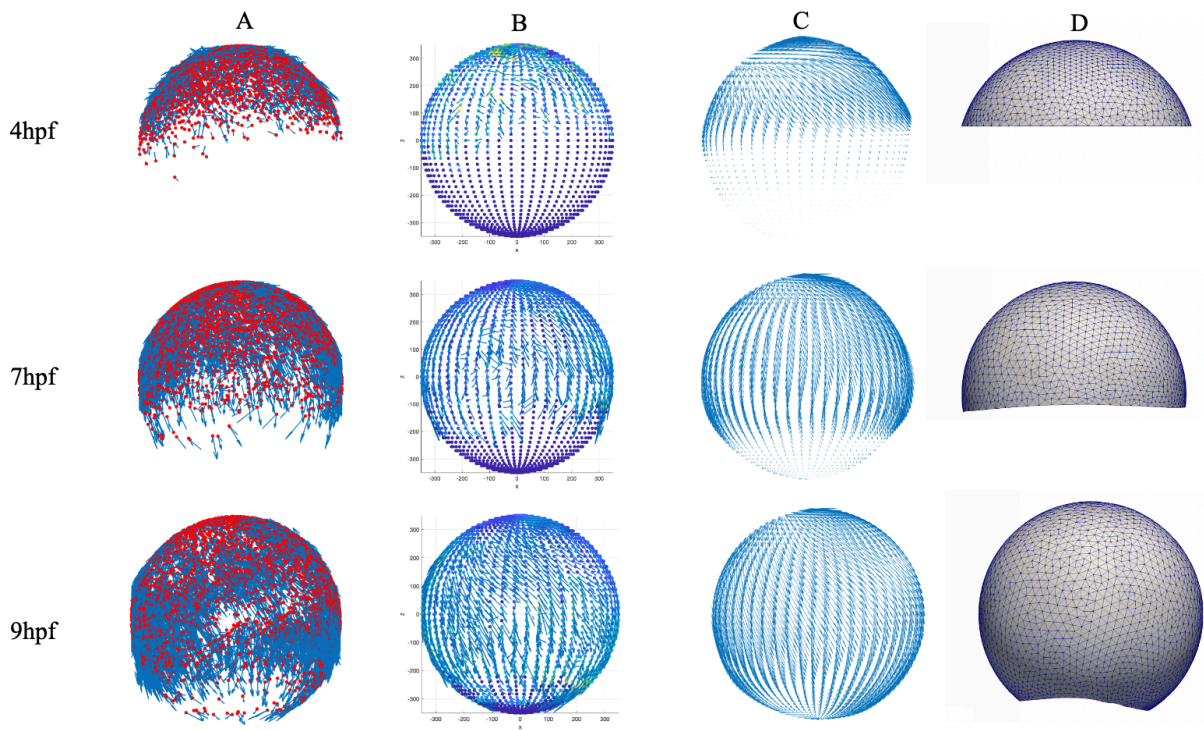


Figure 2.5. Generation processes of the 3D dynamic cell velocity map at different stages. Column A represents the real cell movement data mapped onto a spherical surface. Column B represents the averaged spontaneous velocity on an evenly distributed point cloud over the surface. Column C represents the functionally fitted and smoothed 3D dynamic cell velocity map based on spherical coordinate. Column D shows the finite element mesh movement guided by the dynamic cell velocity map.

2.2 Quantification of Spatiotemporal P-Smad image data

BMP is ligand that binds and activates its transmembrane receptor complex to directly phosphorylate the Smad5 (P-Smad5) transcription factor [88]. P-Smad5 subsequently accumulates in the nucleus and induces BMP target gene transcription [35], [95], [96]. Thus, the Smad5 is directly phosphorylated by the BMP type I receptor in response to BMP signaling, and P-Smad5 concentration has been shown to linearly correlate with the concentration of BMP ligand[88]. In our study, P-Smad5 fluorescence is used to compare against our model output by comparing the BMP gradient profile with the P-Smad5 profile.

In this study we utilized a quantitative immunofluorescence approach done by Zinski, et al at our collaborated group of Dr. Mary Mullins at University of Pennsylvania, to quantify nuclear P-Smad5 as the direct intracellular readout of BMP signaling. The data provided can directly visualize the P-Smad5 gradient at single-cell resolution embryo-wide and compare differences across mutant populations [51], [88], [97], [98]

Particularly, in our modeling approach, P-Smad5 data will be used to validate the reliability of the model. Both wild-type P-Smad and mutant P-Smad levels will be quantified and compared with the BMP concentration profile predicted by the mathematical model relatively. Different mechanisms will be tested in the mathematical model to assess which mechanism can produce predictions that align better with the experimental data.

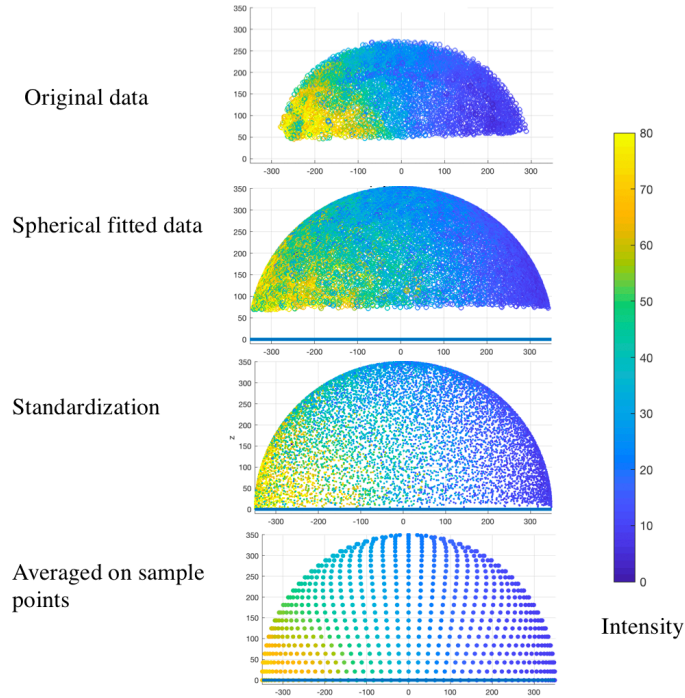


Figure 2.6. Data processing steps for P-Smad data. Color level indicates the intensity level at arbitrary unit.

To compare the P-Smad profile and our model output BMP gradient profile directly, we processed their data by fitting the original data to a standard sized hemisphere with different coverage along the elevation direction depending on the epiboly stage (4.7hpf for 40% epiboly, 5.7hpf for 50% epiboly, 6.3hpf for 60% epiboly). Different sets of experimental data in the same stage have been averaged on the evenly distributed sample points over the spherical domain to obtain the representative P-Smad level for this stage. Figure 2.6 demonstrates the details of our P-Smad data processing steps. Figure 2.7 and Figure 2.8 show the results of averaged P-Smad distribution profile over the whole 3D spherical domain for both wild-type and *Chd* mutant embryos. This data set will be directly applied into our modeling framework to validate the output BMP gradient and optimize our current model.

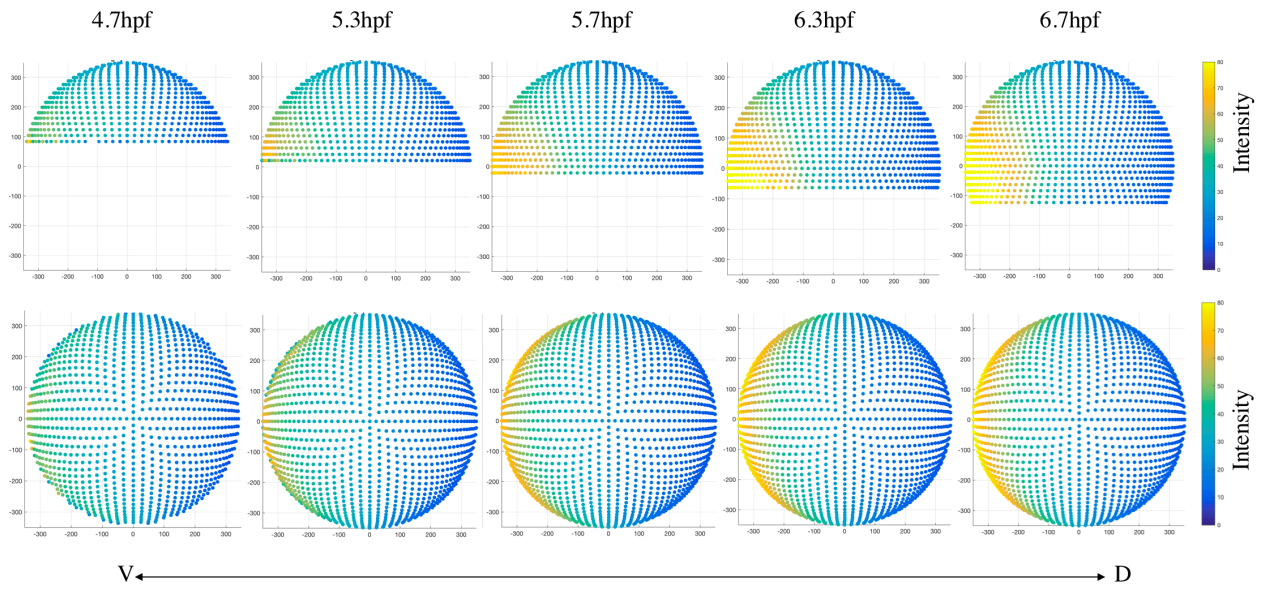


Figure 2.7. Averaged P-Smad distribution for wild-type at 4.7hpf, 5.3hpf, 5.7hpf, 6.3hpf and 6.7hpf

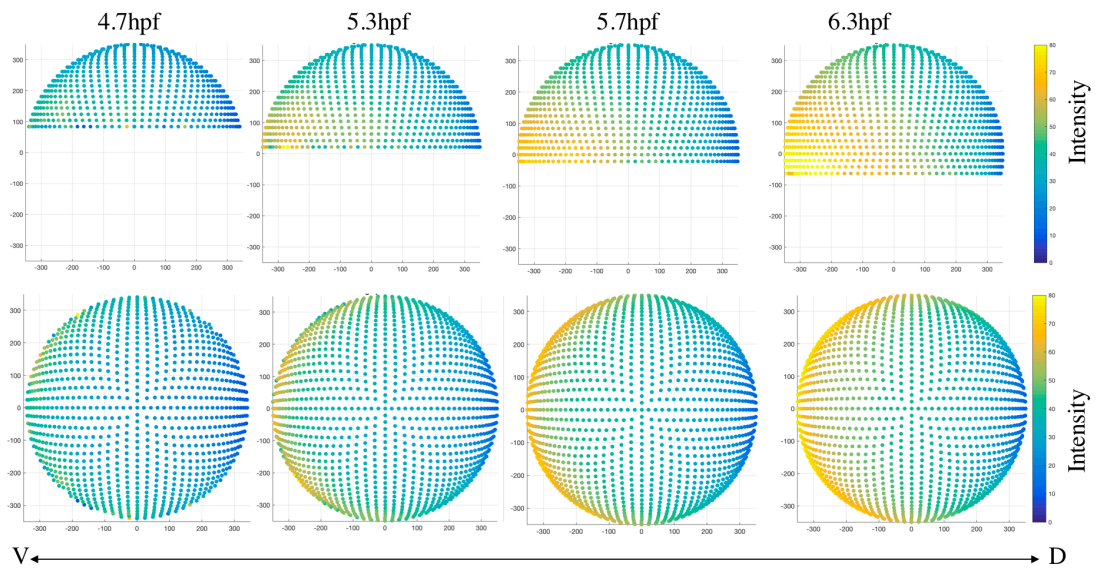


Figure 2.8. Averaged P-Smad distribution for chd mutant at 4.7hpf, 5.3hpf, 5.7hpf, and 6.3hpf

To have a better understanding of the relative level between different stages, we used a band of sample points around the margin and across the central region (from dorsal-most to ventral-most through the top of the animal pole) of the embryo to plot the profiles of overall P-Smad5 gradient between stages and between wild-type and Chd mutant embryos(Figure 2.9 and Figure 2.10).

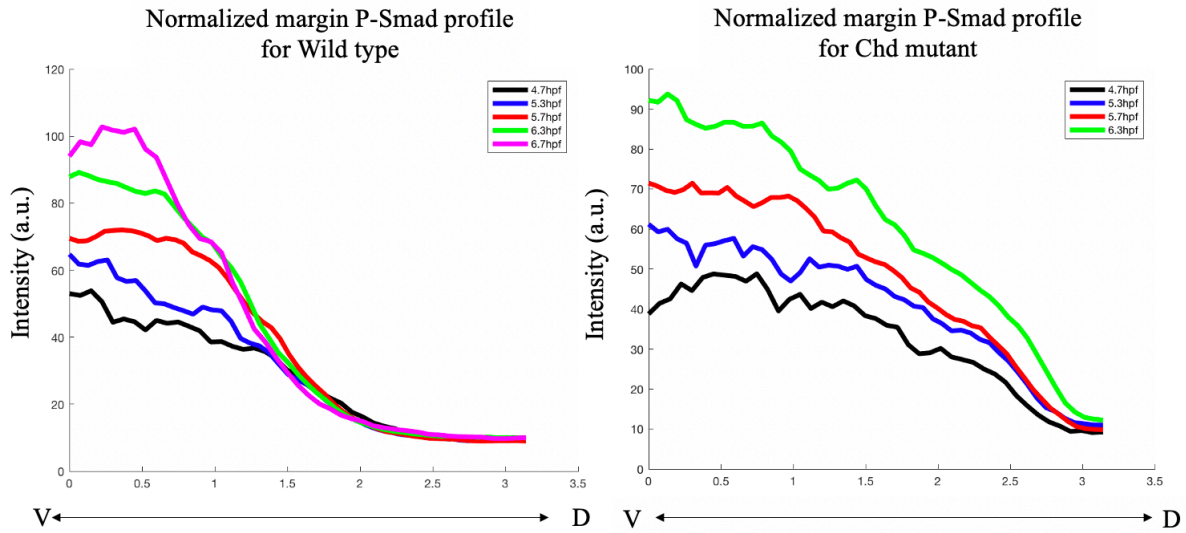


Figure 2.9. P-Smad profile at the margin for wild-type and Chd mutant

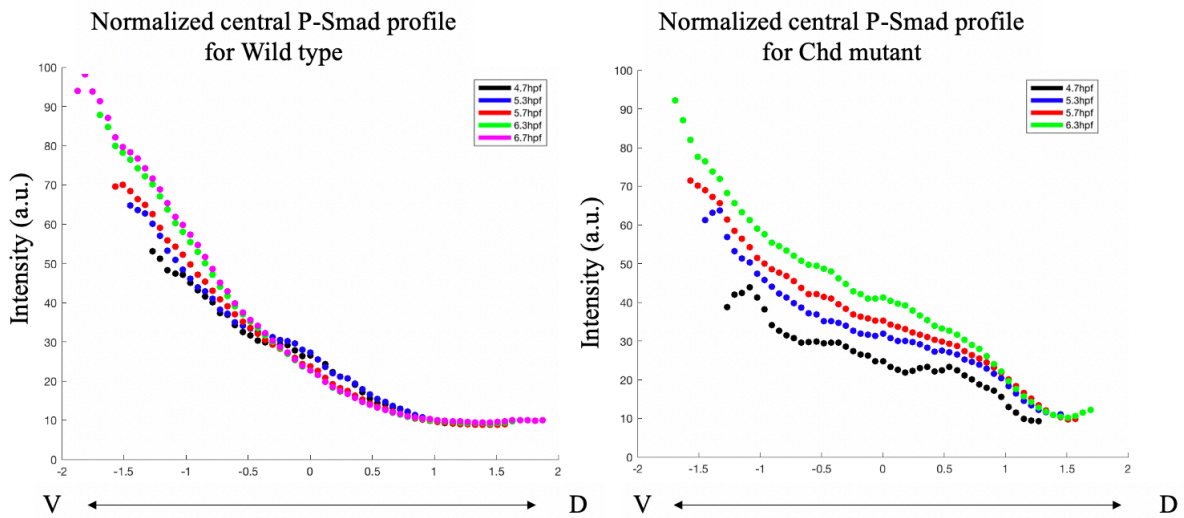


Figure 2.10. P-Smad profile at central for wild-type and Chd mutant

2.3 Quantification of Spatiotemporal target gene expression with whole-mount mRNA scope experimental data

On the other hand, through different techniques, experimental investigation in the zebrafish embryo can offer a wide variety of data mainly through visualizing the phenotypic structure and protein expression patterns in a partial or whole embryo.

Single-molecule fluorescence *in situ* hybridization (smFISH) has enabled detection of multiple mRNA spots in cells or embryos including *C. elegans* [99], *Drosophila* [100] and zebrafish [101], which is more quantitative than the traditional RNA *in situ* hybridization method. RNAscope, the higher-resolution smFISH method, allows the detection of lower expression levels of genes [102]. Quantified confocal fluorescent image data of *bmp2b* mRNA expression can provide the input profile to the BMP source term in the model.

To determine the values for source terms in the model, we imaged the spatial domains for expression of *bmp*, *chd*, *nog* and *sizzled* mRNA at embryonic stage 4.7hpf, 5.7hpf, 6.3hpf and 8hpf, throughout the embryo using the RNAscope method. The mRNA whole mount mRNA image data was collected by Dr. Xu Wang.

Figure 2.11 illustrates the whole-mount RNAscope image of *bmp2b*, chordin, and *sizzled* mRNA at 5.7hpf. Multiple individual mRNAs can be simultaneously detected by the RNAscope method at the cellular level in whole-mount embryos. *bmp2b* mRNA started to express since the zygotic stage, showing an obvious gradient pattern higher in the ventral, whereas *chd* mRNA expressed in the dorsal at 5.7hpf. The details of the experimental processes of RNAscope method can be found at Appendix A. We use the range of mRNA expression to represent the protein secretion of different species. Also, we developed methods to map BMP morphogen gradient formation and component gene expression quantitatively.

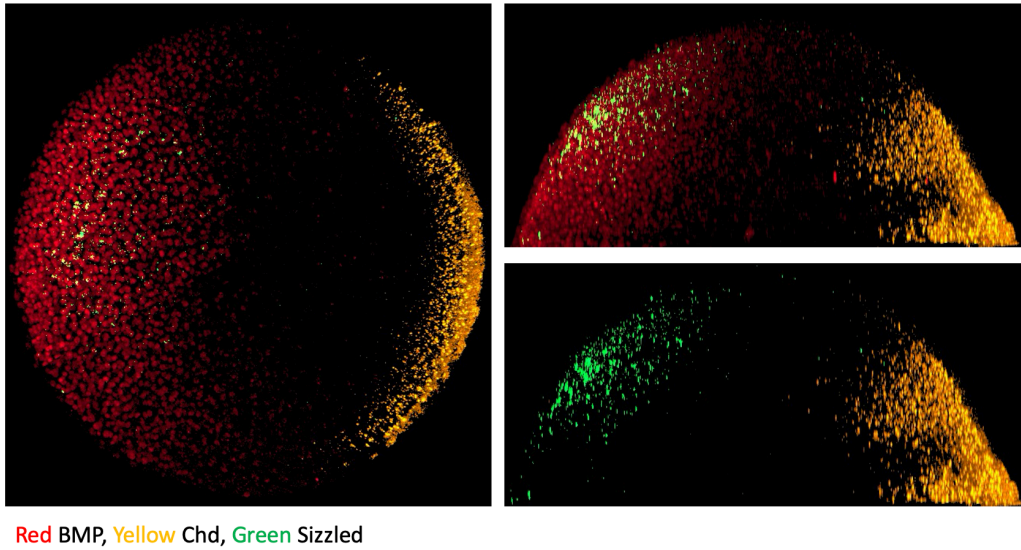


Figure 2.11. Whole-mount RNAscope image of *bmp2b*, *chordin*, and *sizzled* mRNA distribution.

mRNA segmentations, by the thresholding of spot intensity or watershed method, are well-used to quantify the number and intensity of single cells or tissues [103], [104]. We compared the method of both threshold of spot intensity and quantified the number of the single mRNA spots. Since the *chd* mRNA signal is very strong and high-intensity, spots overlapping with each other make it very difficult to distinguish a single spot. Thus, we chose to use the intensity threshold method to quantify the expression level of each species individually. We ignore considering the overlapping of mRNAs through the connect z-stack since the mRNA molecular should smaller than 2-3 micrometer in z-stack.

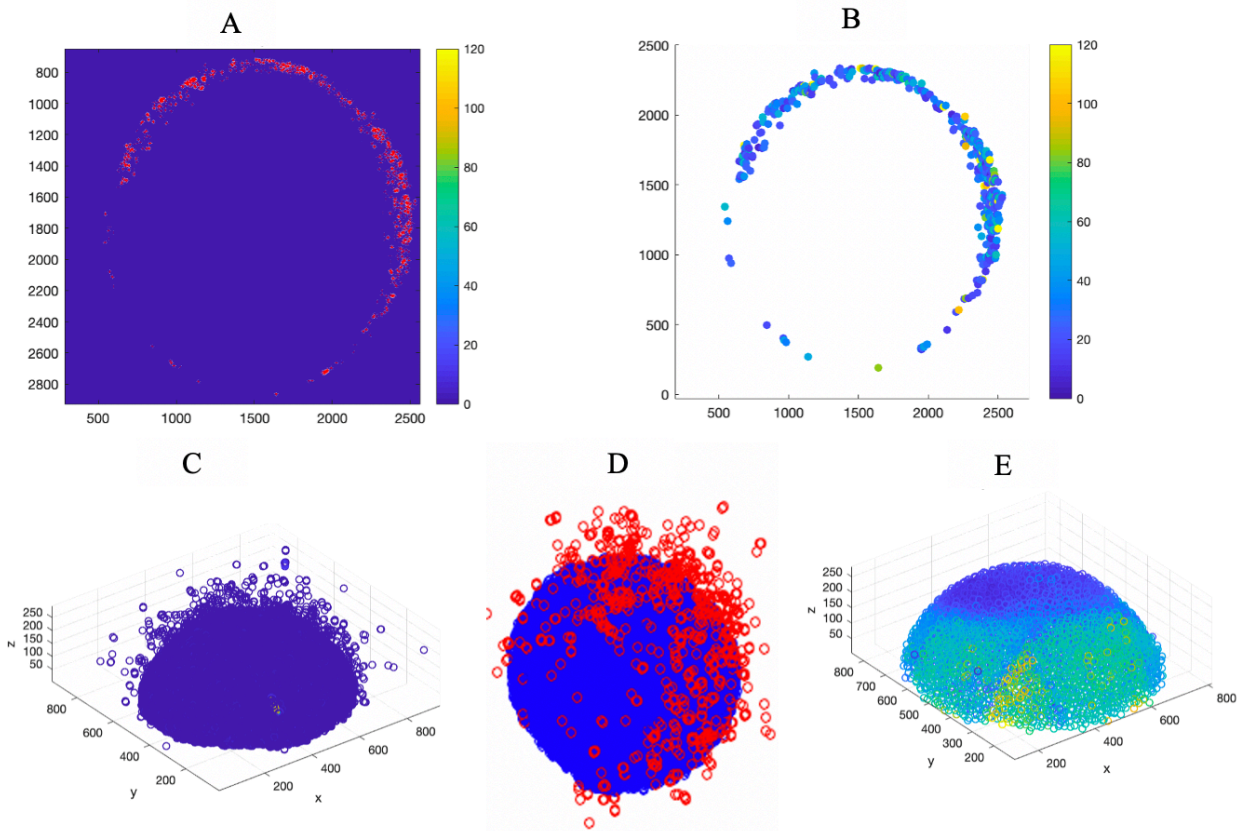


Figure 2.12. mRNA identification and noise of image processing scheme of the whole mount RNAscope experimental image. A. Original confocal image on a specific z-stack. B. mRNAs identified through hold method on a same z-stack. C. mRNAs identified over 3D space with noise D. Noise (Red) clearing process E. Noise cleaned data

We created a framework with a MATLAB-based package to identify all 200,000 + mRNA in each embryo in three dimensions to extract the BMP2b mRNA intensities. The details of the workflow of mRNA identification are shown in supplemental Figure S1. First, prerequisite intensity drop-off corrections were applied to the original image based on the drop-off of the nuclear intensity level through the depth of stacks which makes signal intensity reduced from the top of the image to lower stacks of the image as light is scattered when signal detection deepening into the lower layer of the embryos. Supplemental Figure S2 illustrated the original drop off level of nuclei channel and correction scheme. Then, single mRNA spots were identified through the intensity threshold method. Averaged and peak intensity level inside a single spot was saved with the position. Figure 2.12 shows a single slice of an original 3D image with the individual label of a single mRNA spot. Since the mRNA spots are generally densely distributed throughout the

expression domain, mRNA density around the single mRNA spot was used to eliminate the noise signal out of the range of the embryo region. Individual signal spots surround by distinguishable low density of other spots will be recognized as machine noise and eliminated. The red spots shown in Figure 2.12 represent the noise spot identified through this process. Cytoplasmic individual mRNAs can connect to one big spot, especially for *chd*. Potential big spots were extracted and separated when the spot intensity and pixel volume are larger than 3 times of the averaged value. The separated intensity was evenly distributed into an averaged grid point in the area, shown in supplemental Figure S3.

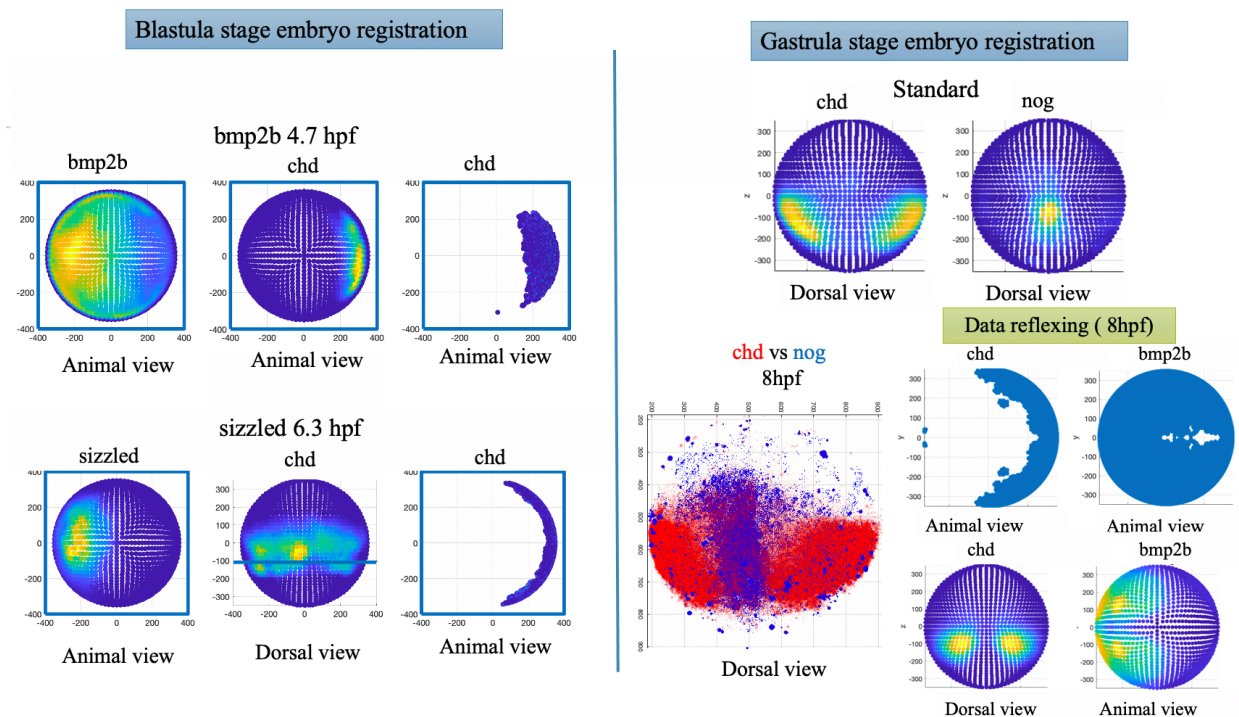


Figure 2.13. Embryo data registration for blastula and gastrula stages

To register the different embryo data along the DV axis, the dorsally expressed *chd* intensity level is used as a dorsal marker to identify the DV axis. The confocal image acquisitions were treated differently between 8hpf embryo with other stages because of the shape differences and limitation with the confocal as light is scattered when signal detection deepening into the lower layer of the embryo, and the signal is usually lost around 400mm depth at the z-stack level. The embryos before and at 6.3hpf were imaged with the upright objective in the same orientation with the marginal region facing to the bottom since the cell layer from the animal pole to the marginal

end is less than 400mm as the epiboly level is around 60%. However, at 8hpf as the epiboly level is over 80%, it is impossible to acquire data for the whole embryo within a single image, as with considering the embryo symmetrically divided by the DV axis, we collect the 8hpf data from the lateral view and manually mirrored the half embryo data to assemble as a whole embryo. The dorsal view of chd and nog expression data was collected and used as a standard to register the half embryo data based on the chd expression distribution. The individual embryo has been treated manually to register along the DV axis. Figure 2.13 demonstrates the detail of the registration processes for both blastula and gastrula stage data.

To apply it to our finite element model, we use mRNA data to determine the area of BMP expression. The data processing method used for mRNA data is similar to one applied on P-Smad data. The sampling area for calculating the average intensity overlapped with its close neighbors in order to a smooth expression map though out the spherical domain. To minimize the influence of the different nuclear densities, the individual sample intensity has been divided by the nuclei number in that sample area, shown in supplemental Figure S4.

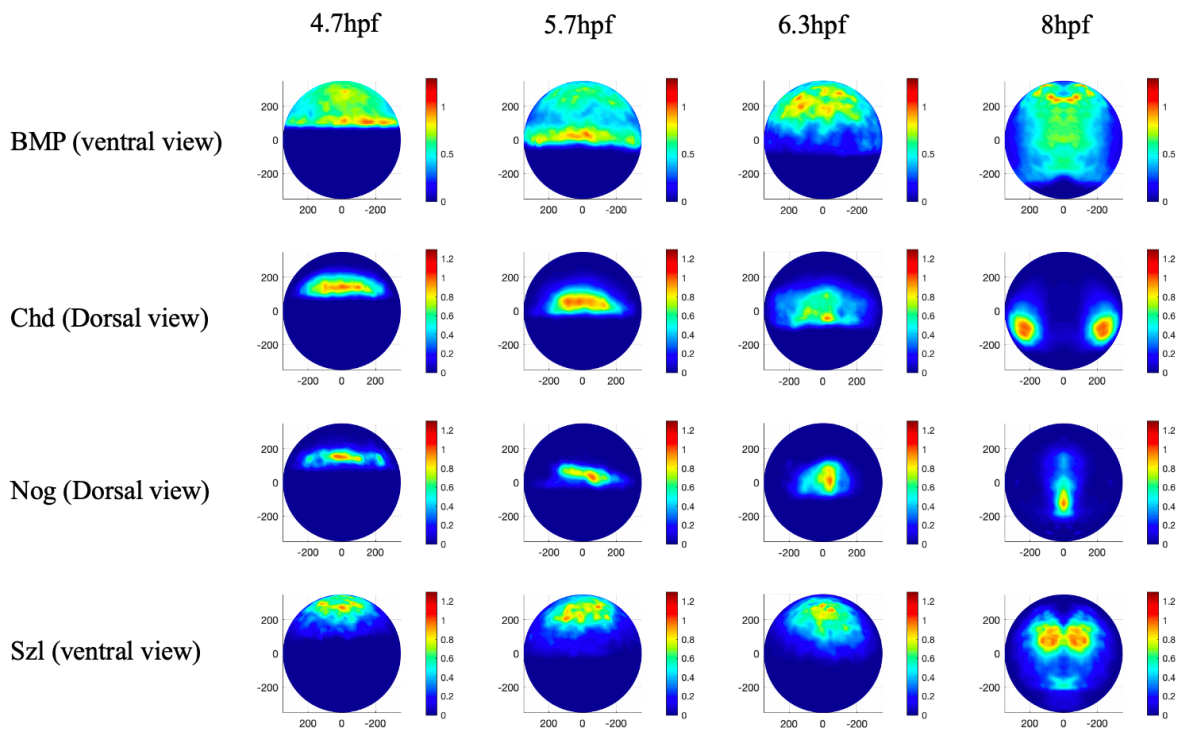


Figure 2.14. Averaged mRNA expression map for different proteins at individual development stages

Totally 98 embryo images have been processed, and different embryo data at the same stage were averaged to generate the average expression map. Figure 2.14 demonstrated the overall average map for four mRNAs (BMP, Chd, Nog, Szl) at four stages (4.7hpf, 5.7hpf, 6.3hpf and 8hpf). The list of embryo numbers averaged for individual genes at specific developmental stages is in supplemental Table 2. To apply the BMP expression data to our model, a dynamic map was created to locate the specific expression level spatially and temporally by linearly interpolating the data between different time points in a 2D spherical surface coordinate in azimuth and elevation angle, shown in Figure S5. Figure 2.15 illustrates the dynamic map interpolated on FEM mesh during the simulation. The dynamic map is used to precisely analyze and test the hypotheses of the gradient formation mechanism in our model.

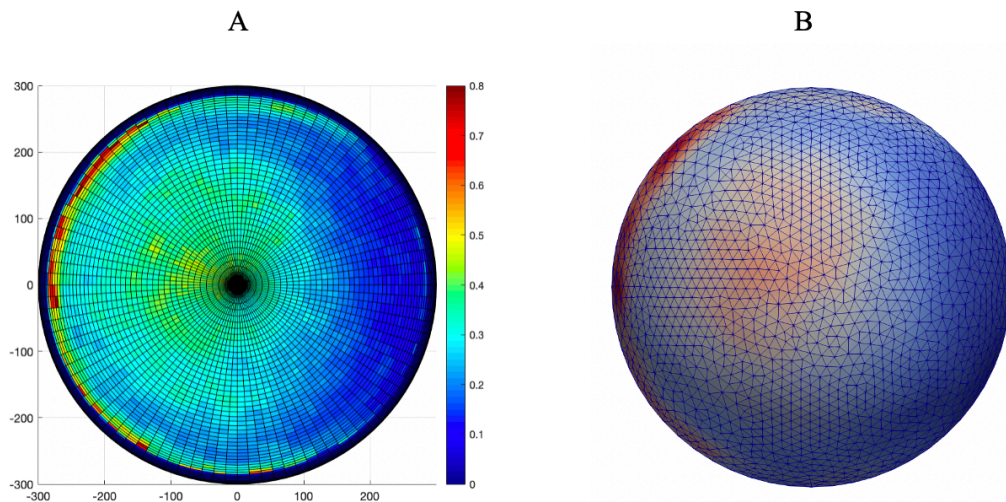


Figure 2.15. Dynamic expression map interpolated on FEM mesh. A, expression map for *bmp2b* mRNA at 4.7hpf on spherical grid. B, Interpolated expression level of BMP on FEM mesh.

3 EVALUATION OF BMP-MEDIATED PATTERNING IN A 3D MATHEMATICAL MODEL OF THE ZEBRAFISH BLASTULA EMBRYO

The content presented in this chapter is adapted from our work “Evaluation of Bmp-Mediated Patterning in a 3D Mathematical Model of the Zebrafish Blastula Embryo”, which was published in *Journal of Mathematical Biology*. Minor edits to the formatting have been made to produce a cohesive dissertation. The published version of this chapter is available at the following link: <https://doi.org/10.1007/s00285-019-01449-x>

Text reuse with permission.

3.1 Introduction

Pattern formation by morphogens drives the normal development of various processes such as limb development and organogenesis in animals [1]–[5], [105], [106]. In zebrafish, patterns of gene expression along the dorsal-ventral (DV) body axis are regulated by Bone Morphogenetic Proteins (BMPs) [10]. BMPs are a member of the TGF- β (transforming growth factor β) superfamily. Very early in embryonic development, both invertebrates and vertebrates require BMP signaling to pattern the DV axis [11], [12]. BMPs pattern DV tissues of zebrafish, *Xenopus*, and *Drosophila* embryos by forming a spatially-varying distribution, in which different levels of BMP signaling drive differential gene expression [29].

BMP signaling is propagated by the binding of BMP dimers to serine/threonine kinase receptors on the cell membrane. Type I and II receptors form higher order tetrameric complexes and phosphorylate intracellular Smads (P-Smad5 in zebrafish) that accumulate in the nucleus and regulate differential gene expression. BMP signaling is regulated by different molecules at multiple levels: extracellular, intracellular, and on the membrane [17]. These regulators form a system that enhances, lessens or refines the level of BMP signaling. One group of regulators are the inhibitors of BMP signaling [5], [29], [55]. BMP inhibitors include Chordin (Chd), Noggin (Nog), Crossveinless2, Follistatin, Sizzled, and Twisted gastrulation. [26], [44], [55], [107], [108], most of which act by binding BMP ligands, preventing them from binding their receptors. In this study, we focus on the major antagonists Chordin and Noggin. Chordin, unlike Noggin and Follistatin, can be cleaved by the metalloproteases Tolloid and BMP1a, releasing Chordin-bound BMP ligand and allowing it to bind receptors and signal [109], [110]. Downstream intracellular regulation of BMP signaling occurs throughout the BMP-Smad pathway [111]. Inhibitory Smads

modulate BMP signaling, either by interacting with Type I BMP receptors or by preventing R-Smads from binding Smad4. Others molecules, such as microRNAs and phosphatases may also act as intracellular modulators [112].

In our previous work, we developed a data-based 1-D model to investigate the mechanisms of BMP-mediated DV patterning in blastula embryos to early gastrula embryos at 5.7 hours post fertilization (hpf) before the initiation of BMP-mediated feedback (Zinski et al. 2017). We quantified BMP signaling in wild-type (WT), *chordin* mutant, and *chordin* heterozygous embryos. In our previous model screen, we simulated BMP gradient formation along a 1D line at the embryo margin and used the quantitative measurements of P-Smad to inform our model selection. We concluded that the signaling gradient patterning the vertebrate DV axis is most consistent with either a counter gradient or a source-sink mechanism. Measurements of BMP2 diffusion by fluorescent-recovery after photobleaching of $\sim 4\mu\text{m}^2/\text{sec}$ by ourselves and others, in addition to published estimates for the BMP2 lifetime, were more consistent with the source-sink mechanism than the counter gradient mechanism [85], [113].

These models lay the groundwork for our current study where we seek to add growth and 3D patterning to the model and test mechanisms of patterning in 3D. There is a significant need for spatially and temporally accurate 3D models of the early embryo to evaluate reaction-diffusion processes of chemical morphogens including BMP ligands. The development of accurate 3D models has been limited due to the complexity of embryo structure, and the computational resources needed to run parametric screens in 3D models. The work here builds off of previous work carried out by us and others. Previous work in *Drosophila* focused on a three-dimensional organism-scale model of BMP and gap gene patterning in the *Drosophila* embryo [8], [68], [86]. In zebrafish, the 3D structure shares some similarities but many differences with *Drosophila*, especially in regard to the growth during epiboly and the potential role of cell movement in shaping the gradient in the zebrafish. To date there are few mathematical models for zebrafish embryonic development and only one that developed a 3D approximation by Zhang et al. to study the role of Chordin in regulating BMP signaling in zebrafish [87]. This model focused on the blastula stage from 30% epiboly to the early gastrula shield stage (around 50% epiboly), however, it did not include growth, was not compared to data, and suggested a mechanism of BMP shuttling that has now been shown not to function in the embryo (Zinski et al. 2017).

BMP signaling begins patterning ventral tissues before the onset of gastrulation [10], [114], [115]. During gastrulation, coordinated cell movements organize the germ layers and establish the primary body axes of the embryo [15]. Epiboly begins during mid blastula stages (30–50% epiboly) and continues through the gastrula stage and entails a thinning and expanding of the cell layers from the animal pole, where the blastoderm lies, to cover the yolk cells over the vegetal pole [16]. The 3D model developed here accounts for this growth from 30 to 50% epiboly. The cell proliferation and movement during epiboly lead to a growth-like cell flow in the system. Such systems are often considered on a growing domain and many have incorporated domain growth into models of pattern formation [116], [117]. There are many ways and levels of detail that can be developed into a “growing” domain in a model and the appropriate choice depends on the physics of growth, the relative rates for new mass to enter the system, the ratio of processes that are involved in the transport of the molecules of interest among other considerations [118], [119]. In our first model for early zebrafish development that encompasses up to 50% epiboly, the approaches we considered include finite element modeling with a moving mesh or a simplified approach that simply adds mass at the leading edge to represent the movement of the cells further in the vegetal direction using a finite-difference solution approach. In this study, we used a growth domain finite-difference scheme that treats growth of the 3D simulation domain by adding new layers of mass near the leading edge of cells at the margin of the embryo at each growth step.

While our final goal is to develop a complete advection-diffusion-reaction model that incorporates all stages of zebrafish embryonic development, our current data and the development of the model herein that is tested against the data covers the first half up through 50% epiboly. It also serves as a greater test of the source-sink mechanism. Herein, we find that a Partial Differential Equation (PDE)-based model for BMP patterning of a zebrafish embryo with growth through epiboly demonstrates that the source-sink mechanism patterns well in 3D, however, sensitivity analysis suggests that the prepatterns of mRNA expression of BMP ligands and the inhibitor Chordin play a large role in dictating the overall shape and dynamics of the BMP gradient. Additional work is needed to quantify the gene expression domains and map them into the 3D modeling environment to improve the model for greater understanding of the inhibitors’ roles in shaping the gradient in 3D.

3.2 Method

We adopted our previous 1D model for the reaction-diffusion system simulated along a line for the margin [85] to our 3D geometry for the embryo growing domain model. The regulatory network in this study includes four individual components (BMP, Chd, Nog, Tld) and two bound complexes (BMP-Chd (BC), BMP-Nog (BN)). Figure 3.1H illustrates the regulatory network between different components: antagonists Chd and Nog inhibit BMP signaling by binding BMP ligands, and Chordin and BC complexes are cleaved by the metalloprotease Tolloid. To develop the model equations, a number of assumptions and simplifications are needed that are based on the biology and the questions being investigated. At minimum, we needed to determine if the mass-balance equations require both advective and diffusive terms for molecular transport, the structure of the reaction rate equations, and quantification of the sources of each of the components that may change over space and time.

We first estimated the potential role of advection in shaping the gradient based on our estimates for diffusion and the rates of cell movement in early development. We quantified the cell movement during epiboly by using the digital embryo data presented by Keller et al. [120] and quantified individual cell traces from 30% to 50% epiboly. To decide whether the advective transport caused by the cell movement or diffusive transport dominates the BMP concentration profile during blastula stages, we estimated the average Péclet number based on the cell tracing data from 4.7 to 5.3 hpf. As described in Chapter 2.1, we found that the median blastula stage Péclet number is 0.428 among all trackable cell traces in the embryo, thus, for the blastula stage embryo, we can assume this problem as a moving domain non-advection problem.

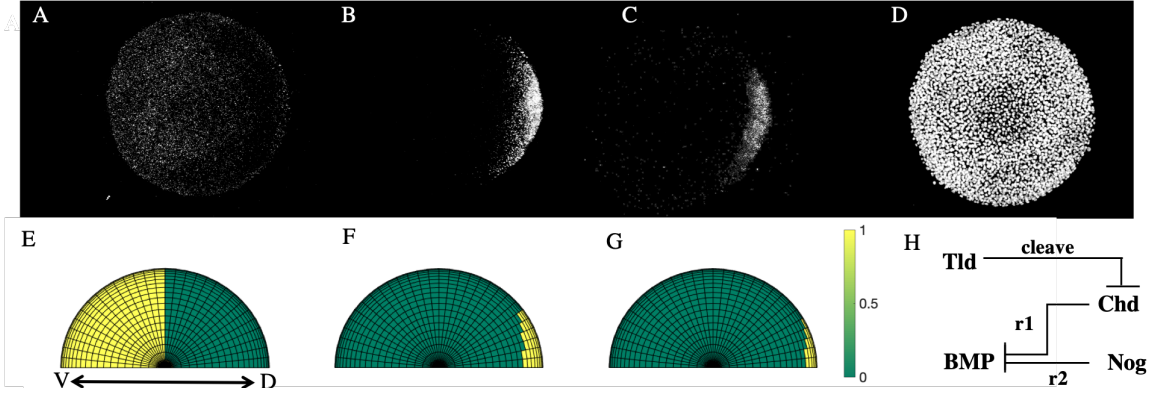


Figure 3.1. Whole mount experimental result of *bmp2b* (A), *chd* (B), *nog* (C) mRNA expression and nucleus positions (D), view from the animal pole. (E-G) Simulation input of expression area in WT for BMP, Chd and Nog, respectively. Yellow color indicates an area of production for each species. (H) Simplified BMP regulatory network used in this study.

Based on the regulatory network in our model Figure 3.1H, we firstly developed five-coupled non-linear partial differential equations (PDEs) model for BMP ligand, Chordin, Noggin, and the complexes of BMP-Chordin, BMP-Noggin. The model solves the spatial-temporal diffusion problem in spherical coordinates using the derivative in expanded form:

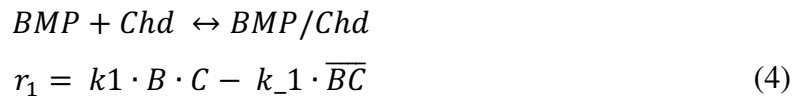
$$\frac{\partial C}{\partial t} = D\nabla^2 C \quad (1)$$

into

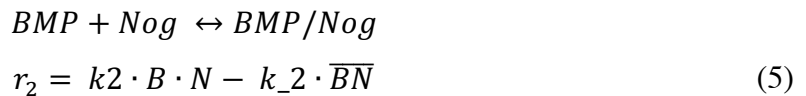
$$\frac{\partial C}{\partial t} = \frac{D_C}{r^2} \left(\frac{1}{\sin^2 \theta} \frac{\partial^2 C}{\partial \phi^2} + \cot \theta \frac{\partial C}{\partial \theta} + \frac{\partial^2 C}{\partial \theta^2} \right) \quad (2)$$

Note, C here represents a generic concentration, where C in the following equations represents the concentration of Chordin. The reactions between the different components are listed below:

The reaction of BMP ligand and Chordin ligand forming BMP-Chordin (BC) complex,



BMP ligand and Noggin form a BMP- Noggin (BN) complex,



(k_n and k_{-n} are the forward and reverse reaction rates, respectively).

The metalloproteases Tolloid (Tld) and BMP1a are lumped together and called *Tld* in this model and they function by cleaving Chd and Chd in the BMP-Chd complex.

The model for all the species involved is given by Equations below,

$$\begin{aligned} \frac{\partial B}{\partial t} &= \frac{D_B}{r^2} \left(\frac{1}{\sin^2\theta} \frac{\partial^2 B}{\partial \phi^2} + \cot\theta \frac{\partial B}{\partial \theta} + \frac{\partial^2 B}{\partial \theta^2} \right) + S_B - r_1 - r_2 + \lambda_1 Tld \cdot BC - k_b B \\ \frac{\partial C}{\partial t} &= \frac{D_C}{r^2} \left(\frac{1}{\sin^2\theta} \frac{\partial^2 C}{\partial \phi^2} + \cot\theta \frac{\partial C}{\partial \theta} + \frac{\partial^2 C}{\partial \theta^2} \right) + S_C - r_1 - \lambda_2 Tld \cdot C - k_c C \\ \frac{\partial N}{\partial t} &= \frac{D_N}{r^2} \left(\frac{1}{\sin^2\theta} \frac{\partial^2 N}{\partial \phi^2} + \cot\theta \frac{\partial N}{\partial \theta} + \frac{\partial^2 N}{\partial \theta^2} \right) + S_N - r_2 - k_n N \\ \frac{\partial BC}{\partial t} &= \frac{D_{BC}}{r^2} \left(\frac{1}{\sin^2\theta} \frac{\partial^2 BC}{\partial \phi^2} + \cot\theta \frac{\partial BC}{\partial \theta} + \frac{\partial^2 BC}{\partial \theta^2} \right) + r_1 - \lambda_1 Tld \cdot BC - k_{BC} BC \\ \frac{\partial BN}{\partial t} &= \frac{D_{BN}}{r^2} \left(\frac{1}{\sin^2\theta} \frac{\partial^2 BN}{\partial \phi^2} + \cot\theta \frac{\partial BN}{\partial \theta} + \frac{\partial^2 BN}{\partial \theta^2} \right) + r_2 - k_{BN} BN \end{aligned}$$

Since we limited the domain to the sphere surface, the diffusion in the r direction can be ignored. The above equation holds in the growing spatial domain Ω_t for all $0 < t < T$, where ϕ and $\theta \in \Omega_t$. B , C , N , BC , BN and Tld represent the concentration of BMP, Chordin, Noggin, BMP-Chordin complex, BMP-Noggin complex, and relative Tolloid, respectively. Tolloid is scaled and therefore dimensionless with a maximum of 1. D_i represents the diffusion rate for each species, S_i is the constant term of source for original expression of the specific gene which varies by its spatial distribution and reflects the experimental gene expression data for different species (Figure 3.1E, F, and G), λ_i is the Tld processing rate for Chd and BC complex, and K_i is the decay rate for specific ligands.

We approximated simple expression regions from confocal images to build the model. Various expression regions were tested for all three components (BMP, Chd, and Nog). Figure 3.1A illustrates a set of expression regions for BMP, Chd, and Nog that were tested. Notably, we applied a general gene expression data instead our gene expression map to the finite difference approach since we didn't finish the development of the image collection and processing framework at that time. For the simulations, the image data were converted into binary regions of expression and no expression. As shown in Figure 3.1, the BMP production region is limited to the ventral region, and Chd and Nog are limited to the dorsal side. As shown in Figure 3.1C, the Nog production region is smaller than the Chd production region.

The zebrafish embryo is approximated as a perfect hemisphere and the reaction-diffusion process happens on the surface of the sphere. Solutions were computed using the finite difference scheme based on the elevation and azimuth angles in spherical coordinates. Since the experimental result indicates that the development of the zebrafish embryo is symmetrical during the blastula

and gastrula stage, we only calculated our model in a quarter-sphere domain to decrease the computation and storage load. No-flux boundary conditions were applied for all species on both the ventral and dorsal boundaries, shown in Figure 3.2A. To avoid the singularity that happens on the top points where the elevation angle θ is equal to zero, we used a hollow-shaft approximation method presented by Thibault et al [121]. With this approximation, the mesh point $\theta = 0$ is eliminated by introducing a small but finite interior surface $\theta = f_{\theta}\Delta\theta$, and we used $f_{\theta} = 0.1$ in this study. The growth of the domain is achieved by adding finite-difference layers at the margin region in the elevation direction. Figure 3.2B illustrated the initial domain region (blue) compared to the growth domain region (orange) at 50% epiboly. Figure 3.2C shows the finite difference decentralization scheme based on elevation and azimuth angle on the spherical coordinate. The growth steps depend on the initial mesh density in the elevation direction and the smaller the mesh size in the elevation direction, the smaller the step size is used to model growth. We calculated the majority of solutions to the problem with step sizes for growth that balance model accuracy with computational cost. For faster screening within the large parameter space, we balanced at a 9 (elevation direction) by 15 (azimuth direction) mesh grid on the initial domain. Mass is added to the system by matching the concentration of the newly added node with the closest margin node of the previous time point. Example geometries and a time-lapse of a single solution are shown in Figure 3.3A.

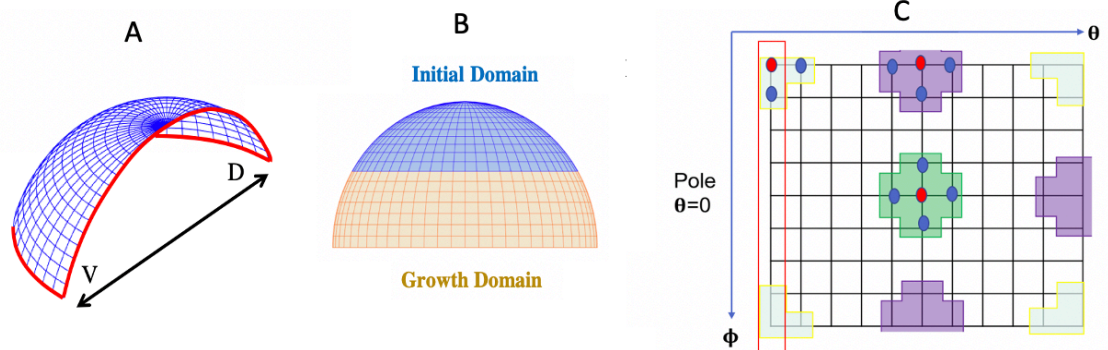


Figure 3.2. (A) Spatial domain at 3.5 hpf, Red open edges represent the non-flux boundary condition. (B) Initial domain (blue) vs later stage embryo domain (orange). Here we illustrate a 14 (elevation) by 31 (azimuth) initial mesh that requires 7 growth steps from 30% to 50% epiboly. (C) Finite difference discretization

To test the Partial Differential Equation (PDE)-based models developed herein, we used the previously published point cloud data for P-Smad5 (readout of BMP signaling) that is available online at Zinski et al. [85]. To apply these data to our model, we processed the data by fitting the original data to a standard size hemisphere with different levels of coverage along the elevation direction based on the embryonic stage of development. Different sets of experimental data in the same stage were averaged on the sample points over the globular domain to obtain the representative P-Smad level for each stage as shown in Figure 3.3 B.

To evaluate the system over a wide range of possibilities, we developed a computational model-based screen of over 300,000 combinations of biophysical parameters of the major extracellular BMP modulators. We applied a Monte Carlo parameter sampling strategy wherein parameters were randomly selected from a uniform distribution in log space that covered four orders of magnitude within the physiological range for each parameter. Each parameter was selected independently of the other parameters. The parameter ranges for sampling are listed in Table 1. After an initial wild-type simulation for each parameter vector, the model was re-simulated with Chordin production set to zero to simulate the BMP signaling gradient in a *chordin* loss-of-function (LOF) scenario. Based on previous studies [85], [113], the diffusion rate and decay of BMP ligand and Chd are fixed as constant, $4.4\mu\text{m}^2/\text{s}$ and $8.7 \times 10^{-5}/\text{s}$ for BMP, and $7\mu\text{m}^2/\text{s}$ and $9.6 \times 10^{-5}/\text{s}$ for Chd, respectively. The parameter space for the rest of the unknown parameters is shown in Table 3.1. The model is solved for the developmental window that spans from 3.5 to 5.7 hpf, and all measurements of model error are calculated at 4.7, 5.3, and 5.7 hpf.

Table 3.1. List of the parameter ranges used in the computational model-based screen. Values range between the upper and lower bound.

Parameters	Range	Best Fit	Unit
D_B (BMP Diffusivity)	4.4	4.4	$\mu m^2/s$
D_C (Chd Diffusivity)	7	7	$\mu m^2/s$
D_N (Nog Diffusivity)	$10^{-2} \sim 10^2$	0.58	$\mu m^2/s$
D_{BC} (BC Diffusivity)	$10^{-2} \sim 10^2$	25.89	$\mu m^2/s$
D_{BN} (BN Diffusivity)	$10^{-2} \sim 10^2$	5.09	$\mu m^2/s$
k_1 (Forward reaction rates for BMP and Chd)	$10^{-4} \sim 10^0$	0.14	$1/nM \cdot s$
k_{-1} (Reverse reaction rates for BMP-Chd)	$= k_2$	0.14	$1/s$
k_2 (Forward reaction rates for BMP and Nog)	$10^{-4} \sim 10^0$	2.56×10^{-4}	$1/nM \cdot s$
k_{-2} (Reverse reaction rates for BMP-Nog)	$= 0.1k_3$	2.56×10^{-5}	$1/s$
k_B (Decay rate of Ligand BMP)	8.7×10^{-5}	8.7×10^{-5}	$1/s$
k_C (Decay rate of Ligand Chd)	9.6×10^{-5}	9.6×10^{-5}	$1/s$
k_N (Decay rate of Ligand Nog)	$10^{-5} \sim 10^{-1}$	0.05	$1/s$
k_{BC} (Decay rate of Ligand BC)	$10^{-5} \sim 10^{-1}$	0.0015	$1/s$
k_{BN} (Decay rate of Ligand BN)	$10^{-5} \sim 10^{-1}$	6.87×10^{-4}	$1/s$
S_B (Production rate of BMP)	$10^{-2} \sim 10^2$	0.41	nM/s
S_C (Production rate of Chd)	$10^{-2} \sim 10^2$	17.34	nM/s
S_N (Production rate of Nog)	$10^{-2} \sim 10^2$	0.02	nM/s
λ_C (tld processing rate of Chd)	$10^{-4} \sim 10^0$	0.0016	$1/s$
λ_{BC} (tld processing rate of BC)	$10^{-4} \sim 10^0$	0.0022	$1/s$

3.3 Results

We identified the simulations generating BMP profiles that fit the P-Smad5 gradient at 4.7, 5.3, and 5.7 hpf as measured by a low normalized root mean squared deviation (NRMSD) for both WT and Chd LOF. Figure 3.3A demonstrates a simulation result for a WT case at these time points. The simulated BMP concentration level and measured P-Smad5 profiles (Figure 3.3B) are normalized between 0 and 1 to calculate the relative error (Figure 3.3C) between each profile for the entire domain. In our current simulations, we find good agreement throughout the embryo,

except on the ventral-anterior side and the lateral region between ventral and dorsal, that exhibits a relative error of ~12% (Figure 3.3C). The current best-fit parameter set is listed in Table 3.1. List of the parameter ranges used in the computational model-based screen. Values range between the upper and lower bound.. Compared with the biophysical requirements and fitness from the 1D model screen of Zinski et al., the result is consistent with the source-sink mechanism in which BMP diffuses from its distributed source to a sink of dorsal Chd. Overall, the simulation results match the trend with the experimental P-Smad5 profiles throughout the entire 3D domain. As the simulation progresses, the difference accumulates in the ventral-anterior region and at the lateral portion of the margin for later stages. The likely source for this error is the assumption of binary expression domains (Figure 3.1E-G).

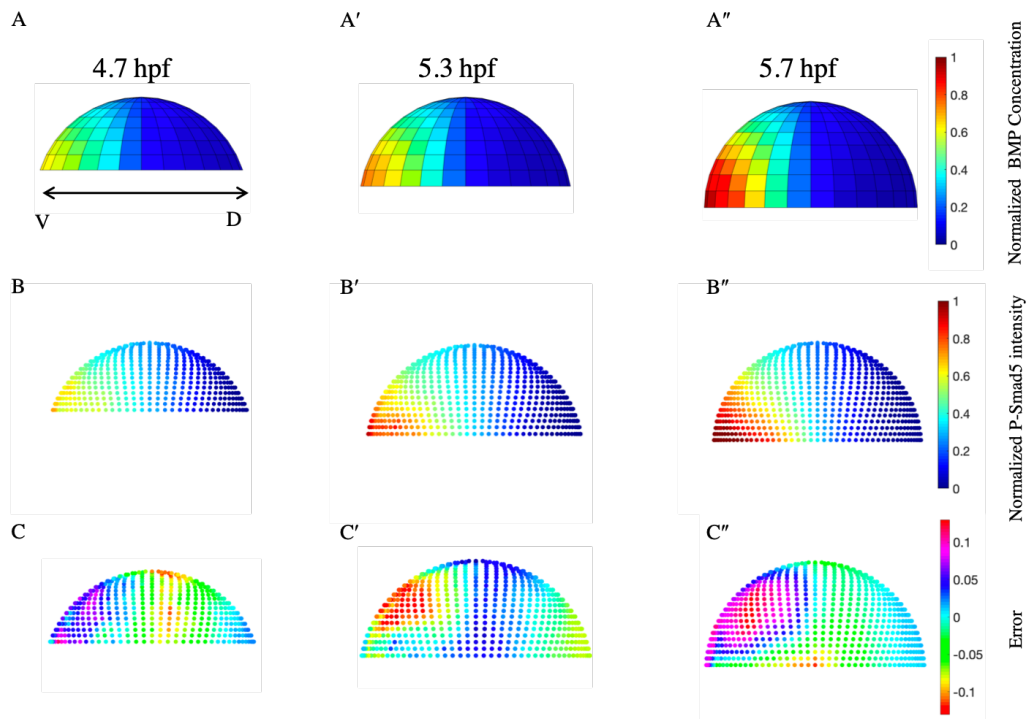


Figure 3.3. A, A' and A'', Normalized simulation result of a wild type case at 4.7 hpf, 5.3 hpf, and 5.7 hpf. B, B' and B'', Averaged and normalized P-Smad5 profile of 4.7 hpf, 5.3 hpf, and 5.7 hpf embryos. C, C' and C'', Relative differences between simulation results and P-Smad5 level.

Positive error indicates the experimental data are higher than simulation results, negative error indicates the experimental data are lower than simulation results. The results show in this figure illustrated with 9x15 mesh in the initial domain.

To clarify the differences between simulation results and P-Smad profiles, we isolated the profiles along the embryo's margin and central region for WT and Chd LOF in Figure 3.4 for the current best-fit model. The central region is defined as the region connecting over the animal pole the ventral- and dorsal-most points of the embryo. Thus, for different growth stages, the number of indices measured radially along the margin remains the same, but the central region covers increasing radial portions with progress through epiboly. The relative level of BMP ligands on the margin region agrees with the experimental P-Smad5 profile for different time points (Figure 3.4A and C). However, the central profile shows a gap for the Chd LOF model. Compared to the experimental profile, which has a nearly linear drop from the ventral to dorsal region, the simulation results' profiles show a stronger sigmoidal shape. Again, this may be caused by the sharp boundary of BMP production in the lateral region between ventral and dorsal or the sudden appearance of inhibiting Chd ligands. Based on the current data [85] the P-Smad5 gradient in *chordin* mutants showed a statistically significant increase in lateral regions of the embryo during these time points. Our results demonstrate the WT model has relatively better fitness on the central line compared to the Chd LOF model (in Figure 3.4 A-D) where the Chd LOF simulation overestimates at the early time points. The fitness at 4.7, 5.3, and 5.7 hpf for WT exhibits an overall consistency and solutions lay within one standard deviation of the measured mean, however, the earlier 4.7 hpf timepoints between the model predictions and P-Smad data for the Chordin mutants show greater differences along the line that travels through the animal pole (central, in Figure 3.4 D). This phenomenon appeared in all reasonable fits from the screen.

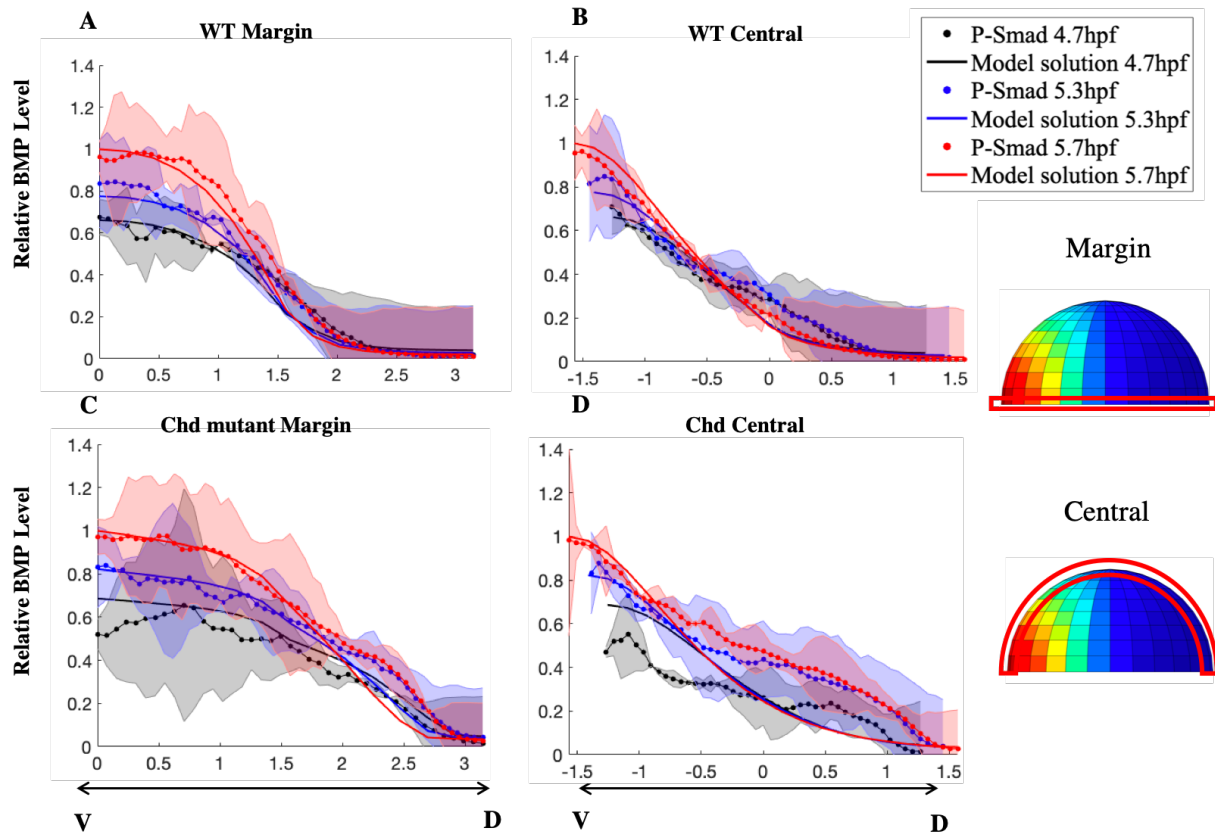


Figure 3.4. BMP distribution of a single modeling simulation result compared with the P-Smad 5 profile. A, WT case profile in the margin region. B, WT case profile in the central region. C, Chordin LOF case on margin region. D, Chordin LOF case on central region. All graphs are from ventral to dorsal as indicated below x-axis in C, D. Black color represents 4.7 hpf, Blue color represents 5.3 hpf, Red color represents 5.7 hpf. The shaded region indicates standard deviation for individual experimental data, represented by the dotted line. The x-axis indicates the radial position.

To determine how sensitive the solutions are to the model parameters and identify the likely contributors to the data-model mismatch, we developed a local sensitivity analysis and we also carried out principal component analysis (PCA). In our work, PCA did not identify clear correlations amongst parameters to principal components in models that fit the available data. We relied more heavily then, on parametric sensitivity, and Figure 3.5 A-D shows the parameter space for different unknown parameters vs. error between normalized simulation results and P-Smad5 averaged intensities. The best parameters among 300,000 random sets were chosen as the starting point to test the local sensitivity. Compared to other unknown parameters, the production-related parameters demonstrate the greatest sensitivity for the simulation error. As shown in Figure 3.5A,

the model fitness changed most in response to BMP and Chd production rate changes, where the smallest error of 5% occurred with BMP production at 0.4 nM/s and Chd at 17.7 nM/s . Interestingly, model fitness does not vary with Nog production rate. The current best fit parameter set is a Chd dominant model, where the production rate of Chd (17.34 nM/s) is much higher than the Nog production rate (0.02 nM/s). Thus, the WT model sensitivity shows that Chd dominates the sharp BMP gradient profile rather than Nog, consistent with previous 1D modeling results [85].

Since the decay rates and diffusivities of BMP and Chd are fixed based on measurements [85], [113], the local sensitivity for the decay rates and diffusivities of Nog, BMP-Chd complex, and BMP-Nog complex are compared in Figure 3.5B and C. The model shows limited sensitivity to the decay rate of BMP-Chd. The model fitness is not sensitive to the decay rate and diffusivity of Nog. The Tld processing rate of Chd and the BMP-Chd complex show similar and relatively large sensitivities. The best Tld processing rate of Chd appears at $1.6 \times 10^{-3} / \text{s}$, and model fitness worsens considerably when the Tld processing rate of BMP-Chd complex increases beyond $4.1 \times 10^{-3} / \text{s}$. Also, the model shows less sensitivity to the association constant for BMP/Chd and is insensitive to the association constant for BMP/Nog. The parameters related to Noggin show minimal effects on model fitness based on our current results. On the contrary, the model is sensitive to the Chd-related activities (Chd production, Decay rate of BC complex, BC diffusivity, and Tld processing rate of Chd and BC complex). This also indicates that a precise production region of the major components (BMP, Chordin, Noggin and Tld) and production rate of them could be the critical factors that increases the fitness quality of our current model. The high sensitivity to the current Tld model (linearly dependent on rate and concentration) also suggests that a more detailed protease model is needed to know how Chordin is restricted to the dorsal side required for shaping the BMP gradient.

Since, we use the range of mRNA expression to represent the spatial organization of protein secretion of different components and due to our previous work showing sensitivity to the spatial distributions in the 1D model, we carried out a deeper sensitivity analysis of these terms. To relate the model to the observed phenotypes, we tested how the secretion range of BMP, Chd, and Nog will influence the maximum concentration level of BMP ligands by using the same best-fit parameter set. Shown in Figure 3.5E, as the range of BMP secretion increases, the maximum BMP ligand concentration increases. On the other hand, as Chd decreases, the maximum concentration level of BMP ligand increases and leads to a dramatic increase when Chd range is less than 10%

of the embryo length. Shown in Figure 3.5F, we compared the changes of the normalized BMP profile in the margin and central region with respect to changes in the ranges of secretion. As BMP expression widens, the BMP ligand concentration profile widens in the margin but does not lead to a substantial difference in the central region. Alternatively, as Chd expression widens, it sharpens the BMP ligand concentration profile and limits the BMP ligand range for both the margin and central region (Figure 3.5G).

While our final goal is to develop a complete advection–diffusion–reaction model that incorporates all stages of zebrafish embryonic development, within our first approach and data the development of the model herein that is tested against the data cover the first half up through 50% epiboly. It also serves as a greater test of the source-sink mechanism. Herein, we find that a Partial Differential Equation (PDE)-based model for BMP patterning of a zebrafish embryo with growth through epiboly demonstrates that the source-sink mechanism patterns well in 3D, however, sensitivity analysis suggests that the pre patterns of mRNA expression of BMP ligands and the inhibitor Chordin play a large role in dictating the overall shape and dynamics of the BMP gradient. Additional work is needed to quantify the gene expression domains and map them into the 3D modeling environment to improve the model for a greater understanding of the inhibitors' roles in shaping the gradient in 3D.

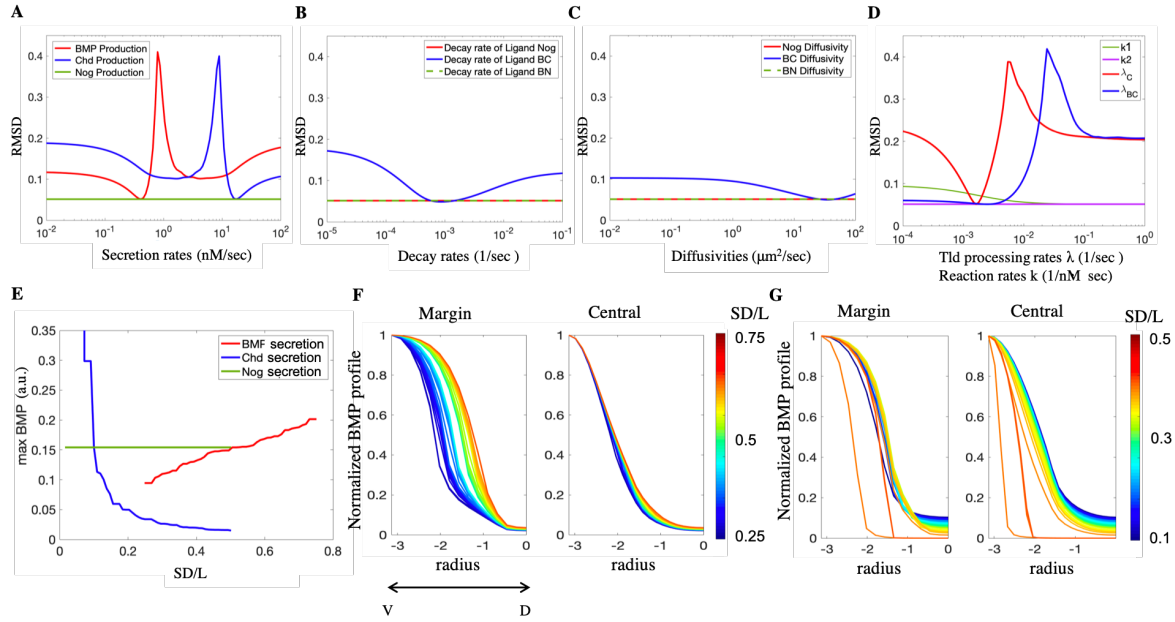


Figure 3.5. Local sensitivity analysis for unknown parameters. A, the production rate for BMP, Chd, and Nog. B, the Decay rate for Nog, BMP-Chd complex, and BMP-Nog complex. C, Diffusivity of Nog, BMP-Chd complex, and BMP-Nog complex. D, Tld processing rate of Chd and BMP-Chd complex (1/s), 2nd order constant for BMP/Chd (k_1) and BMP/Nog (k_2) (1/nM·s).

For Figure A-D, the x-axis represents the parameters' value in the log scale. The y-axis represents the error of the simulation result for the normalized BMP ligand concentration compared to the normalized experimental P-Smad intensity. E, Relative maximum BMP concentration changes as secretion domains change with BMP, Chd, and Nog. The X-axis represents the proportion of secretion domain vs embryo length (SD/L). F. Normalized BMP profile at the margin and central line changed by a proportional range of BMP secretion. G. Normalized BMP profile on margin and central line changed by a proportional range of Chd secretion. X-axis represents the radial position from Ventral (left) to Dorsal (right). The Red line indicates a wider range of BMP or Chd secretion, respectively.

3.4 Discussion

One advantage of simulating the model on the 3D geometry proposed here is that it enables observation of the variation of the levels of components throughout a more realistic whole embryo domain. Though morphogen activity along the margin has offered preliminary insight into DV axis patterning, we observed greater differences between model and data along the margin vs. the meridian line that passes through the animal pole.

The major challenge for this study is the vast unknown parameter space and computationally expensive simulation. The 3D growing embryo scheme is considerably more complex compared to a fixed 1D or 3D model. Using the finite difference scheme, the model

growth increments are at a constant radial rate along the longitudinal direction and also along a regular shape, which limits our capability to introduce a more realistic embryo shape and incorporate the advection caused by the cell mobility during later epiboly. However, by controlling the mesh size and growth duration in 3D that considers both the spatial and temporal aspects of embryo-scale modeling, this system allows for a closer surrogate to the actual embryo geometry to test different mechanisms that 1D and fixed domain models cannot support.

Local sensitivity analysis provides evidence that the BMP gradient is sensitive to the parameters related to Chordin and Tld activities. Since the BMP gradient is most sensitive to the gene expression inputs for BMP ligand, Chordin, and Tld processing, future work is needed to determine the relative expression of each of these proteins and the relative levels and spatial distributions of their expression. We are collecting *bmp*, *chordin*, *noggin*, and *tld* quantitative mRNA wholemount expression profiles at different stages to directly address this question. Even though we constrained some of the biophysical parameters based on experimental evidence that we and others have collected, there are likely more optimal parameter sets that may have different local sensitivities than shown here. Resources for increasing the size of the computational screen as well as greater determination of the *in vivo* rate constants will narrow down the study further and overcome a primary weakness of the work presented here.

This work contributes to our long-term goal of developing 3D models of the embryo with growth and advective cell movement, quantitative gene expression, and feedback to determine the interplay of these processes on pattern formation. The study here is the first step and provides a 3D mathematical model on a growing domain and provides a computational framework to elucidate how the components work together to establish the BMP gradient at multiple time-points in the blastula embryo.

4 ACCELERATION OF PDE-BASED BIOLOGICAL SIMULATION THROUGH THE DEVELOPMENT OF NEURAL NETWORK METAMODELS

The content presented in this chapter is adapted from our work “Acceleration of PDE-Based Biological Simulation Through the Development of Neural Network Metamodels”, which was published in *Current Pathobiology Reports*. Minor edits to the formatting have been made to produce a cohesive dissertation. The published version of this chapter is available at the following link: <https://doi.org/10.1007/s40139-020-00216-8>

Text reuse with permission.

4.1 Introduction

Mathematical modeling is widely used to interrogate mechanisms of signaling in biological systems. Spatiotemporal control of biological signaling is constrained by physical laws such as conservation of energy, mass and momentum. These physical laws, under a continuum assumption, are represented through partial differential equations (PDEs). Mechanism-based PDEs of biological signaling networks involve many coupled variables through nonlinear relations and many parameters. Model calibration often requires the screening of a massive parameter space due to the complexity of the system and the limitations of experimental evidence. During embryo development, regulation of the body plan can be described by nonlinear systems of reaction-advection-diffusion PDEs of relevant proteins. Due to the complexity of the regulatory system and the physics involved, experiments alone are not enough to gain mechanistic understanding of pattern formation in embryos or to understand how cells pass information to each other over long distances. Rather, identifying the correct parameters of the PDE system that explain the observed data is essential to our understanding of the biology[8], [122]. Unfortunately, solving PDE models can be a computationally intensive task. The type of nonlinear PDEs appearing in morphogenesis and pattern formation have to be solved numerically with methods such as the finite difference method or the finite element method. Because of the high dimensionality of the input parameters specifying the PDEs, parameter calibration through random search involves running millions of PDE simulations[88]. Even with the unrealistic assumption that a single PDE evaluation takes on the order of seconds, the computational cost for the calibration task quickly adds up to weeks or longer. For more detailed PDE models accounting for realistic geometries, more proteins, other physical phenomena, and geometric and constitutive nonlinearities, the brute-force approach is

simply infeasible. Due to these problems, alternatives to direct PDE simulations are needed. One approach is to approximate the numerical simulation of a PDE system by another, simpler model - a metamodel.

Machine learning and data analytics have yielded transformative results across multiple scientific fields due to the explosive growth of available data and computing resources. In this review, we discuss the ability of powerful machine learning methods to accelerate the parametric screening of biophysical informed- PDE systems. Training a deep learning algorithm enables us to accurately identify a nonlinear map between high-dimensional input and output data pairs that replaces the direct numerical simulation of the PDEs. We propose to use neural network (NN) proxies to build these metamodels. Figure 4.1 illustrates the differences between the traditional PDE model approach versus the proposed NN meta-model. A NN proxy can give results that are very close to those of a PDE model while providing significant speedups for model evaluation. Here we review literature where these methods were utilized and then focus on an example system that models zebrafish embryonic patterning through an extracellular reaction-advection-diffusion system represented by PDEs for chemical components that evolve over space and time. This model is a prototypical example of a signaling network that can explain how complex patterns emerge in organisms during development. We show that the NN metamodel is capable of replacing the PDE solver over a wide and high-dimensional parameter space, while at the same time requiring a much smaller computational cost. As a consequence, we are able to do parameter calibration against a set of experimental data using the NN metamodel. The example shown here is a specific application of machine learning to replace physics solvers by inexpensive surrogates, but the methodology described in this manuscript extends to other models of morphogenesis and pattern formation which can be described in terms of PDEs. Finally, even though we focus on the reaction-advection-diffusion PDEs and on NNs, we review alternative machine learning algorithms and their application to different classes of physics solvers.

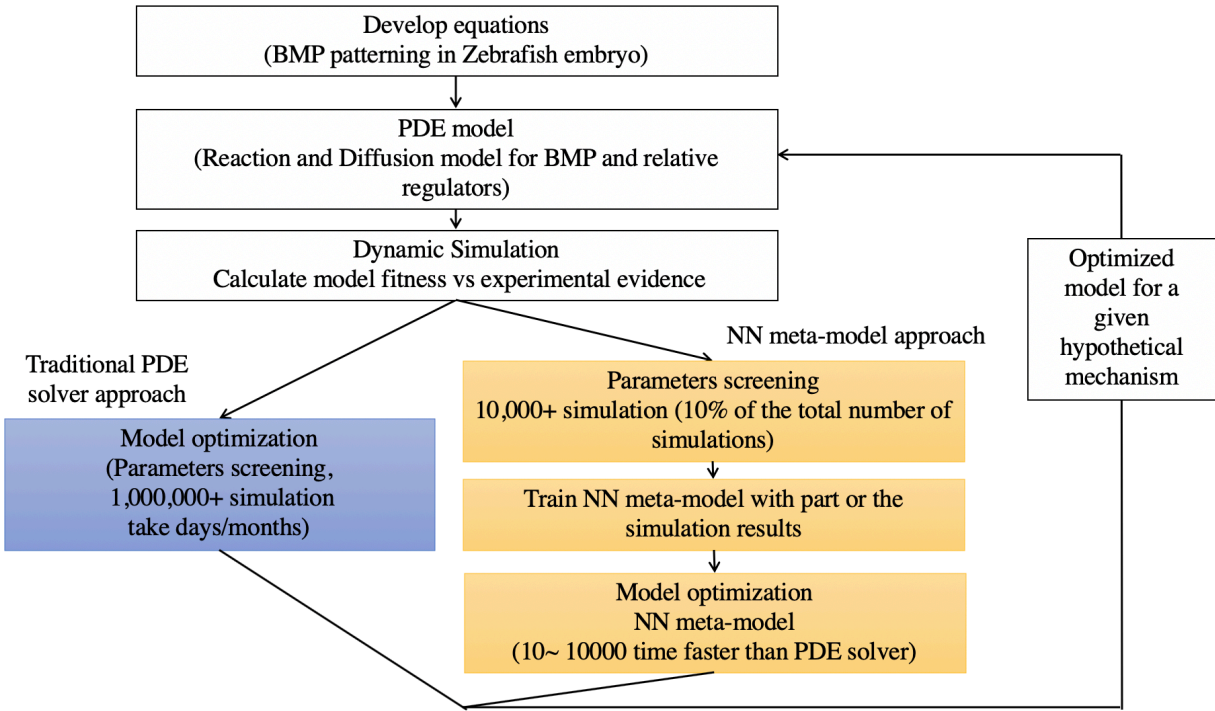


Figure 4.1 PDE modeling (blue) and meta-modeling (yellow)

4.2 Machine learning and deep learning

Machine learning encompasses a class of algorithms where a given task can be learned through implicit pattern recognition rather than by relying on explicit instructions. Machine learning can be split into subcategories: supervised learning, unsupervised learning and reinforcement learning[123]. Supervised learning involves fitting a function between inputs and outputs where the outputs have clearly defined labels that are to be exactly predicted by a machine learning model. It can be done either in the form of classification or regression. Some popular examples of methods used in supervised learning are Support Vector Machines (SVM), Naive Bayes classifiers, Gaussian Processes and Neural Networks [124]. Unsupervised learning involves finding patterns in data that does not have any labels. It can be done with k-means clustering, Gaussian Mixture Models (GMM) or also with Neural Networks [125]. Reinforcement learning (RL) involves an agent exploring an environment and attempting to find a sequence of actions that leads it to obtaining a highest reward based on reward function that was crafted by a human. Popular approaches to RL include policy gradient [126]and Q-learning [127] and usually use

Neural Networks. For other reviews about recent machine learning developments specially in the context of biological systems modeling, we refer the reader to [128], [129].

In recent years a subfield of machine learning called deep learning [130] has been gaining popularity due to advances in big data and massively parallel computer hardware[131]. Deep learning involves training NN with many layers. The number of layers needed in a NN model depends on the complexity of the task. Adding multiple layers allows the network to learn more detailed and more abstract relationships within the data and how the features interact with each other on a non-linear level. The networks are trained through backpropagation [132] and stochastic gradient descent (SGD) optimization. Some common SGD algorithms that implement an adaptive learning rate include Adagrad [133], RMSprop [134] and Adam [135]. The simplest NN architecture is a Multilayer Perceptron (MLP) where all nodes are fully connected. If the data involves sequences, then usually Recurrent Neural Networks (RNN) are used[136], [137]. A generic RNN diagram is shown in Figure 4.2. As shown on the diagram, the input at time s is combined with the hidden state h at time $s - 1$ to give output y at time s . Training RNNs is a bit more complex since it involves backpropagation through time where gradients are summed up for all time steps. Standard RNNs struggle with long sequences as gradients start to vanish if they are backpropagated though a long graph. To deal with this problem, Long Short-Term Memory Networks (LSTM) [138] were proposed where some gradients are allowed to be passed almost undisturbed. LSTMs are much more computationally expensive to train compared to MLPs.

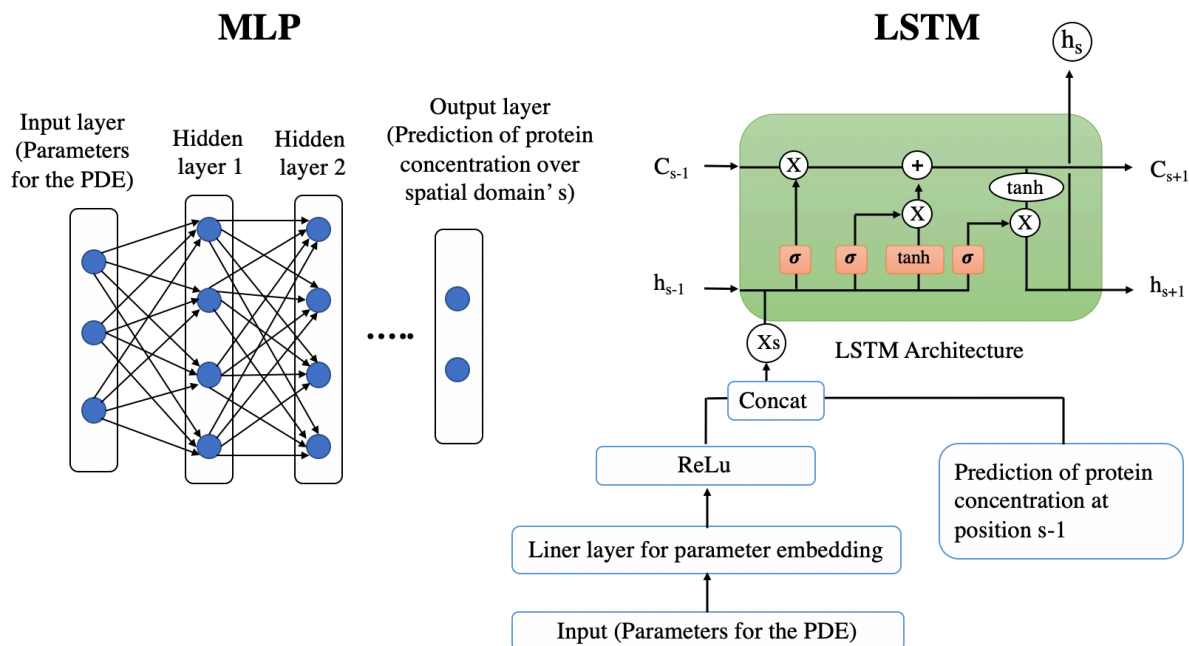


Figure 4.2 MLP vs LSTM model architecture

Input and output data type identification is critical to choosing the type of neural network. If the data involves 1D or 2D correlations to be explored like in speech signal or images, then Convolutional Neural Networks (CNN)[139] are used. Unlike in MLP, nodes of a CNN are sparsely connected to focus on spatial interdependencies.

4.3 Applications of machine learning to mathematical modeling

A major advantage of NN models is that nesting layers leads to the ability to interpolate highly nonlinear functions with a sequence of mostly linear steps. They are built primarily on basic linear algebra operations like matrix multiplications and convolutions which are highly parallelizable and run on the order of milliseconds unlike many scientific simulations. Hence if a NN metamodel could emulate a given mathematical model running on a computer then it could offer major advantages in terms of speed. Such use of NN has been seen in materials science, chemistry, physics, robotics and recently biology[140]. Furthermore, the predictions of the NN model includes scalars, prediction of a small set of discrete variables over all time, and prediction of spatial-temporal fields.

In the simpler cases, a NN model can be used to predict a single scalar. In the context of physics models, energy quantities are a common target for machine learning. For instance, take Schrodinger's Equation (SE), a fundamental tool in quantum mechanics. A problem of interest is to predict the potential energy as predicted by solving SE from particle positions. Similarly, potential energy for atomistic simulations or molecular dynamics simulations can be calculated as a single scalar output taking particle positions as input. Yet exact solutions are only possible for the smallest systems and otherwise expensive numerical approximations have to be used. To overcome this limit, [141] use a sum of weighted Gaussians to predict molecular energy based on the distance between molecules. The regression coefficients are found through kernel ridge regression on data generated with Density Functional Theory (DFT) which is taken as the ground-truth. They circumvent the task of explicitly solving the SE by training the machine learning algorithm on a finite subset of known solutions. Since many interesting questions in physics require repeated solutions of SE or molecular dynamics equations, the highly competitive performance of the ML approach is a boon for larger-scale exploration of molecular energies in chemical compound space[142]. The efficiency of the machine learning approach paves the way for large scale exploration of chemical compounds and their energies[143]. In [144] an MLP is used to predict the potential energy of a molecular system based on DFT calculations. What's notable is the authors carefully crafted a molecular representation as an input to the MLP. They took into account that the representation needs to be compact while maximizing resolution of the local atomic environment and covering all the relevant space the molecule occupies. They termed the resulting input as the Atomic Environment Vector (AEV). That is in line with other work in deep learning that shows that input representation matters. For example [145] shows they are able to narrow the gap in 3D object detection between stereo and LIDAR vision data by generating a pseudo-LIDAR representation from stereo data. One of major problems within materials discovery is to be able to identify stable compositions of chemical compounds. It is mostly done through expensive DFT calculations. In [146] they train an MLP to predict formation energy of a crystal based on Pauling electronegativity and ionic radius of species. They achieve very accurate results on garnets and perovskites. The ability of machine learning tools in predicting single scalars from the state of a complex multi-dimensional input space can help in accelerating the modeling of biological systems. For example, given a set of input parameters, a single scalar metric of interest

might be predicting the maximum expression of a given morphogen, or the total expression of a molecular species.

In some studies, NN models are used to predict a small set of discrete variables rather than a scalar, and in many cases the dynamics of these quantities are needed. In other words, predictions are needed over all time (or some time frame) for the set of discrete quantities. Dynamics simulators of this type are common in robotics. However, the rigid body dynamics models they employ can be very time consuming due to complex nature of the physics they are trying to capture. In [147] the authors use experimental data to train MLP and RNN to predict motion and sensory outputs of a robot based on its current positioning and kinematics. They developed various Simulator Neural Networks (SNNs) to capture different type of simulators. Depending on the specific simulator the prediction can either be a scalar or a set of motion locations over time. Accuracy tests indicated that NN simulators created for these robots generally trained well and could generalize well on data not presented during simulator construction. This approach increases effectiveness of building robust control system for robots. Even when part of the model is known, deep learning approaches can be used to learn unknown nonlinearities[148]. Another crucial yet very computationally costly problem in science is a three-body problem. In [149] the authors train an MLP to predict location of particles 1 and 2 given input of time t and initial location of particle 2. Location of particle 3 follows from problem symmetry. To acquire data, they used the Brutus numerical integrator and the time saved by using a NN is on the order of 100 million-fold. Such fast and accurate three-body solver has major implications for research into dynamical systems, especially to capture chaotic dynamics[150]. The ability of machine learning tools to predict the dynamics of complex systems might help accelerate discovery in biological systems. For example, instead of dealing directly with the PDE, the regulatory network can be considered as a 0-dimensional system leading to a system of ordinary differential equations (ODE). The ODE dynamics, including derivatives, can be captured through machine learning tools. This type of metamodel can either be used in the PDE solver to replace part of the computations, or it can be used by itself to at least delineate plausible parameter ranges before running the PDE solver[151].

The last type of ML algorithms we would like to showcase are those related to our problem of interest of accelerating PDE simulation for biological systems. For prediction of spatial-temporal fields, Wang applies neural networks to a mechanistic PDE model of pattern formation in bacteria[152]. Wang et al. trained an LSTM for a PDE system that calculates cell and molecular

concentrations for pattern formation in *Escherichia coli*. The model was non-linear and complex and simulated *E. coli* programmed by a synthetic gene circuit and the outputs of the model are cell growth and movement, intercellular signaling and circuit dynamics and transport and these outputs depended on PDE input parameters like the cell growth rate, cell motility rate and the kinetics of gene expression. Training data was generated by a PDE solver and their neural network achieved an R^2 of around 0.99 and provides speedup of about 30,000x. That carries great potential for efficiently exploring the parameters space of the PDE model and finding spatial distributions not easily seen before. Physics-constrained machine learning approaches have also received significant attention recently in the context of fluid and solid mechanics[153]–[155].

Most of the above work uses deep learning which scales better with increasing data sizes than more traditional machine learning approaches like SVMs and Gaussian Processes[156], [157]. For biological systems modeling, the number of chemical species that needs to be considered is large because regulatory networks are complex. In turn, a large set of parameters is needed. The output is also high dimensional. Deep NN have a fixed number of parameters (the weights and biases of the neurons) to represent these high dimensional input spaces and the nonlinear outputs. Thus, deep NN are a good choice considering the data here comes from simulation and is automatically labeled. Since it does not require strenuous manual annotation like vision, speech and text data, there is no limit other than time in generating training data through solution of the PDE systems. There are also multiple options for the type of NN used for acceleration. In some cases where data is sequential, as occurs in the simulation of physical systems over time, we can use RNNs to solve the problem. One thing that also weighs into the selection of NN is the tradeoff between speed and accuracy. RNNs operate in sequences and involve multiple linear layers in a single module which considerably slows them down compared to standard MLPs. Since inference latency is a crucial concern when emulating scientific simulations with neural networks, this disparity between MLP and RNN with MLP often having lower latency but potentially lower accuracy.

4.4 Mathematical modeling in developmental biology

One of the fundamental problems in developmental biology is how complex patterns in organisms emerge from a group of nearly identical cells. A major tool in understanding such

complex pattern emergence is to use reaction-diffusion mathematical models which model how molecular concentrations change over space and time [158]. Three major components of reaction-diffusion models are molecular transport, production and clearance. The reaction-diffusion PDEs involve many parameters, for example diffusion rate, production rate and decay rate of each protein. In order to get insight into the dynamics and interactions of the different molecules, the parameters of the PDEs have to be identified such that the simulations match experimental data. Moreover, we frequently want to find parameters that optimize the system for multiple different species or mutations in which case multi-objective or Pareto optimization is used[159].

Out of many proteins important for pattern formation in tissues, we are interested in Bone morphogenetic protein (BMP). In this review, we focus on the PDE model of BMP signaling network which patterns of gene expression along the dorsal-ventral (DV) body axis in early development of zebrafish embryo[38], [88]. BMPs pattern DV tissues of zebrafish, *Xenopus*, and *Drosophila* embryos by using a gradient-based mechanism, in which different levels of BMP signaling drive differential gene expression [29].

Previously, we developed both 1-D and 3-D modeling approaches to investigate the mechanisms of BMP-mediated DV patterning in blastula embryos through 5.7 hpf (hours post fertilization) before the initiation of BMP-mediated feedback[88], [160]. For the 1D approach, we assume the patterning region is on the margin line. For the 3D approach, the zebrafish embryo is approximated as a perfect hemisphere and the reaction-diffusion process happens on the surface of the sphere, shown in Figure 4.3. Using a hemisphere allows us to discretize the model using the spherical coordinate system. We solved the coupled non-linear partial differential equations (PDEs) for BMP ligand, Chordin, Noggin, Sizzled (in the 1D model only) and the complexes of BMP-Chordin, BMP-Noggin using finite difference method in MATLAB [160]. No-flux boundary conditions are applied for all species on both the ventral and dorsal boundaries for both 1D and 3D model.

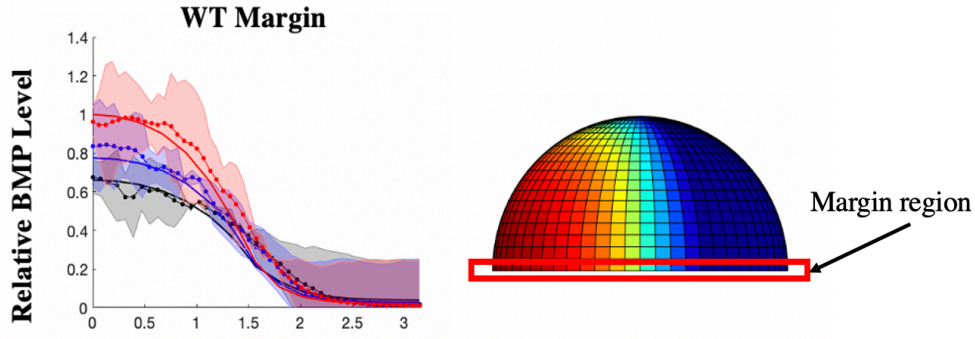


Figure 4.3 Illustration of the 1D vs 3D approach of PDE simulations on BMP concentration profile on Margin region/whole embryo region

As a general definition, the advection-diffusion-reaction PDE describing the changes in the concentration field of a chemical species $C(\mathbf{X}, t)$ in space $\mathbf{X} \in \mathbb{R}^n$ and time t can be stated as

$$\frac{\partial C}{\partial t} = D\Delta C - \mathbf{u} \cdot \nabla C + R + P$$

The first term in the right-hand side is the change in concentration due to diffusion. The Laplace operator acting on the concentration ΔC establishes that the concentration will flow in the direction of the negative gradient. Diffusion is parameterized by the constant D . The second term in the right-hand side is the advection term corresponding to the velocity field $\mathbf{u}(\mathbf{X}, t)$ and the concentration gradient ∇C . The velocity field is assumed to be known and to satisfy the continuity equation. The last two terms on the right-hand side are functions describing reaction and production of C . These functions could depend on C itself, could also depend on position and time, or even be functions of other fields.

For illustration, we consider a simple system of BMP regulation. Let $B(\mathbf{X}, t)$ denote the concentration field of BMP over some domain $\mathbf{X} \in \Omega \subset \mathbb{R}^n$, and $R(\mathbf{X}, t)$ the concentration of a regulator protein. The field $BR(\mathbf{X}, t)$ is the concentration of the BMP-regulator compound. In this example we ignore the advection term assuming that the tissue and cell populations are stationary and $\mathbf{u}(\mathbf{X}, t) = \mathbf{0}$. The system of equations describing local mass balance are

$$\begin{aligned} \frac{\partial B}{\partial t} &= D_B \Delta B - k_b B \cdot R + k_{ub} BR \\ \frac{\partial R}{\partial t} &= D_R \Delta R - k_b B \cdot R + k_{ub} BR \end{aligned}$$

$$\frac{\partial BR}{\partial t} = D_{BR}\Delta BR + k_b B \cdot R - k_{ub} BR$$

This system is parameterized by three diffusion parameters D_B, D_R, D_{BR} and two reaction rates k_b, k_{ub} . In order to actually compute the change in the concentration fields $B(\mathbf{X}, t), R(\mathbf{X}, t)$ and $BR(\mathbf{X}, t)$ over time and space, a few more ingredients need to be defined. First of all, the domain of interest $\Omega \subset \mathbb{R}^n$ has to be introduced. For example, as we will see later, we are interested in a surface that is a portion of a sphere. Boundary conditions also need to be specified. No-flux conditions at the boundary of the domain are a common and reasonable assumption. Lastly, the initial conditions $B(\mathbf{X}, 0), R(\mathbf{X}, 0), BR(\mathbf{X}, 0)$ are also needed.

Once the boundary value problem is fully specified, the next challenge is to solve it. Analytical solutions are not an option beyond extreme simplifications and assumptions. Instead, numerical methods are used to solve the PDE. There are several alternatives, depending on the characteristics of the PDE. We won't dive into the details of all possible approaches here. For the case of solid elastic or viscoelastic domains like the ones we are interested in, material points can be followed throughout the simulation. For these cases, structured grids or unstructured discretization are the most common. Structured grids allow the use of finite difference schemes to discretize the derivatives in the PDE but are limited to regular domains. Among unstructured grids, the finite element method allows to represent functions and derivatives on arbitrary geometries but increases computational cost. The time derivative also allows for different discretization strategies. Explicit time integration schemes bypass the solution of a linear system of equations but are only conditionally stable and may require extremely small-time steps depending on the nonlinearities of the PDE. Implicit time integration results in a possibly nonlinear system that needs to be solved for every time step but has the benefit of being stable for large time steps. The system of 3 equations introduced above for BMP regulation consists of only constant linear operators and therefore can be efficiently solved with implicit time integration schemes. More realistic models are often nonlinear.

In specific, we consider a PDE model of reaction-diffusion in zebrafish development that is represented by equations below. There are six proteins: BMP, Chordin, Noggin, BMP-Chordin, BMP-Noggin and Sizzled that interact with each other.

$$\frac{\partial B}{\partial t} = D_B \Delta B + \phi_B + \lambda_{tBC} \cdot \frac{1}{1+S/kit+(C+BC)/kmt} \cdot BC + \lambda_{aBC} \cdot \frac{1}{1+S/kia+(C+BC)/kma} \cdot BC - k_{onc} B \cdot C + k_{offC} BC - k_{onN} B \cdot N + k_{offN} BN - de_{CB} B$$

$$\frac{\partial C}{\partial t} = D_C \Delta C + \phi_C - \lambda_{tC} \cdot \frac{1}{1+S/kit+(C+BC)/kmt} \cdot C - \lambda_{aC} \cdot \frac{1}{1+S/kia+(C+BC)/kma} \cdot C - k_{onC} B \cdot C + k_{offC} BC - dec_C C$$

$$\frac{\partial N}{\partial t} = D_N \Delta N + \phi_N - k_{onN} B \cdot N + k_{offN} BN - dec_N N$$

$$\frac{\partial BC}{\partial t} = D_{BC} \Delta BC - \lambda_{tBC} \cdot \frac{1}{1+S/kit+(C+BC)/kmt} \cdot BC - \lambda_{aBC} \cdot \frac{1}{1+S/kia+(C+BC)/kma} \cdot BC + k_{onC} B \cdot C - k_{offC} BC - dec_{BC} BC$$

$$\frac{\partial BN}{\partial t} = D_{BN} \Delta BN + k_{onN} B \cdot N - k_{offN} BN - dec_{BN} BN$$

$$\frac{\partial S}{\partial t} = D_S \Delta S + \frac{V_S \cdot B^n}{k^n + B^n} - dec_S S$$

$$\frac{etaS}{V_S} = \frac{p \cdot b^n}{\frac{k^n}{B_0} + b^n}$$

The model has 23 unknown parameters and to learn the overall system behavior, a common approach is to screen a distribution of these parameters. Furthermore, for each set of parameters there are seven mutations for which experimental data is available: (wild type (WT), Chordin loss of function (CLF), Noggin loss of function (NLF), Bmp1a loss of function (ALF), Tolloid loss of function (TLF), Bmp1a and Tolloid loss of function (TALF), Sizzled loss of function (SLF)). Thus, a separate set of PDEs, each for a given mutation, is needed. The mutation simulation is based on the turning on/off of some specific parameters, for example in CLF simulation the Chordin expression is set to $\phi_C = 0$. The model has unknown and tunable parameters. Most of the variable parameters have to be randomly searched according to their ranges so that the outputs of the simulation match the experimental data. The fitness of the parameters is determined by Normalized Root Mean Square Error (NRMSE) between the final BMP distribution from the simulation and the experimental values. The values of S_{max} that are used to find appropriate reaction rate k_{it} and k_{ia} ranges are determined based on other simulations not discussed here.

4.5 Application on PDE acceleration through neural networks

In this section, we will discuss how we applied the neural network approach in PDE acceleration of the specific PDE system of BMP patterning in two different ways based on the type of data input and output. For this problem, this biological process happens on a developing

zebrafish embryo during blastulation and gastrulation. By assuming the patterning only happens on the margin of the cell group, this problem can be considered as a one-dimensional problem with the input of unknown parameters and output of 1D concentration profiles. On the other hand, by considering the spatial distribution of the cells and their movement, this problem can be considered as a three-dimensional moving domain problem with the input of unknown parameter space and 3D concentration profiles are generated at each node. For the 1D approach, we assume the patterning region is on the margin line. The inputs to the neural network are the PDE model parameters that are generated randomly according to the specific ranges. The output is the final distribution of BMP concentration in a 1D line with 36 nodes. Since the parameter values can take on an unknown number in the screen, and often over a very large range, both inputs and outputs are normalized by taking a logarithm of base 10 of all the values and then dividing the resulting values by 10. Also, any value less than 10^{-8} , including 0, is approximated to 10^{-8} . This way we ignore concentrations too small to be significant and avoid taking a logarithm of zero. To collect data for neural network training we run 100,000 parameter sets, each consisting of 7 different mutation for a total of 700,000 unique simulation data points. 90% of data is used for training and 10% is used for validation. We consider two neural network architectures: MLP and LSTM. In the MLP model, the PDE parameters are passed through a sequence of linear layers, each followed by Rectified Linear Unit (ReLU) activation function. The output layer gives the 1D distribution of BMP concentrations on the margin in 36 nodes at once. That is in contrast to an LSTM model, shown in Figure 4.2, where the BMP concentrations are output in a sequence over spatial locations, one by one through the calculation domain. Here the PDE parameters are passed first through a linear layer that gives a higher dimensional parameter embedding. Then the parameter embedding is concatenated with an LSTM output at a previous step in sequence and passed to an LSTM module which outputs the BMP concentration at the current point in sequence. A BMP concentration of 0 (-0.8 after normalization) is given as a dummy input at the first step of a sequence. The sequence length of LSTM is 36 since there are 36 points in space for the PDE model.

To match neural network outputs with actual PDE simulation outputs an L1 loss is calculated between the two. (Both L1 and L2 loss have been tested, L1 loss has better performance than L2 loss in our case) It is then backpropagated through the neural network to calculate the gradient at each weight of the neural network. Then the weights are optimized through the Adam algorithm with an initial learning rate of 0.001. The training is run for 100 epochs. In addition to

the L1 loss we consider another metric (NRMSE between NN prediction and direct PDE simulation result) to evaluate the performance of the neural network.

4.6 Results

Tables 4.1 and 4.2 show the validation set results of training different MLP and LSTM model for the 1D case. The MLPs are named with the format: MLP-number of layers-number of units. For example, MLP-3-256 means the model has 3 layers, first with 256 outputs, second with 256 outputs and third with 36 outputs. MLP-4-256 would have one more layer with 256 outputs. For LSTMs we consider modules with output sizes of 256 and 512. In addition to accuracy metrics like R^2 and relative error we also consider number parameters and computational cost metrics like number of floating-point operations (FLOPs), latency on a standard Intel CPU and latency on Titan X Pascal GPU. Among MLP models, MLP-4-1024 has the best accuracy while among LSTM models it is LSTM-512. We can also see that LSTMs models slightly outperform MLP models in accuracy. For example, LSTM-512 has the same number of learnable parameters as MLP-4-1024 with a relative error lower by over 1%. That is due to LSTM’s ability to understand sequences. However, that also comes with a bigger computational cost. All of FLOPs, CPU latency and GPU latency are more than 10x larger for LSTM- 512 than for MLP-4-1024. From here on we only consider the best MLP and LSTM models hence we refer to the MLP-4-1024 model as MLP and to the LSTM-512 model as LSTM.

Table 4.1. Comparing MLP models

	MLP - 3 -256	MLP - 3 -1024	MLP - 4 -256	MLP - 4 -1024
Parameters	0.0812M	1.11M	0.147M	2.16M
FLOPs	0.162M	2.22M	0.294M	4.32M
CPU latency	0.092ms	0.120ms	0.125ms	0.319ms
GPU latency	0.187ms	0.189ms	0.237ms	0.237ms
Rel.error	12.19%	9.57%	8.34%	6.99%

Table 4.2. Comparing LSTM models

	LSTM - 256	LSTM -1024
Parameters	0.533M	2.11M
FLOPs	37.9M	151M
CPU latency	5.96ms	12.4ms
GPU latency	5.51ms	5.67ms
R ²	0.9994	0.9996
Rel.error	7.67%	5.74%

Next, we investigate how the neural network model responds to the amount of data it is fed and how its error changes as training progresses. We only consider the MLP model here since the LSTM model is expected to give very similar trends. As expected, the accuracy improves as more samples are used. Using 100,000 samples gives satisfactory results. Results are acceptable for 10,000 samples and not good for 1000 samples. Such differences in accuracy based on number of samples are quite standard compared to other deep learning application where usually 10,000 training samples are needed for this number of inputs and the degree of nonlinearity. This table also shows importance of our relative error metric. For 1000 samples we get a high relative error while still a respectable R². That is because R² is calculated on normalized log values since calculating it on actual values would make those of larger magnitude dominate which we avoid.

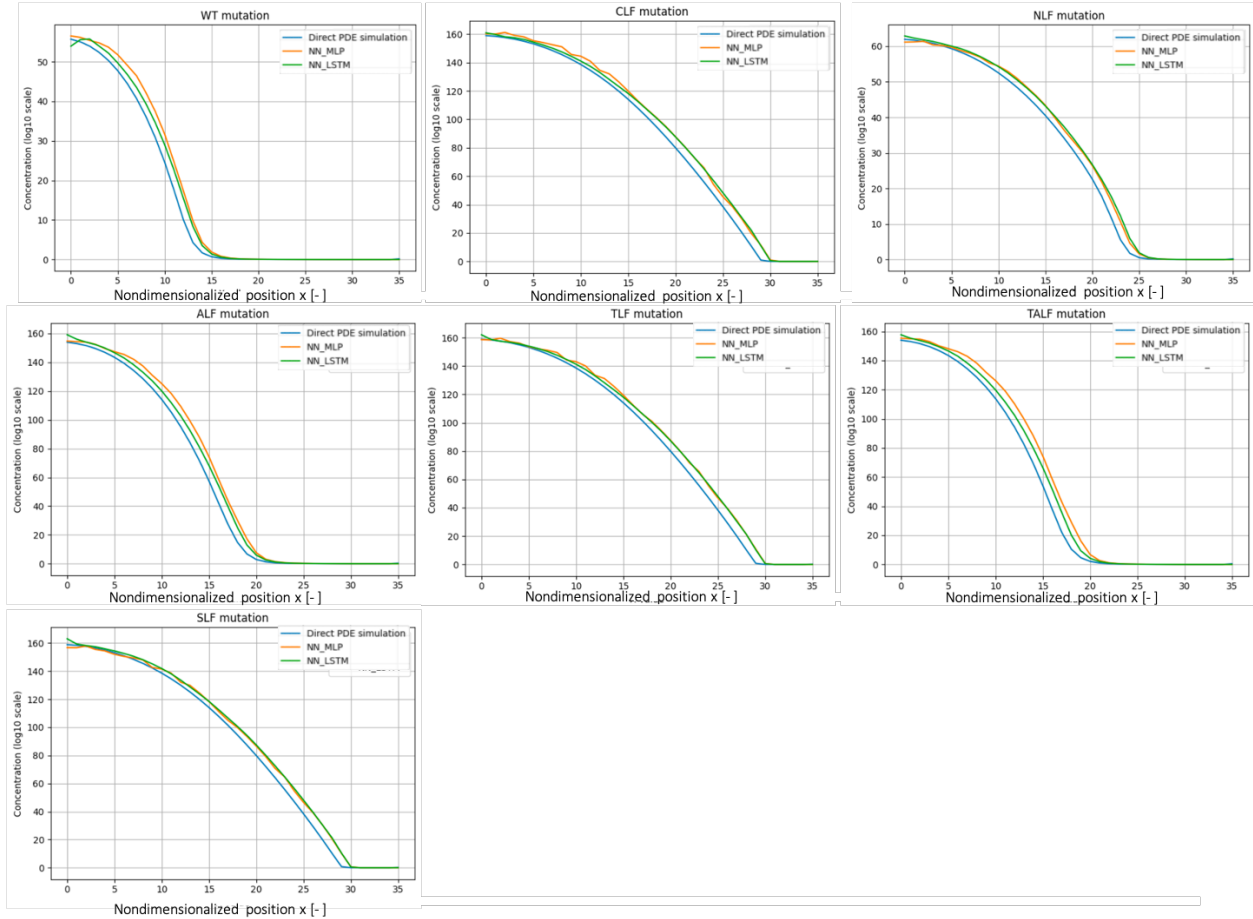


Figure 4.4 Comparison of protein distributions obtained by direct PDE simulation, MLP metamodel and LSTM metamodel plotted over the 1D domain parameterized by the nondimensional x coordinate, with $x = 0$ (0 micrometer) the ventral end and $x = 35$ (700 micrometers) the dorsal end on margin.

Figures 4.4 shows how MLP, and LSTM model respectively reproduce the PDE simulations results on seven randomly chosen samples, one for each mutation. We can see that generally the neural networks provide a final BMP distribution that is very similar to the one given by a direct PDE simulation. Since LSTM gives outputs in the form of a sequence, one by one, we would expect that its plots would generally be smoother than those of MLP.

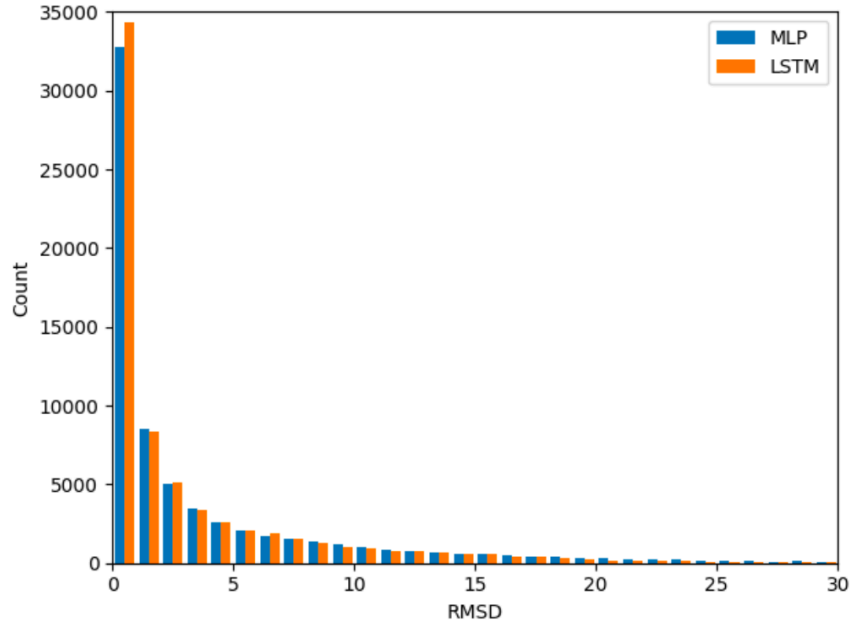


Figure 4.5 Comparison of RMSD distribution among 70,000 validation MLP metamodel and LSTM metamodel

Both quantitative and qualitative evaluations slightly favor the LSTM model. It gives higher R^2 , lower relative error, produces smoother BMP distributions and reproduces the mutation data with less variation. The RMSD between simulation results and metamodel results was calculated, and Figure 4.5 shows the histogram of the case number of RMSD distribution for both the MLP and LSTM metamodel. Predicted results of only a slight improvement over the MLP. However, those improvements come at a significantly higher computational cost of at least 20x. Since we would like to use the neural network metamodel for rapid exploration of PDE parameter space, the MLP may often be the better choice.

We further applied the neural network approach to a more complex PDE system that contains 3D dynamics on the surface of a hemisphere geometry. Previous simulations of a growing domain 3D simulation were used as the training and validation data in the MLP model (Li et al. 2020). To handle the large input and output data size in the prediction of the results for the entire embryo (over 1000 spatial locations in 3D compared to 36 spatial points in 1D), adjustments to the structure of the neural network were needed resulting in a more complicated model with multiple layers and output points that increased the CPU latency and decreases the accuracy of the model prediction relative to the 1D simulation. To train the neural networks to solve supervised

learning tasks as an alternative to the PDE solver, we used the input data with the structure as [parameters + coordinates + time] and the output data structure as [concentrations of different species], which is similar to the inputs and outputs of a PDE solver. To train the neural network for the 3D hemisphere, the MLP model was given the individual calculation points extracted from the grid (see Figure 4.6). Ten thousand WT simulation results were used to test the model, provide 4,051,234 points for the training set (9000 whole embryo simulation results) and 450,000 (1000 whole embryo simulation results) points are used for the validation set. Train accuracy remains 99% after 100 epochs. Figure 4.6 shows the comparison of multi-objective plots between simulation and NN model of 3D growing domain model results with the MLP network.

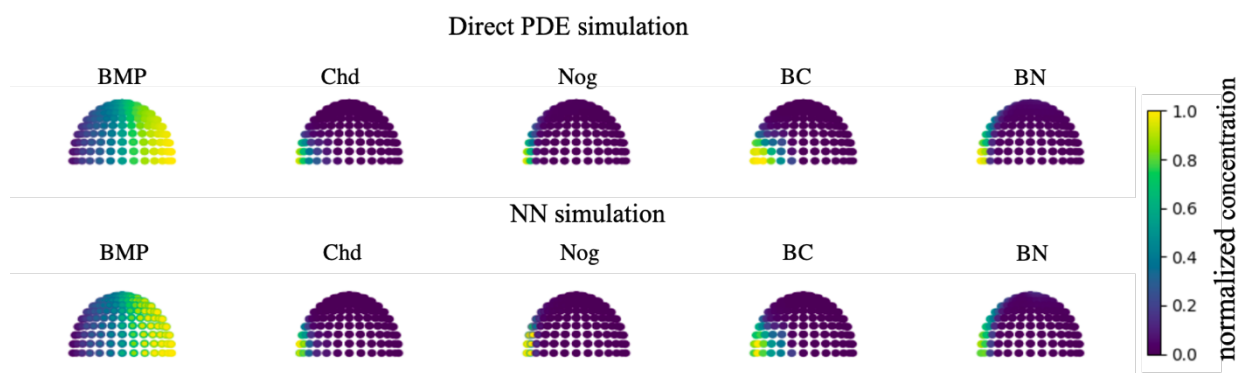


Figure 4.6 Comparison between simulation and NN model of 3D growing domain model results with MLP model

In this review, we summarize and show an example for how neural network metamodels are effective in accelerating PDE-based biological simulations. The acceleration offers speedups of about 1000x while preserving accuracy with R^2 above 0.99. We considered a specific PDE model from zebrafish development, but the neural network models discussed here can be applied to many other PDE systems. Compared to [152] we train both LSTM and MLP models and show that MLP offers advantages in speed without sacrificing much accuracy.

The key contribution in the approach presented is the acceleration of PDE evaluation via NN metamodel, which enables the inverse problem of identifying the parameters of the PDE that best explain experimental data. With the proposed NN metamodel, we can now replace the direct PDE solver and explore the entire input space thanks to the computational efficiency of the NN metamodel. However, brute force parameter exploration may not be the most efficient approach, even with a fast metamodel. Another advantage of NN is that they are fully differentiable and thus

open the possibility for gradient descent which would be much more complicated when the direct PDE solver is used. For direct PDE solvers, gradient optimization entails either costly and inaccurate numerical approximations based on more function evaluations, or solution of the adjoint problem. Finally, NN and other machine learning methods could also contribute to the inverse problem by employing reinforcement learning (RL) to find optimal parameters. The actions from RL could be the parameters searched and reward could be the inverse of error between PDE simulation or NN metamodel and experiments. In a similar fashion, reinforcement learning has already been used in Neural Architecture Search (NAS) [161]. Another application that can expand the use of the NN model-based acceleration of PDE is multi-objective optimization. Multi-objective optimization is an area of multiple criteria decisions making that is concerned with mathematical optimization problems involving more than one objective function to be optimized simultaneously. It is a useful tool for quantitative biology (Pargett et al. 2014). However, it may require a large number of parameter screens among the different types of simulation. We expect that the approaches discussed here will improve the capabilities of AI-based surrogate models and accelerate scientific research and discovery in biology.

5 FINITE ELEMENT GROWING DOMAIN MODEL OF BMP-MEDIATED SIGNALING IN ZEBRAFISH EMBRYO

We are interested in how the cellular movements impact the formation of gradients by contributing an advective term whereby the morphogens are swept with the moving cells as they move vegetally. Our goal in this chapter is to develop a complete advection-diffusion-reaction model that incorporates all stages of zebrafish embryonic development data to investigate mechanisms in underlying BMP-driven DV patterning during epiboly. The finite difference approach described in Chapter 3 has limits in reflexing the advection due to the cell movement during epiboly and the mass conservation.

5.1 Methods

In this chapter, we propose an improved model with the finite element method to solve the coupled advection-diffusion-reaction equations in a smoother growth domain fashion. Figure 5.1 gives an overall flow of how we construct the FEM model and incorporate it with the experimental data. Compare to the previous finite difference approach, the couple PDE system would be solved by mass-conservative growing mesh finite element scheme. The experimental data collected and analyzed in Chapter 2 were applied to this approach. Dynamic cell imaging data are used to quantify the cell movement during the epiboly, and the velocity map described in chapter 2.1 will be applied in the finite element model as the guide of mesh movement. We evaluated the accuracy of the mesh updating compared to the cell movement driven advection and its role in embryonic patterning. Quantitative whole-mount RNA scope data of BMP2b and phosphorylated-SMAD data are collected and analyzed precisely to test the hypotheses of the gradient formation mechanism in our model. By combining the biophysics of epiboly with the regulatory dynamics of the BMP network, we can test complex models to investigate the consistent spatiotemporal DV patterning in the early zebrafish embryo.

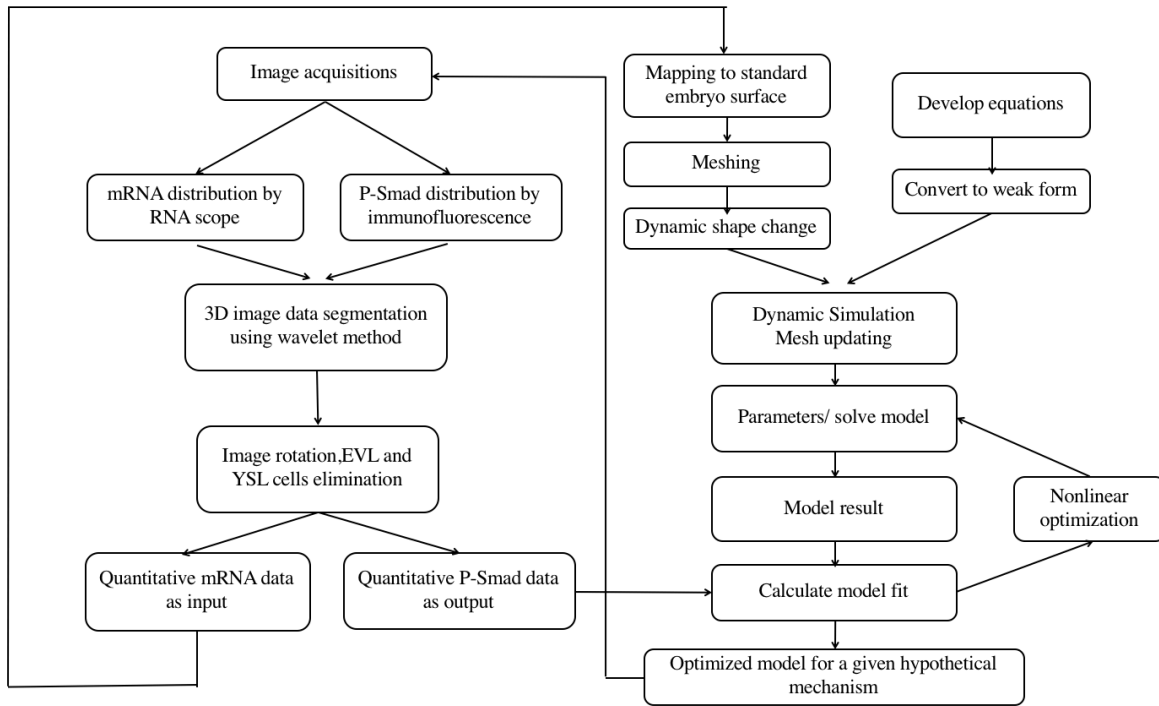
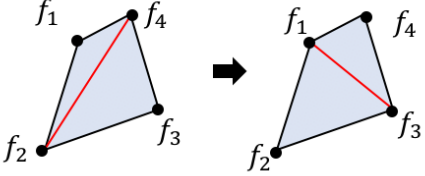
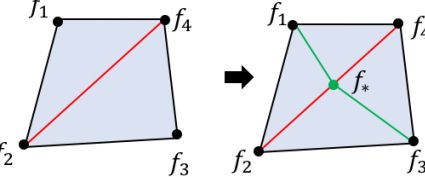
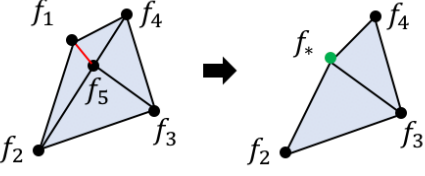


Figure 5.1. Flow chart of FEM model construction

5.1.1 Remeshing scheme

To keep the quality of the mesh during the large deformation, we adopt a previous study on the mesh tangling problem in surface tracking [162], the powerful C++ library tracks dynamic surfaces with triangle meshes in 3D. Triangles with small areas or poor aspect ratios can adversely affect collision detection, topological operations, and any boundary-integral-based simulation [162]. Simple common operations like edge flip, edge split, and edge collapse, etc. are used to improve the quality of the surface discretization. Table 5.1 shows the detail of the remeshing method used in this study. This powerful remeshing library can provide an environment that our simulating embryo surface meshes remain their quality during epiboly.

Table 5.1. Remeshing scheme

Edge flip		f_i are nodal values of some function f f_i do not change with edge flips
Edge split		New nodal value $f_* = \frac{1}{2}(f_2 + f_4)$
Edge collapse		New nodal value $f_* = \frac{1}{2}(f_1 + f_3)$

5.1.2 FEM formula for convection-diffusion-reaction system

Arbitrary Lagrangian-Eulerian (ALE) methods is a method that allows the mesh to move arbitrarily, with the two limiting cases reducing to the Lagrangian and Eulerian formulations. In the Eulerian-based finite element formulation, the computational system is fixed in space, on the other hand, in the Lagrangian-based finite element formulation, the computational system is attached to the material. An ALE mesh that conforms to the Lagrangian mesh for the structure along part of its boundary while the rest remains fixed providing a convenient transition between the fluid and the structure [163], [164].

Here we discuss the FEM solution for the diffusion-reaction system problem on the fixed mesh at each single time interval. In the case of the advection-diffusion-reaction system problem we consider an ALE formulation

$$\left. \frac{\partial \phi}{\partial t} \right|_x + (\mathbf{u} - \hat{\mathbf{u}}) \cdot \nabla \phi - \nabla \cdot k \nabla \phi - f = 0$$

Where

ϕ is a scalar field denoting the concentration of certain species

\hat{x} are the coordinates of the reference mesh (the mesh at time t)
 \mathbf{u} is the velocity of the fluid
 \hat{u} is the velocity of the mesh
 k is the diffusion coefficient
 f is the source term (include all the expression term and reactions term)

We applied the cell velocity map to guide the mesh update in every single time increment. By assuming that the cell flow in which ϕ is transported moves with the mesh, thus, we can make the approximation that the velocity of the fluid \mathbf{u} is equal to the velocity of the mesh movement, which canceled the advection term in the equation. In other words, the mesh movement can be considered to represents the advection in the system.

Then, we have the general for of reaction- diffusion system with,

$$\left. \frac{\partial \phi}{\partial t} \right|_{\hat{x}} - \nabla \cdot k \nabla \phi - f = 0$$

5.1.3 Finite element approximation

For the finite element approximation of the diffusion-reaction system, considering a time-dependent diffusion of a single species with concentration C_i

$$\dot{C}_i + \nabla \cdot q_i = s_i(C_i)$$

$$\frac{C_i^t - C_i}{\Delta t} + \nabla \cdot q_i = s_i(C_i)$$

where

$$q_i = -D_i \nabla C_i$$

D_i is the diffusion rate of the specific species.

Multiplying the differential equation by a test function w and integrating over the domain gives the weak formulation of the problem is:

$$\int \left(\frac{C_i^t}{\Delta t} \right) w - \int \left(\frac{C_i}{\Delta t} \right) w - \int s_i w - \int \nabla w \cdot q_i + \int w \cdot q_n = 0$$

Thus, the residue is

$$RES = \int \left(\frac{C_i^t - C_i}{\Delta t} - s_i \right) w - \int \nabla w \cdot q_i + \int w \cdot q_n = 0$$

To compute surface derivatives on a triangulated surface, we need to define a map which converting the symmetric weak form equation from the global Cartesian coordinates to natural coordinates system. To define a map $M: (\xi, \eta) \rightarrow (x, y, z)$ from a reference triangle in the local coordinate system (ξ, η) to T_m in the physical coordinate system (x, y, z) we define the surface point $\mathbf{x}_\Gamma = \mathbf{x}_\Gamma(\xi, \eta)$.

$$\bar{\phi} = \bar{X} = \sum N_i(\xi, \eta) \bar{X}_i$$

where \mathbf{x}_i is one of the n nodal points of the triangle T_m of the surface, and $N_i(\xi, \eta)$ is the finite element shape functions of order m on the reference element.

$$N_1 = 1 - \xi - \eta$$

$$N_2 = \xi$$

$$N_3 = \eta$$

Shown in Figure 5.2, \bar{g}_1 and \bar{g}_2 are two tangent vectors of the surface

$$\frac{\partial \bar{\phi}}{\partial \xi} = \frac{\partial \bar{X}}{\partial \xi} = \sum \frac{\partial N_i}{\partial \xi} \bar{X}_i = g_1$$

$$\frac{\partial \bar{\phi}}{\partial \eta} = \frac{\partial \bar{X}}{\partial \eta} = \sum \frac{\partial N_i}{\partial \eta} \bar{X}_i = g_2$$

\bar{e}_1 is the unit vector of \bar{g}_1

$$\bar{e}_1 = \frac{\bar{g}_1}{|\bar{g}_1|}$$

\bar{n} is the orthonormal vector of the surface

$$\bar{n} = \frac{\bar{g}_1 \times \bar{g}_2}{|\bar{g}_1 \times \bar{g}_2|}$$

\bar{e}_2 is the basis vector orthonormal to \bar{e}_1 and \bar{n}

$$\bar{e}_2 = \bar{n} \times \bar{e}_1$$

\bar{e}_1 , \bar{e}_2 , and \bar{n} are the orthonormal unit basis for the surface. Then the transformation matrix between Cartesian coordinates to natural coordinates is:

$$A = [e_1, e_2, n]$$

Thus, the mapped coordinate of the mesh is

$$\hat{X} = A^{-1} * \bar{x}$$

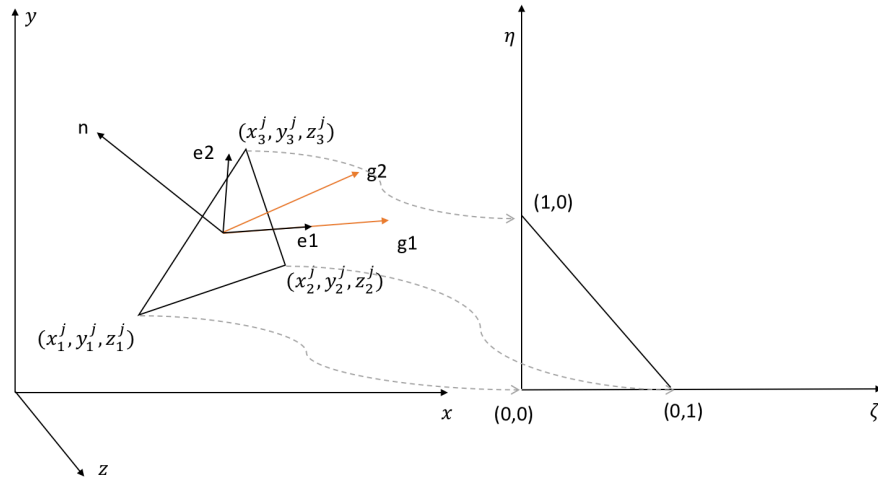


Figure 5.2. Surface mapping

The diffusion and reaction system are solved on a fixed domain in a specific time increment, and the Newton-Raphson method is applied to finding the exact solution for the particular time interval. After solving the reaction-diffusion system in a single time increment, the cell velocity will be applied to calculate the nodal movements, the remeshing processes will be applied if the mesh quality is low. At the case of a new node was generated, the concentration of the node will be interpolated through the other close nodes.

5.1.4 Governing equations

The improved model is solved by finite element formulation in the moving domain. Coupled continuous partial differential equations (PDEs) include transport by diffusion and advection, chemical reactions between secreted components, and cellular feedback, in the form of non-linear Hill-like functions for cooperative repression activation of feedback targets. While our

previous mathematical model described in chapter 3.1, used a simple linear proteolysis model of Chordin by Tolloid alone, to simulate the feedback mechanism for sizzled at gastrula stage, we updated the model to explicitly simulate the enzyme saturation kinetics to model Chordin proteolysis by Tolloid and the distinct competitive inhibition of Tolloid by Sizzled. The governing equation solved through blastula to gastrula stage list below:

$$\frac{\partial B}{\partial t} = \nabla \cdot D_B \nabla B + u \cdot \nabla B + \phi_B - k_1 B \cdot C + k_{-1} BC - k_2 B \cdot N + k_{-2} BN + \lambda_1 \cdot \frac{1}{1 + \frac{S}{kit} + \frac{BC+C}{kmt}} \cdot Tld \cdot BC - k_b B$$

$$\frac{\partial C}{\partial t} = \nabla \cdot D_C \nabla C + u \cdot \nabla C + \phi_C - k_1 B \cdot C + k_{-1} BC - \lambda_2 \cdot \frac{1}{1 + \frac{S}{kit} + \frac{BC+C}{kmt}} \cdot Tld \cdot C - k_c C$$

$$\frac{\partial N}{\partial t} = \nabla \cdot D_N \nabla N + u \cdot \nabla N + \phi_N - k_2 B \cdot N + k_{-2} BN - k_n N$$

$$\frac{\partial BC}{\partial t} = \nabla \cdot D_{BC} \nabla BC + u \cdot \nabla BC + k_1 B \cdot C - k_{-1} BC - \lambda_1 \cdot \frac{1}{1 + \frac{S}{kit} + \frac{BC+C}{kmt}} \cdot Tld \cdot BC - k_{BC} BC$$

$$\frac{\partial BN}{\partial t} = \nabla \cdot D_{BN} \nabla BN + u \cdot \nabla BN + k_2 B \cdot N - k_{-2} BN - k_{BN} BN$$

$$\frac{\partial S}{\partial t} = \nabla \cdot D_S \nabla S + u \cdot \nabla S + \frac{V_s \cdot B^n}{k^n + B^n} - k_s S$$

$$\frac{\partial Tld}{\partial t} = \nabla \cdot D_{Tld} \nabla Tld + u \cdot \nabla Tld + \phi_{Tld} - k_{Tld} Tld$$

Similar to the denotations used in Chapter 3.1. BMP ligand, Chordin, Noggin, and Sizzled are denoted by B, C, N, and S, and the complexes of BMP-Chordin and BMP-Noggin are denoted by BC and BN, respectively. Since Sizzled expression is induced by BMP signaling [50], we applied Sizzled expression to the model based on BMP signaling levels represent as then gene control feedback term which described by the Hill equation $\frac{V_s \cdot B^n}{(K/B_0)^n + B^n}$, V_s is the maximum of Sizzled expression, B_0 is the maximum of BMP. In order to estimate the parameter for the feedback term (k, kit, and kit), in the parameter screen, we have to run each parameter case with Chd mutant and Chd/Szl mutant priory to the WT case to get the maximum BMP level. To determine the fixed values of V_s and n , Tuazon et al measured the distribution of sizzled mRNA and compared it directly to the stage-matched distribution of P-Smad5 [51]. We applied V_s as 100 and n as 4 based on their calculation.

5.1.5 Model validation

We have tested our code for the diffusion-reaction solving method and compared it with the commercial FEM package COMSOL for validation.

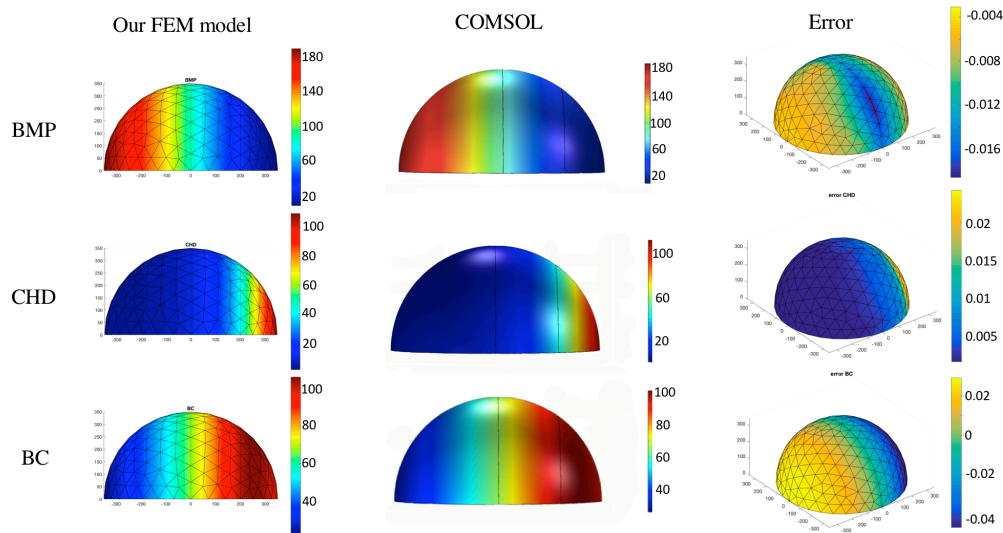


Figure 5.3. FEM model validation with COMSOL

To verify the reliability of the finite element model, we tested the same model in COMSOL under the same condition. Since COMSOL is not able to solve our problem in growth domain condition, the growth rate in our FEM model was set as 0 to represent the same fixed domain with COMSOL. The same mesh was applied in both models, the concentration result in every single node was compared to calculate the error between our model and COMSOL. The average differences between the two models were less than 5%. Thus, we consider our algorithm for the finite element scheme in calculating the diffusion-reaction PDES is trustworthy.

5.2 Result

BMP signaling regulation in zebrafish embryos is a complex network. The main goal of the study is the characterization of numerous extracellular modulators and intracellular feedback regulators function in establishing and controlling BMP signaling along the dorsal-ventral (DV) embryonic axis in vertebrates to convince space and time-dependent patterns of gene expression. We represent the biophysical driven finite element model can be a start point in testing the different

mechanisms in the regulatory network. In this current study, we validate our model against wild type P-Smad data, besides that we want to answer two important questions that remain in the study of BMP mediate DV patterning during epiboly, first, how the cell flow driven advection plays the role of BMP gradient formation? and second, if Sizzled plays a key role in size-dependent scaling invariance in zebrafish embryos?

5.2.1 Wild type parameter screening

Figure 5.4 illustrates the output of concentration profiles for different species simulated with the 3D FEM growing domain model. An initial geometry of triangle meshes represents the hemispherical cap of the zebrafish embryo at 3.5 hpf and the mesh evolves as the embryo shape changes during epiboly. Domain growth reflects the cell migration during epiboly. As the edges of the growing membrane move down the yolk, the mesh is continuously updated to maintain a high-quality discretization. Firstly, we did parameter screening for the wild-type embryo model. The parameter ranges keep consistent with the ranges list in Table 3.1.

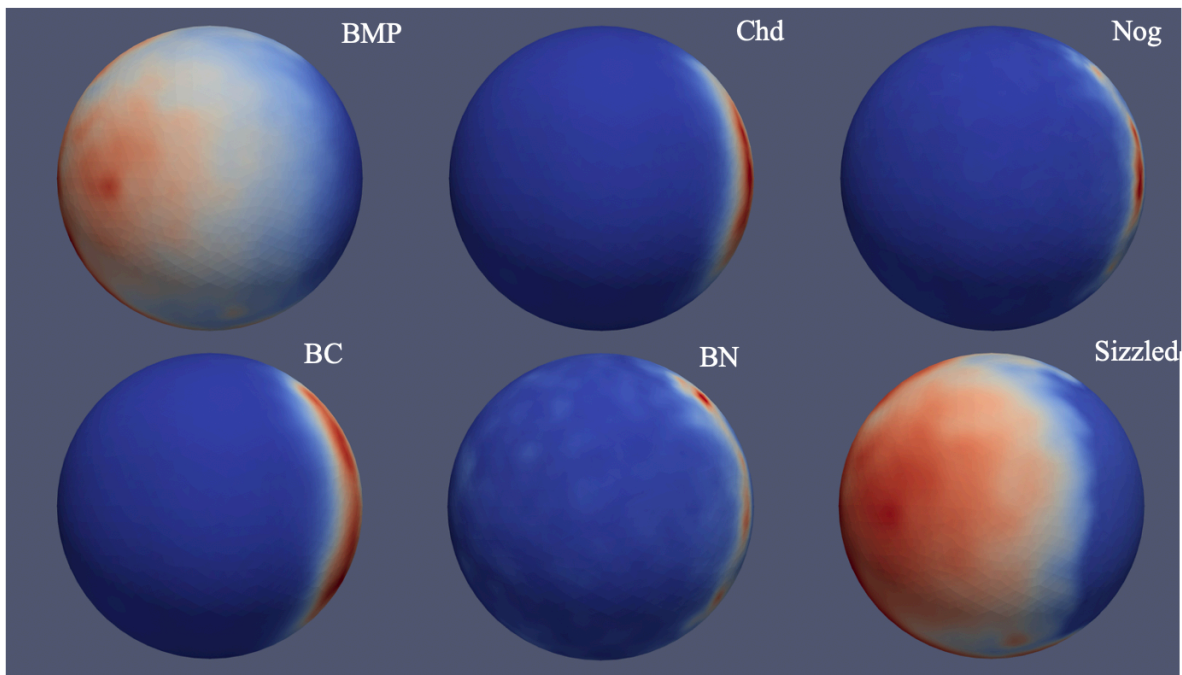


Figure 5.4. Finite elements simulation results in reflex of expression region obtain from mRNA expression map, concentrations for different species (BMP, Chd, BC, Nog, BC complex, BN complex and Sizzled) normalized individually.

With governing equations described in Chapter 5.1.4, we have a total of 21 unknown parameters with a large parameter range. On the other hand, the 3D models are computationally intensive, depends on the size of time increment, a single simulation can last from 4 min to hours. Adaptive time step is applied to accelerate the simulation. We also applied Latin Hypercube Sampling (LHS) scheme to evenly sample the parametric space. LHS samples only one sample in each row and each column in a square grid containing sample positions represents a Latin square. LHS generalized samples the parametric space with a given number of samplers in an arbitrary number of dimensions, whereby each sample is the only one in each axis-aligned hyperplane containing it. This can ensure that relatively smaller sampling parameter sets can represent the variability of the parametric space. A total of 5000+ parameter sets have been tested with the power of the supercomputer clusters at Purdue University.

Quantitative data with P-Smad image data that we analyzed in Chapter 2.2 contains specific information of BMP signaling in space and time. The P-Smad data at 4.7, 5.3, 5.7,6.3 and 6.7hpf applied as a scaler for the data-model comparisons against the wild-type signaling profiles. Figure 5.5 demonstrates a simulation result for a WT case at different time points. The simulated BMP concentration level and measured P-Smad5 profiles are normalized between 0 and 1 to calculate the relative error between each profile for the entire domain. For direct comparison, BMP simulation results were interpolated on evenly distributed simply point consisted of experimental P-Smad results, normalized root mean squared deviation (NRMSD) was calculated pointwise to measure the difference. Contrary to expectations, we were not been able to find a best-fitted parameter along with all the sample points over the spatiotemporally. As shown in Figure 5.5C, we found that many cases of the simulation results show good fits on the marginal region and have a consistent maximum BMP level against the P-Smad5 profile at all the testing stages. However, the larger errors happen in the ventral-animal region for the majority of the simulation results.

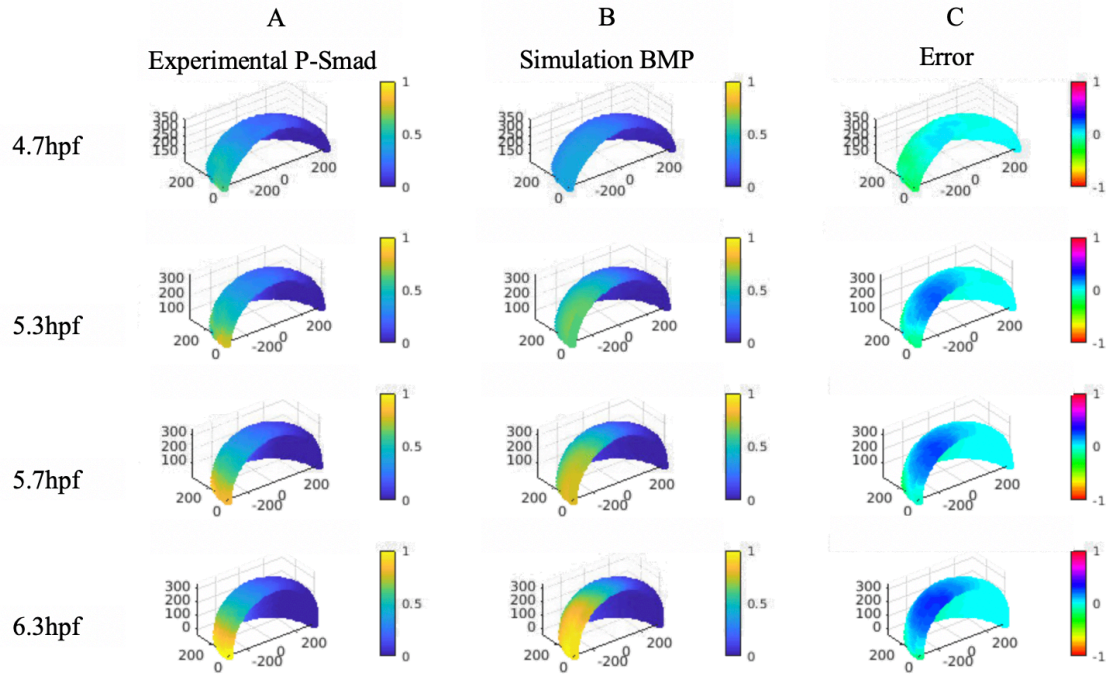


Figure 5.5. Column A, Averaged and normalized P-Smad5 profile at 4.7 hpf, 5.3 hpf, and 5.7 hpf and 6.3 hpf. Column B, Normalized simulation result of a wild type case 4.7 hpf, 5.3 hpf, and 5.7 hpf and 6.3 hpf. Column C, Relative differences between simulation results and P-Smad5 level. Positive error indicates the experimental data are higher than simulation results, negative error indicates the experimental data are lower than simulation results.

To analyze the possible pitfalls in our system, we found that the BMP profile on the ventral-animal region highly sensitive to the BMP expression level between the marginal region and ventral-animal region. The limitation of the imaging acquisition for collecting the whole-mount *in situ* hybridization mRNA data could be the reason. As shown in Figure 2.14, for the early development stage through 5.7hpf, the BMP mRNA expression map show a relatively higher level of expression on the marginal region than the ventral-animal region. However, at 6.3hpf the expression level shows a huge drop off at the marginal region. By examining the original confocal image, we found some limitations of the image acquisition, first, the signal level drop-off as the z-stack goes deep, second, the signal lost mainly occurs at the region that embryo shape perpendicular to the imaging plane where the laser light needs to pass a thicker tissue, third, the BMP mRNA signal is relatively weak compares to Chd mRNA signal. By reimaging the samples from different angles of view, we found that the marginal region should have a relatively higher expression level of BMP compare to the ventral-animal region.

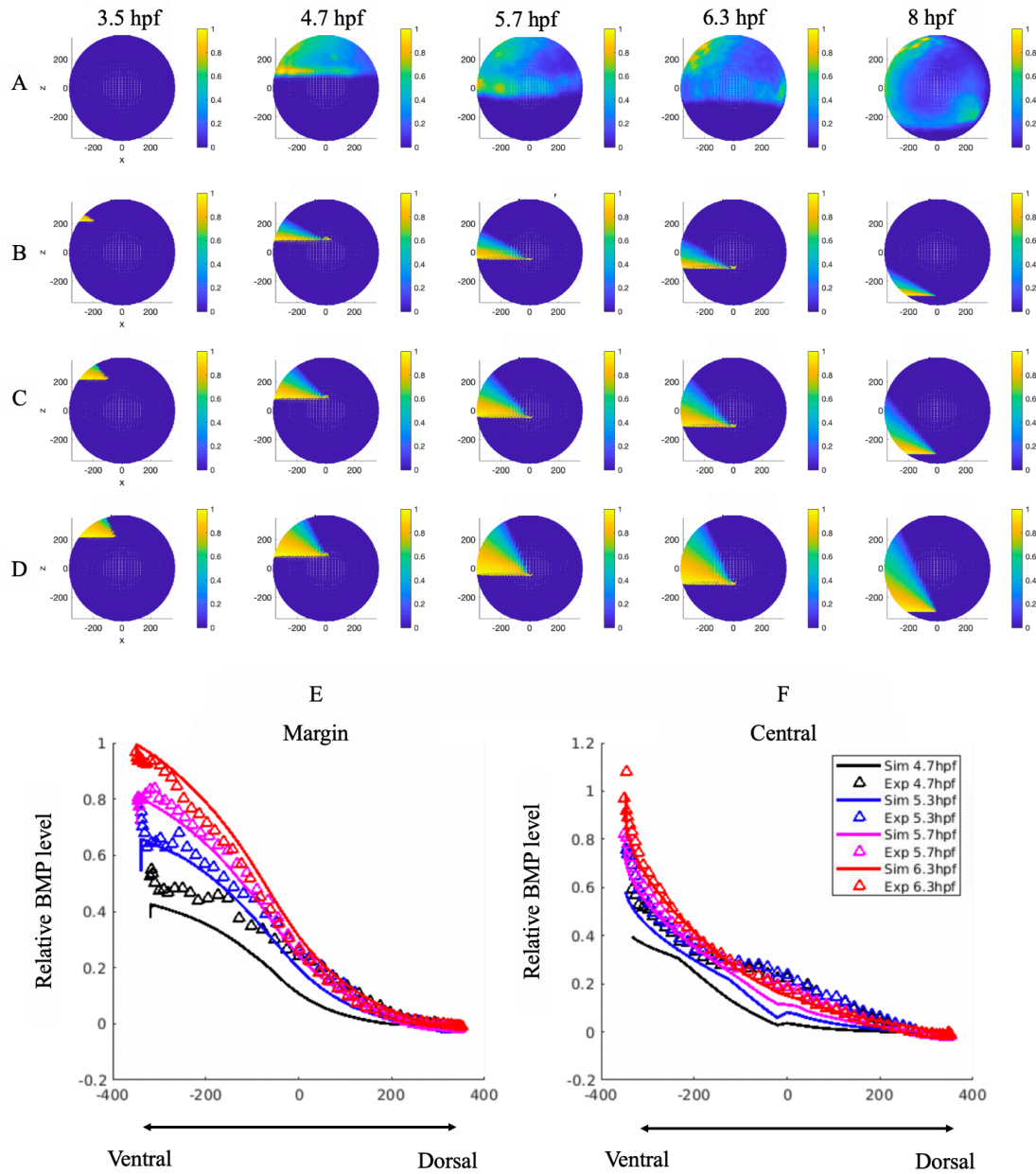


Figure 5.6. Test of expression regions for finding the possible expression patterning induces the best-fitting simulation result on 3.5,4.7,5.7,6.3, and 8 hpf. A. Original BMP expression map obtained from the imaging of RNAscope experiment, B-D, the example of three different testing BMP expression map. E. Best-fitted result on marginal region, F, Best fitting result on the central region. Smooth lines represent the FEM simulation results interpolate on the experimental data location, triangle indicated the averaged and normalized P-Smad5 level.

We try to test the possible BMP expression profiles that can lead to a better-fitted result against the P-Smad 5 profile. We run a parameter screening over 182 sets of parameters represent

the best-fitting results in our previous 1D model [51] over seven different map of BMP expression which we consider may reflex the real expression pattern. Figure 5.6 B-D illustrated three examples of the test regions on 3.5,4.7,5.7,6.3, and 8 hpf. We found that the region shown in Figure 5.6 D gives the smallest NRMSD for majority the parameter set we screened. Shown in Figure 5.6 E-F, the normalized BMP profile on both of marginal region and central region against the P-Smad5 profile in the best-fitted case. We are developing new experimental approaches to validate this hypothesis.

5.2.2 Domain change and advection play a role in BMP gradient formation

During epiboly, the regions of the embryo where BMP is patterning are rapidly changing as the cells stream and converge during gastrulation. In addition to the diffusion of the ligand, advection may be a potential source of the gradient shaping dynamics. Besides the questions that remain with the mechanism of the extracellular regulation network, another question is how the advection's role in BMP gradient formation. For testing the contribution of advective transport during epiboly, we exam our model over two types of mesh schemes under the same simulation setting, the growing domain mesh with advection, and the fixed domain mesh (8 hpf) without advection. As shown in Figure 5.7, as the input expression profiles and the parameters in the governing equations remain the same, both the growing-domain advection model and the fixed-domain diffusion only model, reaches the same max level of BMP concentration by the end of the simulation at 8hpf, the total mass conservative in the system. However, the BMP gradient over the domain has an obvious different profile between these two scenarios. Compare Figure 5.7 B, Figure 5.7 A has a clear wider range of BMP concentration, this should contribute by both the domain growth and the active transport in the horizontal direction. Figure 5.7 C and D demonstrated a detailed comparison of margin and central profile though 4.7 hpf to 6.3 hpf. Notably, the BMP on margin level is much lower for the fixed-domain case than the grown domain case while the central profile remains slightly lower but not as lower as the margin profile. This should cause by the relatively larger domain for the fixed-domain case at the beginning of the simulation. The same amount of the BMP ligand could diffuse further with a larger domain. Thus, the domain change and the advection that reflex the epiboly and cell flow in the early development contributed to the formation of BMP concentration gradient, the effectiveness should not be ignored when modeling the BMP meditate patterning in the zebrafish embryo.

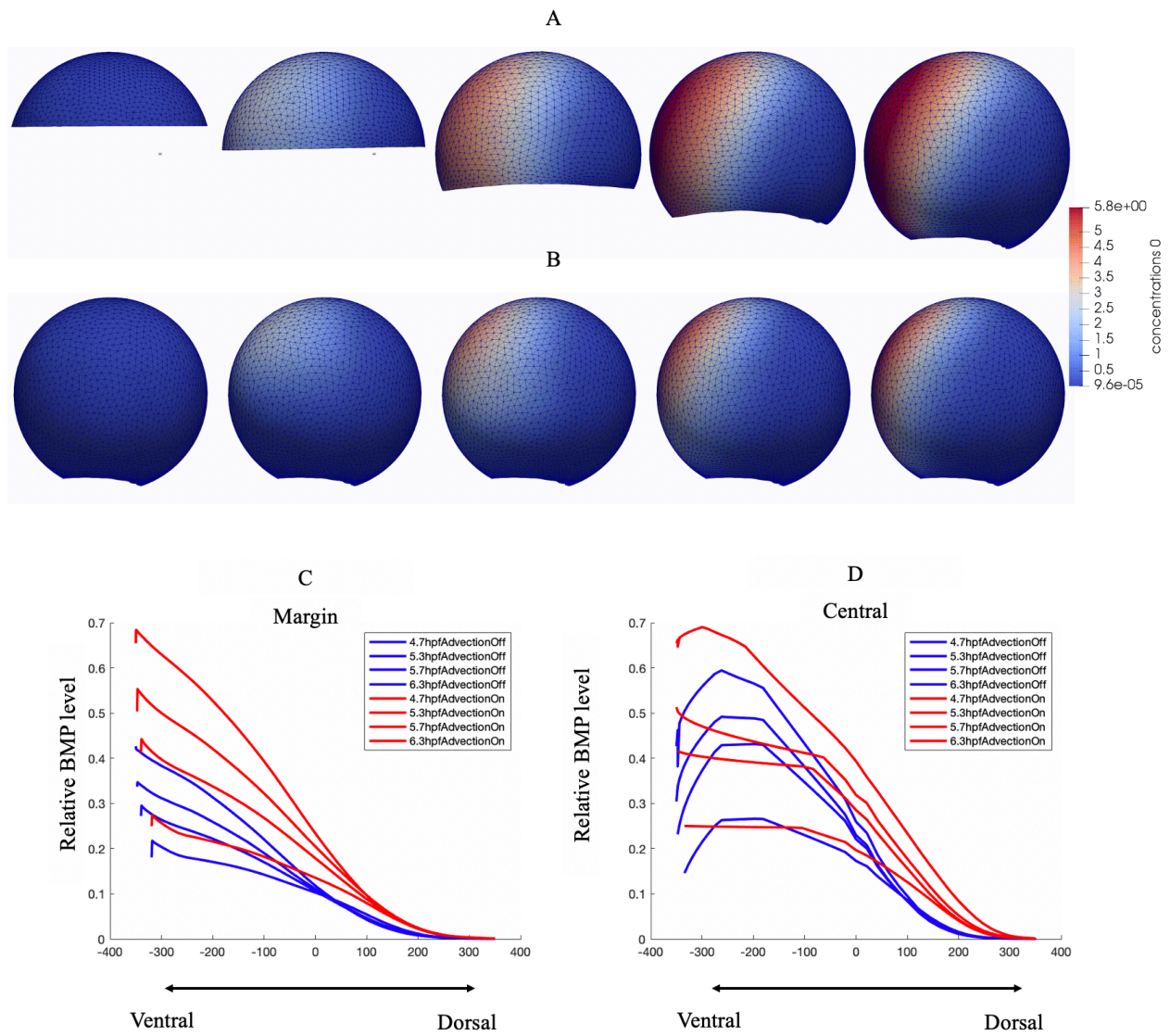


Figure 5.7. Comparison of growing domain advection model (A) vs fixed domain diffusion only model (B) of BMP concentration profile in 3D lateral view. Red lines represent the growing domain simulation result of BMP concentration on marginal region and central region, Blue lines represent the fixed domain diffusion only simulation result of BMP concentration on marginal region and central region, for 4.7,5.3,5.7,6.3 hpf.

5.2.3 Examination the scaling invariance in BMP gradients formation along dorsal-ventral axis

As discussed in Chapter 1.5, scaling invariance remains as a topic of intense debate in how feedback and scaling work undergoing embryo development. Obviously, without considering the real shape of the organism in its real-life size and scale realistically it will be difficult to examine this question effectively. Our current 3D growing domain model provides a framework for testing the BMP regulation network with multiple feedback mechanisms to decipher the underlying mechanism of interspecies and intraspecies scaling invariance. It has been reported through the experimental evidence that the zebrafish embryo maintains scaling of the BMP signaling gradient in embryo size of up to 30% [92]. Computational and experimental studies in *Xenopus* have determined that the mechanism of Sizzled-regulated Tolloid cleavage of Chordin is the key for BMP signaling scale invariance [50]. In this section, we will discuss our result in testing scaling invariance in the zebrafish embryo.

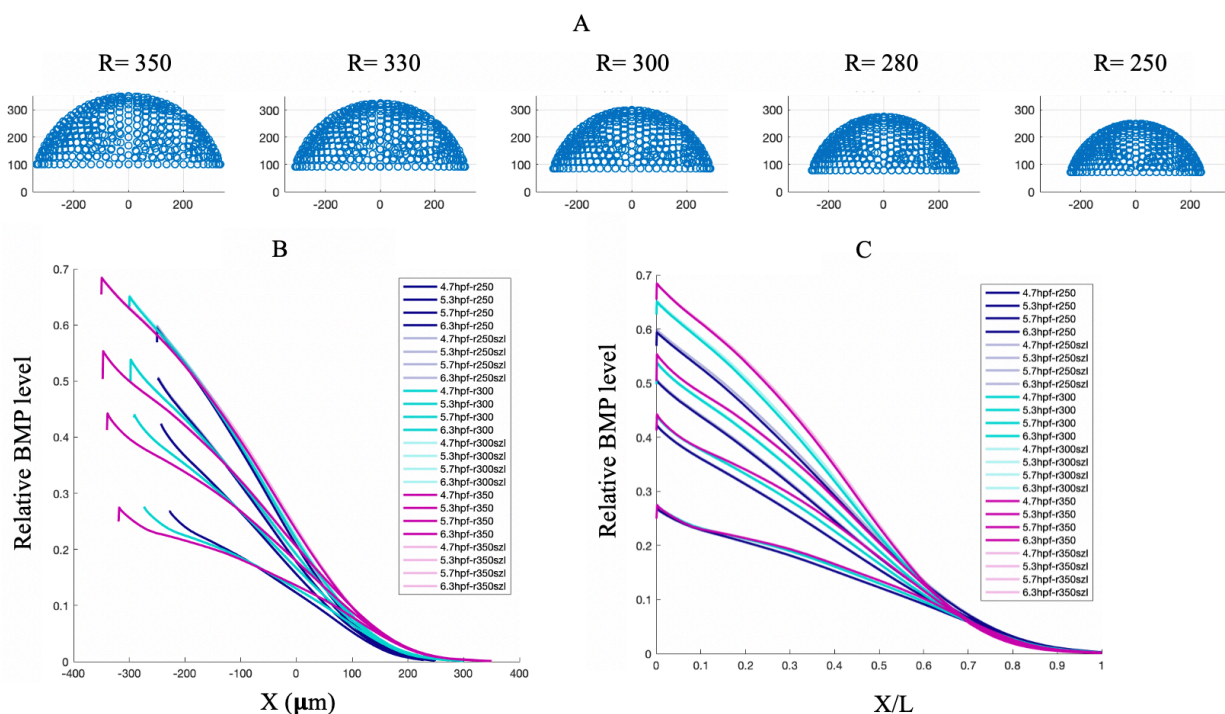


Figure 5.8 A. Comparison between embryo size in real scale. Points cloud indicates the FEM mesh nodes on the specific embryo size. B. Relative BMP gradient reflex in real embryo length C, Relative BMP gradient reflex in normalized embryo length. For clear plotting, only the results from embryos with the radius of 250 μm , 300 μm , and 350 μm were shown in the figure.

To test the Sizzled's role in scaling invariance, we simulated our current seven species model (Chapter 5.1.4) in different size embryos (in the radius of 250 μ m, 280 μ m, 300 μ m, 330 μ m, and 350 μ m) with a parameter screen over 500 parameter sets in each embryo size (Figure 5.8A). We screened the simulated BMP profiles of the embryo radius of 350 μ m (which we consider to be the normal size of the WT zebrafish) over the P-Smad5 profile. Figure 5.8 B and C illustrates the BMP morphogen gradient for the best-fitted result on Margin region at 4.7hpf, 5.3hpf, 5.7hpf, 6.3hpf for both WT and Szl mutant simulation on real embryo size (X plot) and normalized embryo size (X/L plot) for embryo radius in 250 μ m, 300 μ m, and 350 μ m. We found in the majority of our better-fitted simulation results, the BMP gradient shows no obvious differences between WT and Szl mutant. Instead, there is a clear gap between the profile for different size embryos, especially for the later stage embryos.

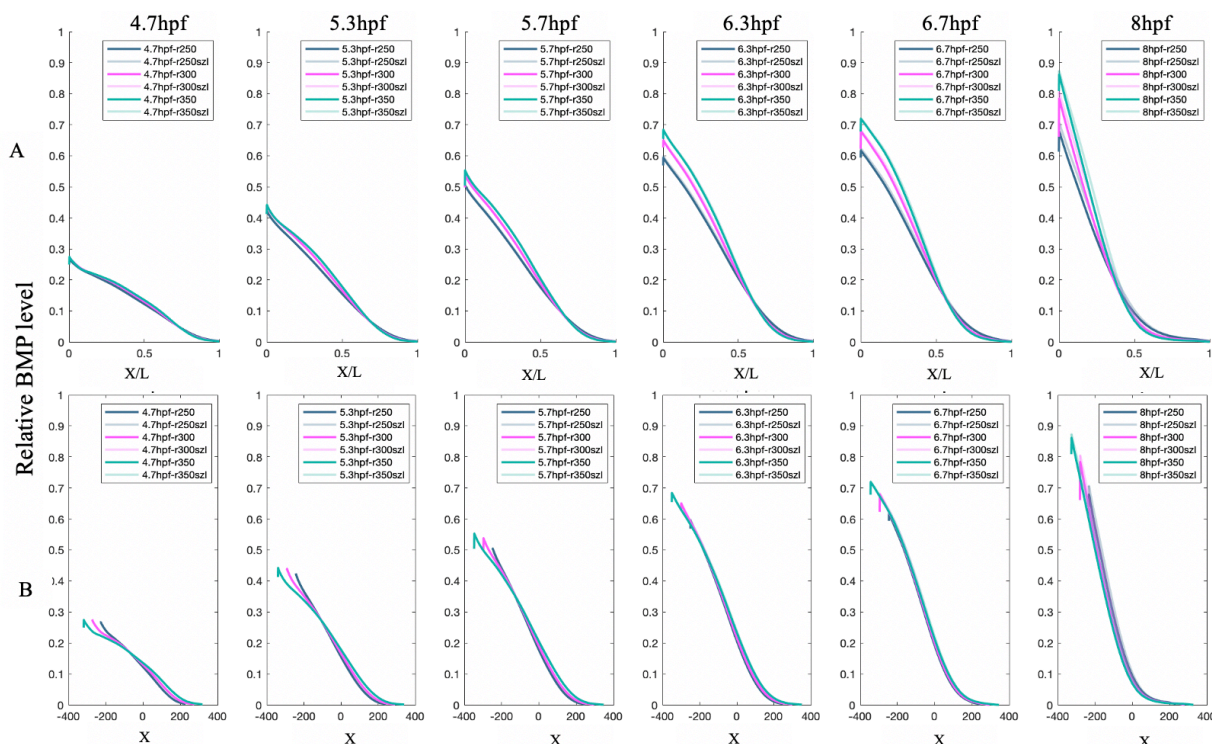


Figure 5.9 Relative BMP gradient for different size embryos at different development stage, 4.7hpf, 5.3hpf, 5.7hpf, 6.3hpf, 6.7hpf and 8hpf. A, Plot in normalized embryo length B, Plot in real embryo length.

For a better comparison, Figure 5.9 compares the BMP gradient for different size embryos at the different development stages. It is clear to see the BMP gradient in normalized embryo size

perfectly overlap with different size at 4.7 hpf but the gap between the profiles trend to get greater at later stages. It is also shown that compares to the earlier stage, there are slight differences between WT and Szl mutant profiles at 6.7hpf and 8hpf.

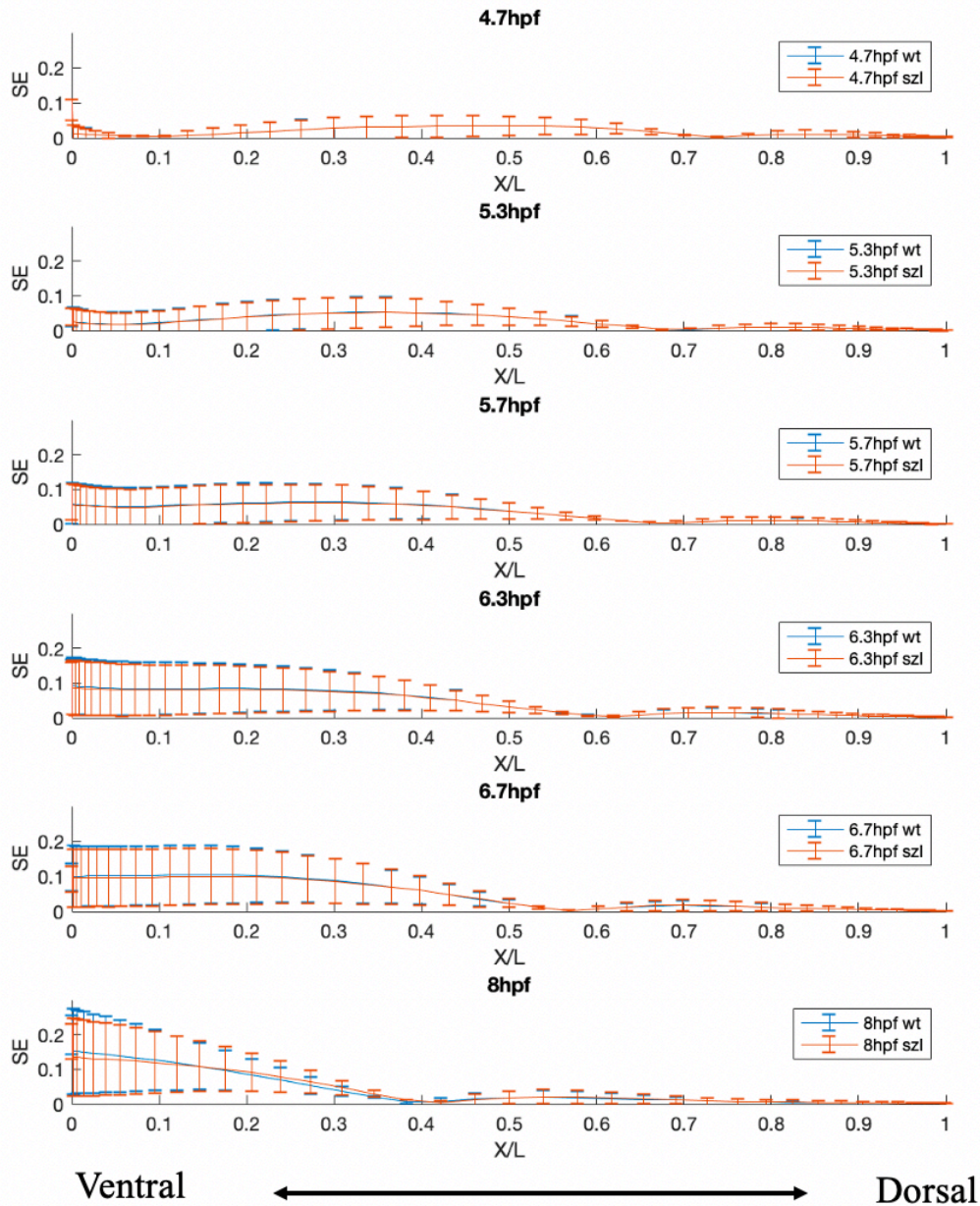


Figure 5.10 Pointwise Scaling Error (SE) at different development stages, 4.7hpf, 5.3hpf, 5.7hpf, 6.3hpf, 6.7hpf and 8hpf in WT and Szl mutant embryos results. Error bar indicates the maximum and minimum error over five different embryo sizes from 250 μm ~ 350 μm radius.

To further exam the scaling level in detail, we evaluated the pointwise scaling error over the different sizes of the embryos in both WT and Szl mutant results. Figure 5.10 shows the pointwise Scaling Error (SE) at different development stages, error bar indicates the maximum and minimum error over five different embryo sizes from 250 μm \sim 350 μm radius. The overall pointwise scaling error is less than 0.3 for all the tested embryo sizes in both WT and Szl mutant results (Figure 5.11). This SE level matching with our earlier experimental study in measuring the scaling invariance in early stage zebrafish embryos [92]. It is also observable that the SE is much smaller at the blastula stages (4.7hpf - 5.7hpf) compare to the gastrula stages (5.7hpf-8hpf). Nevertheless, there is no clear gap between the WT and Szl mutant results in the SE plot.

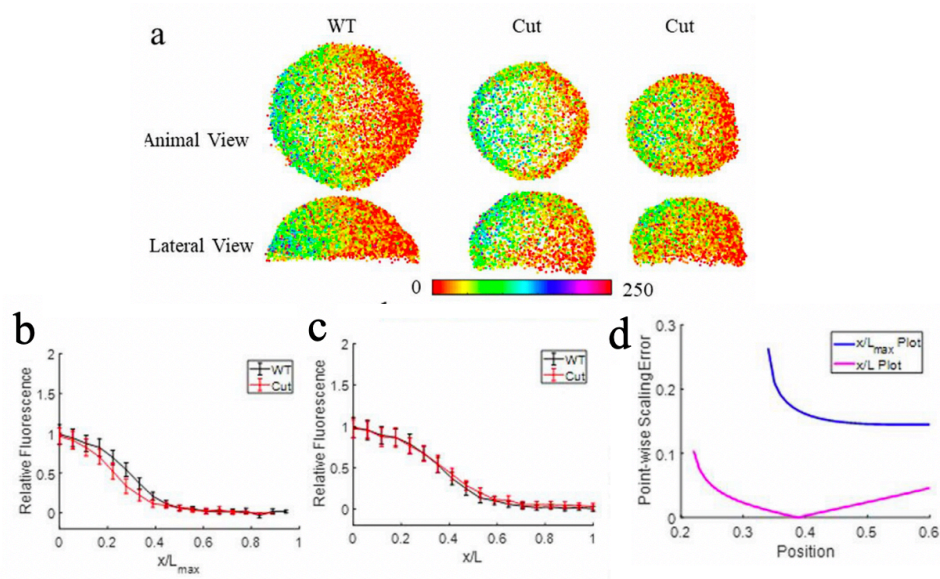


Figure 5.11 Experimental P-Smad5 gradient profiles of WT and Cut embryo scale. (a) The animal and lateral views of P-Smad5 stained 6 hpf embryo point clouds after image processing with P-Smad5 labeling intensity in color. (b-c) P-Smad5 gradient profiles of WT (black) and Cut (red) embryos after filtration, at x/L_{max} scale and x/L scale. Figure adapted from Huang (2019) [92]

5.2.4 Comparison of Finite difference approach and Finite Element approach

To visualize the simulation result changes in different conditions with mesh adding finite difference method, and advection driven domain change mesh conservative finite element method, we used our blastula stage model which is presented in Chapter 3 to test our FEM method, and Figure 5.12 is our result in checking the FEM code by utilizing the blastula stage model. Compare

to the finite difference model, by assuming that the shell membrane domain is getting thinner with growth, without adding the mass to the system, the FEM model keeps the mass conservative during the whole simulation and allows a smoother growth. The remeshing scheme keeps the mesh at a good quality during the large deformational simulation.

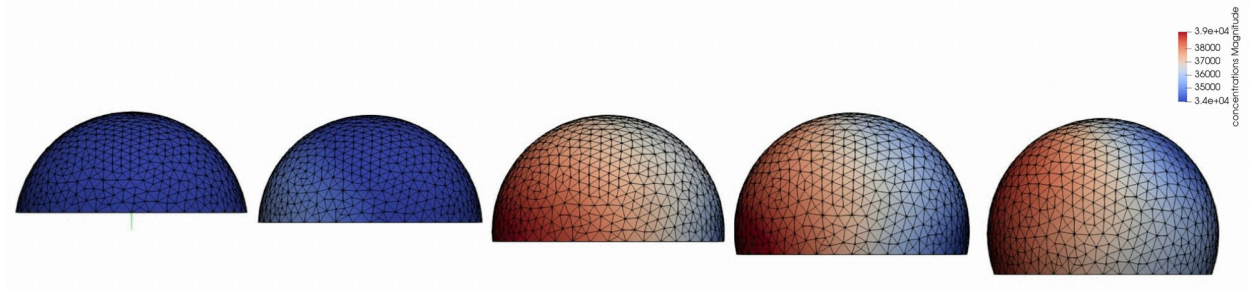


Figure 5.12 Simulation result of FEM model

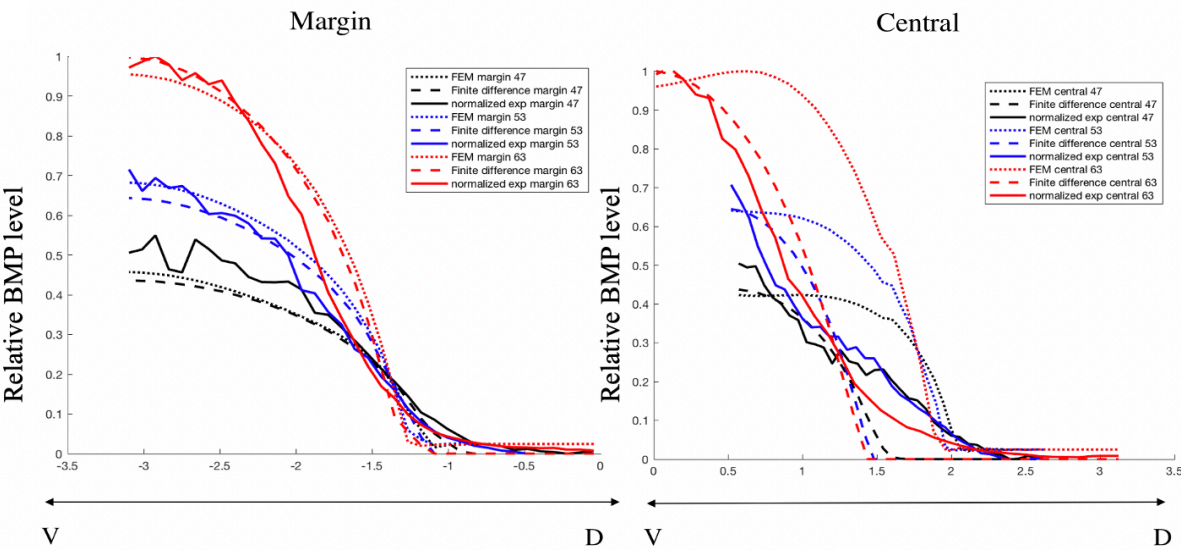


Figure 5.13 The BMP profile result comparison of FEM model vs Finite difference model

Figure 5.13 shows a comparison between the finite difference model result and the FEM model result under the same conditions and tested in an identical parameter set. The margin profiles of the BMP gradient between the two methods are very close; however, the profile on the central region has a relatively big gap at the animal region. This could be caused by the limitation on the approximation of the singularity happening on the pole for the finite difference scheme, or the difference of expression level interpolation method between simulation the finite difference model

and finite element model. Unless finite-difference model which only interpolates the expression level from the experimental dynamic map in each mesh layer growth one, the FEM model requests a spontaneous update of expression level for each single time increment, which could better in reflexing the real expression level at a specific stage.

5.3 Discussion

In this chapter, we introduced our newly developed framework with a growing domain finite element model to simulate the BMP regulation network in the early zebrafish embryo. Compare to our earlier approach, this model adapted in cell advective transport due to the large cell migration during epiboly over the diffusion-reaction system. We are interested in how the cellular movements impact the formation of gradients by contributing as an advective term whereby the morphogens are swept with the moving cells as they move vegetally. Quantitative whole-mount RNA scope data of BMP2b and phosphorylated-SMAD data are collected and analyzed precisely to test the hypotheses of the gradient formation mechanism in our model. We screened the unknown parameter space for WT embryos in processible parameter sets by using LHS sampling. The current WT screening result does match the P-SMAD data on the animal region and highly correlated to the mRNA expression map obtained through whole-mount RNA scope data. As the collection of late-stage embryo data through confocal image data was limited with the effective imaging range as the epiboly ongoing, we could not find the best fitting parameter set in our model reflex the P-SMAD level change spatiotemporally. However, we demonstrated the possible expression map that might reveal the real expression level. Further work requires of designing new experimental processes to cover this gap, for instants, imaging embryo data in multiple directions and assemble the partial image data to obtain the whole embryo data.

We also investigate the role of the domain changes and the advection in BMP gradient formation during epiboly by comparing the growing domain additive model to the fixed domain diffusion only model. The result show strong evidence that the cell movement driven advection during epiboly contributes to the formation of BMP gradient and it should not be ignored when modeling this system.

Investigating the underlining mechanisms in achieving the scaling invariance in the zebrafish embryo during DV patterning is one of the main questions we want to answer through our study. As the result shown in the earlier section, we currently not be able to identify the key

mechanism in keeping the robustness of intraspecies scaling invariance in the zebrafish embryo. However, by comparing the WT and Szl mutant embryo data in different embryo sizes, we found that the BMP gradient scaled in early stage (before 5.7hpf) though the relatively simple mechanism as the Chordin 'sink' the BMP ligand at dorsal region and shape the BMP gradient, Sizzled has no obvious contribution to the earlier stage scaling invariance. This corresponding to the recent result of Sizzled role of omission to the BMP gradient formation at blastula stage zebrafish embryo [51]. However, as the result show the large scaling error in the later stage, it seems this Chordin dominant regulation is not sufficient enough to maintain the robustness in the system. Nevertheless, the only presence of the Sizzled feedback mechanism is not enough to achieve it either. Another possible scenario is since we only screened the results over the P-SMAD5 profile until 6.7hpf, we are limited our constrain to the early gastrulation when Sizzled does not start to regulate BMP patterning. Further direction of investigating scale invariance in the gastrula stage should focus on the experimental data collection for the gastrula stage and adding multi-feedback mechanisms including but not limited to the role of Admp, Pinhead, and bmp1b, etc.

In the presence of BMP expression. The hill function described the feedback mechanism. B_0 represents the maximum level of BMP. To calculate B_0 in estimate the term K/B_0 , we have to calculate the maxima BMP level in pure expression level without exocellular regulates, which can be considering as a Chd/Szl double mutant. For estimating parameter k_{it} and k_{mt} , we have to calculate the maximum sizzled level in Chd mutant. This increases the intensively computational cost for screening the parameter space in our 3D finite element model in WT embryo. Therefore, in the current study, we have been limited by the computational abilities of screening a larger parameter space. Our solution might be trapped in a parametric region that favors the Szl omitted model. Our recently developed Neuron Network model may help in filling this gap. Future work in developing an accurate and reliable NN model to predict 3D simulation results will be one of our main directions to accomplish.

6 CONCLUSION AND FUTURE WORK

6.1 Conclusion

In summary, in this study, we present a three-dimensional (3D) growing domain mathematical modeling framework to simulate the BMP patterning and epiboly process during the gastrula stage zebrafish embryo, with both finite difference and finite element approaching. These models are useful to elucidate how different mechanisms and components work together in 3D to create and maintain the BMP gradient in the embryo.

We are interested in how the cellular movements impact the formation of gradients by contributing an advective term whereby the morphogens are swept with the moving cells as they move vegetally. Dynamic cell imaging data are used to quantify the cell movement during the epiboly. We evaluated the accuracy of the mesh updating compared to the advection caused by cell movement and its role in embryonic patterning. Quantitative whole-mount RNA scope data of *bmp2b*, *chordin*, *noggin*, *sizzled*, and phosphorylated-SMAD5 data are collected and analyzed precisely to test the hypotheses of the gradient formation mechanism in our model. We also present a novel approach of the Neuro Network model to accelerate the computationally intensive PDE simulations.

We investigate two major biology questions that can be tested with our FEM model. First how the cell movement drove advection contributes to the BMP gradient formation during epiboly. The result show strong evidence that advection contributes to the formation of BMP gradient and it should not be ignored when modeling this system. Finally, by investigating the mechanisms for intraspecies scaling invariance, we found that Sizzled may play no role in early-stage scaling invariance for the BMP gradient formation. However, there are two major limits in our current study that may need to address in future studies. First, the experimental data collection for the later stage embryo mRNA and P-Smad data. As our current imaging acquisition, it is extremely difficult to image the whole-mount embryo data for the embryo sample over 50% epiboly. New experimental or imaging procedures may need to be considered to obtain the important data at later gastrulation.

Finally, our goal is to develop a complete advection-diffusion-reaction model that incorporates all stages of zebrafish embryonic development data to investigate the mechanisms in

underlying BMP-driven DV patterning during epiboly. By combining the biophysics of epiboly with the regulatory dynamics of the BMP network, our current 3D growing domain model provides a framework in testing multiscale data-driven questions during zebrafish epiboly. Understanding dynamic changes in the BMP signaling in three-dimensional space over developmental timescales presents another intriguing avenue for future research. our model could be an open sesame to investigate multiscale signaling networks in early zebrafish embryo development, for instants dynamic scaling during embryonic stages, how the morphogen gradients scale within individual embryo as the size of the tissues and organisms are growing, furthermore, multi-objective optimization approaches can aid in evaluating competing mechanistic models of BMP gradient formation and deciphering the common principles between different species.

6.2 Future Work

6.2.1 Stochastic study of downstream gene transcription with BMP signaling regulation

For future studies, we plan to integrate with the stochastic study of downstream gene transcription with BMP signaling regulation. We have constructed a stochastic model of BMP receptor oligomerization to investigate the contribution of receptor-ligand interactions to positional information flow during BMP pattern formation. Experimental evidence indicates that BMP regulation of morphogenesis during development occurs via heterodimer signaling. Through deterministic modeling, we have demonstrated that the BMP heterodimer complex is not generated at higher steady-state levels than other tetrameric signaling complexes. Therefore, the privileged role of BMP heterodimer signaling during development arises from natural selection and is not an accident of kinetic rates.

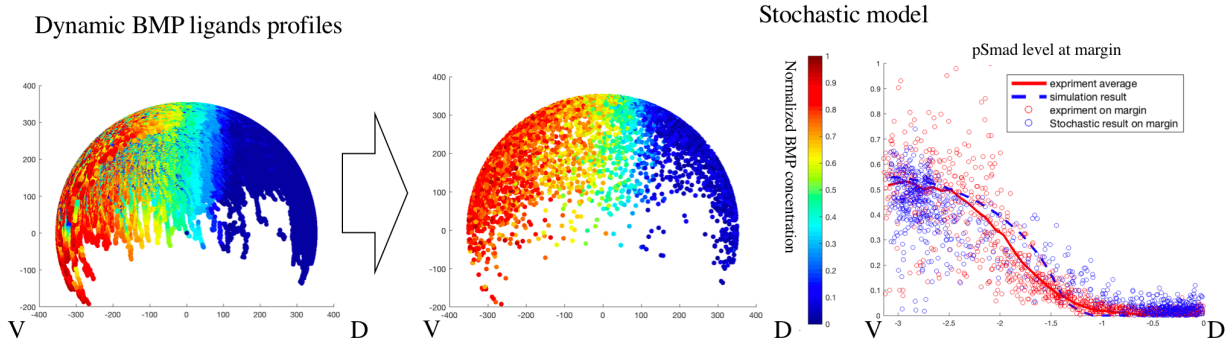


Figure 6.1. Integrate with the stochastic study of downstream gene transcription with BMP signaling regulation

Through computational modeling, we have identified several potential advantages for signaling through the BMP heterodimer over other tetrameric complexes. To evaluate these potential advantages in information transmission, we plan to integrate this stochastic model of BMP receptor oligomerization with a 3-D model of cell movement and ligand diffusion. With the finite element model results, we can have a dynamic map of BMP ligands level over the whole embryo. To obtain dynamic BMP ligands level for individual cells, we used the cell movement data from section 2.1. Time-dependent cell location data are analyzed from 3.5hpf to 8.2hpf (30% to 90% epiboly). Individual cell traces during this time range are obtained by running the provided code from this study. Integration of our stochastic model of receptor oligomerization with the model of cell movement and ligand diffusion will allow us to create an atlas of 'extrinsic noise' from receptor-ligand interactions during epiboly. Comparison of that extrinsic noise atlas, with real data on total BMP signaling noise, will allow us to understand the relative contribution of different sources of noise to the total noise of BMP signaling during development. Comparisons of these noise maps among different tetrameric complexes will confirm the evolutionary advantage of BMP heterodimer signaling.

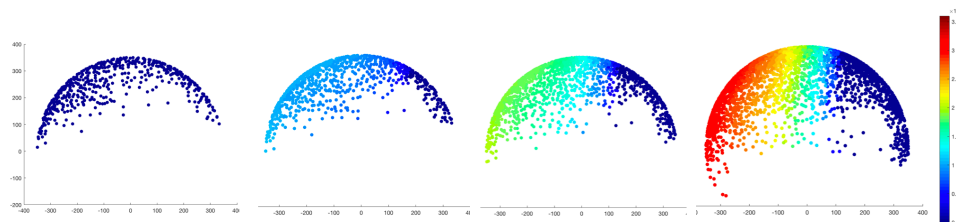


Figure 6.2. Cell level dynamic P-Smad level by the stochastic model

6.2.2 Combined with mechanics during epiboly

Early since Turing's ground-breaking work in morphogenesis, there have been enormous approaches tried to couple the mechanical growth in the organism with protein signaling network. Embryogenesis coupled with mechanical growth during the epiboly is another interesting area we want to further investigate. There is evidence shows that the enveloping cell layer releases (EVL) anisotropic tension which promoting tissue spreading during epiboly [165], thus, there is an increase of interest in how the stress and strain field responding to the cell movement during epiboly. As we already collected the cell movement map in epiboly and we have a growth domain mesh been constructed, we can calculate the mechanical equilibrium of the cell membrane with the stress and strain field using the finite element method. To handle the extrema deformation of the mesh, we represent the upgraded Lagrangian approach in this part of the study.

The total Lagrangian approach of the multiplicative decomposition model is widely employed for predicting residual stresses and morphologies of biological tissues due to growth. However, it relies on the assumption that the tissue is initially in a stress-free state, which conflicts with the observations that any growth state of biological tissue is under a significant level of residual stresses that help to maintain its ideal mechanical conditions. Also, the discrete equations are formulated with respect to the reference configuration. It requires a reference configuration that may not always be available, and numerically it requires a discretization with respect to the initial geometry, which might lead to extreme mesh distortion.

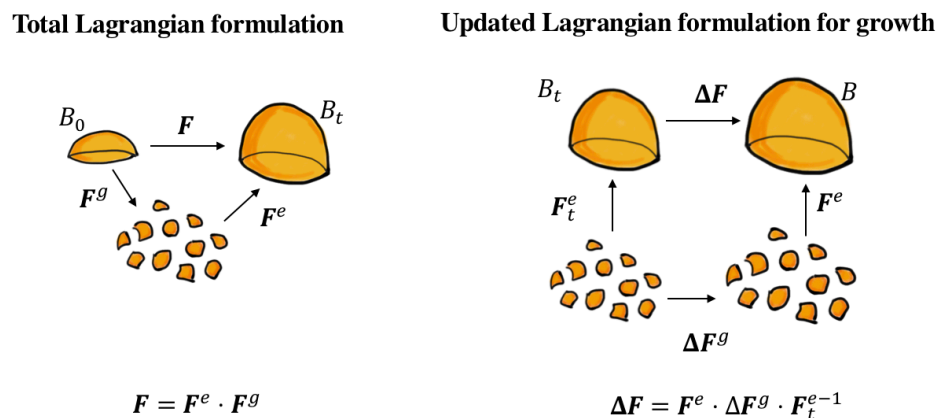


Figure 6.3. The multiplicative split of the deformation gradient to model growth

Here, we propose an updated Lagrangian approach, and the discrete equations are formulated in the current configuration, which is assumed to be the new reference configuration. The independent variables in the total Lagrangian approach are X and t . In the updated Lagrangian they are x and t which are with respect to the new reference configuration. In this study, we mainly track the stress-free state throughout the deformation and allows for remeshing to handle extreme deformations — similar work by Du, et al.[166] who ignore a reference configuration and consider a self-equilibrating stress field. Figure 6.3 illustrates the multiplicative split of the deformation gradient to model growth. The membrane stress of Neo-Hookean type from elastic deformation is

$$\boldsymbol{\sigma} = \mu \mathbf{b}_s^e + p \mathbf{I}$$

Where $\mathbf{b}_s^e = \mathbf{F}_s^e \mathbf{F}_s^{eT}$, is the left Cauchy Green deformation tensor of the elastic surface deformation, which comes from $\mathbf{F}^e = \mathbf{F}_s^e + \lambda_N \mathbf{n} \otimes \mathbf{N}$. The elastic deformation is a combination of a surface component and a normal stretch, and the normal stretch, in turn, satisfies incompressibility

$$\lambda_N = \frac{1}{\det(\mathbf{F}_s^e + \mathbf{n} \otimes \mathbf{N})}$$

And the pressure, p , enforces the vanishing of the normal stress $\sigma_n = 0$. For now, we ignore proper bending in \mathbf{F}_s^e , and instead consider a regularization term penalizing bending deformations based on Batty et al. which suggest simple bending energy to regularize the formulation and prevent buckling

$$E_b = \sum_{edges} \mu_b h^3 (\theta_{edge} - \bar{\theta}_{edge})^2 \frac{\bar{l}_{edge}}{\bar{l}_{edge}^*}, \bar{l}_{edge}^* = \frac{A}{3 \bar{l}_{edge}}$$

Growth is assumed in the surface only, and isotropic as

$$\Delta \mathbf{F}^g = \Delta \vartheta^g \mathbf{I}_s$$

And a constitutive equation for the growth increment is needed. For simplicity we first assume $\Delta \vartheta^g = \text{constant}$. Given the definition of growth and stress, the equilibrium problem for each increment is stated in the weak form in the configuration B_t .

$$\int_{B_t} \mathbf{S}_\Delta : \delta \mathbf{E}_\Delta dV + \int_{B_t} 2E_b \delta \theta_\Delta dV = 0$$

Where

$$\mathbf{S}_\Delta = J_\Delta \mathbf{F}_\Delta^{-1} \cdot \boldsymbol{\sigma} \cdot \mathbf{F}_\Delta^{-T}, \mathbf{E}_\Delta = \frac{1}{2}(\mathbf{F}_\Delta^T \cdot \mathbf{F}_\Delta - I), J_\Delta = \det(\mathbf{F}_\Delta)$$

We have already constructed the theoretical basis of this part of the study. However, we are experiencing a loss of strain tracking during the update of the configuration. A further plan has applied the effect of surface mapping to avoid the vanish of the strain during the simulation.

APPENDIX A. SUPPLEMENTAL TO CHAPTER 2

RNA staining using RNAscope and Image Acquisition

The embryos were fixed at the desired developmental stages with 4% PFA at RT for 4 hours or at 4°C for 24 hours and washed with 0.1% PBSTween 3 times at RT, each for 10 min. 20-30 embryos were separated into 1.5ml RNase free tube. The chorions were removed, and the embryos were gradually dehydrated from 25% methanol in PBST, 50% methanol in PBST, 75% methanol in PBST to 100% methanol, each for 5 min at RT. Store the embryos at -20 °C at least one day and up to 15 days. Two drops of Pretreat 3 (ACD, #320045) were added at RT for 15 min to permeate the embryos. Counterstaining of the probes using the RNAscope Fluorescent multiplex detection reagents (ACD, #320851). The user's manual (323100-USM) is available online, however, we made some modifications. We performed probe hybridization at 40 °C for 16 hours, and C2 probes need to be diluted by C1 probes. Detailed information about the probes is shown in Table 1. All wash steps were performed three times using 0.2x SSCT for ten minutes each time. DAPI was used to stain the nuclei at 4 °C overnight. We chose AltC for Amp4 in the staining kit.

Embryos were mounted in 1% low melting agarose on 35mm glass bottom microwell dishes (Matek, P35G-1.5-10-C). Whole-mounted embryos were imaged with a 20×/1.0 Plan-Apochromat water immersion lens (D = 0.17 M27 75 mm). *chd* mRNA was imaged by excitation at 555 nm wavelength. *bmp2b* and *nog* mRNA were imaged by excitation at 647 nm wavelength.

Table S1. RNA Probe Information

probe	ACD catalog No.	Accession No.	Target Region	Probe dilution
<i>Bmp2b-C2</i>	456471	NM_131360.1	336 - 1238	1:20
<i>Chd-C1</i>	440081	NM_130973.2	387 - 1302	1:1
<i>Nog-C2</i>	476651-C2	NM_130983.2	2 - 1328	1:50

APPENDIX B. SUPPLEMENTAL FIGURES/TABLE

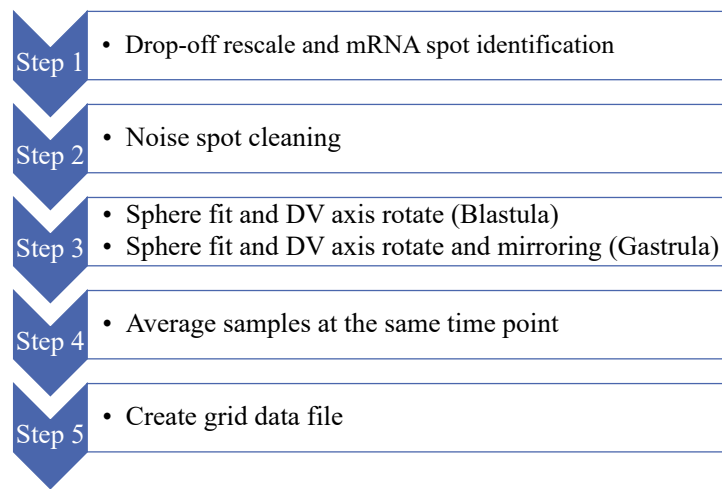
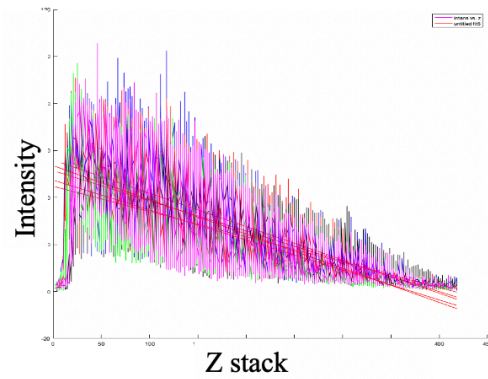
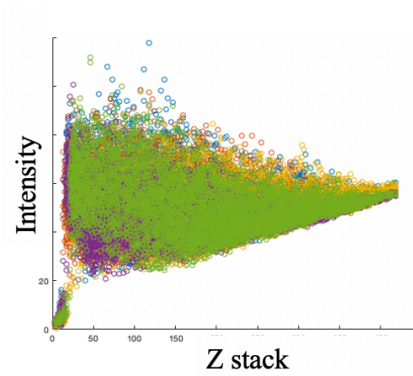


Figure S1. mRNA whole mount image processing flow

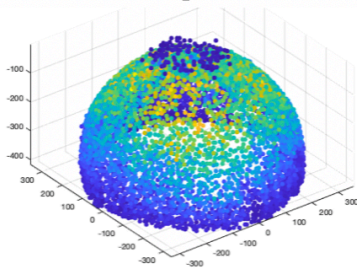
Original Nuclei intensity drop off through the depth stack of embryo



Corrected Nuclei intensity



Original Nuclei data used for measure the drop off level in 3D



$$\text{Correct intensity} = \text{Intensity} - z * \text{drop off gradient}$$

$$\text{drop off gradient} = 0.13$$

Figure S2. Drop off correction scheme

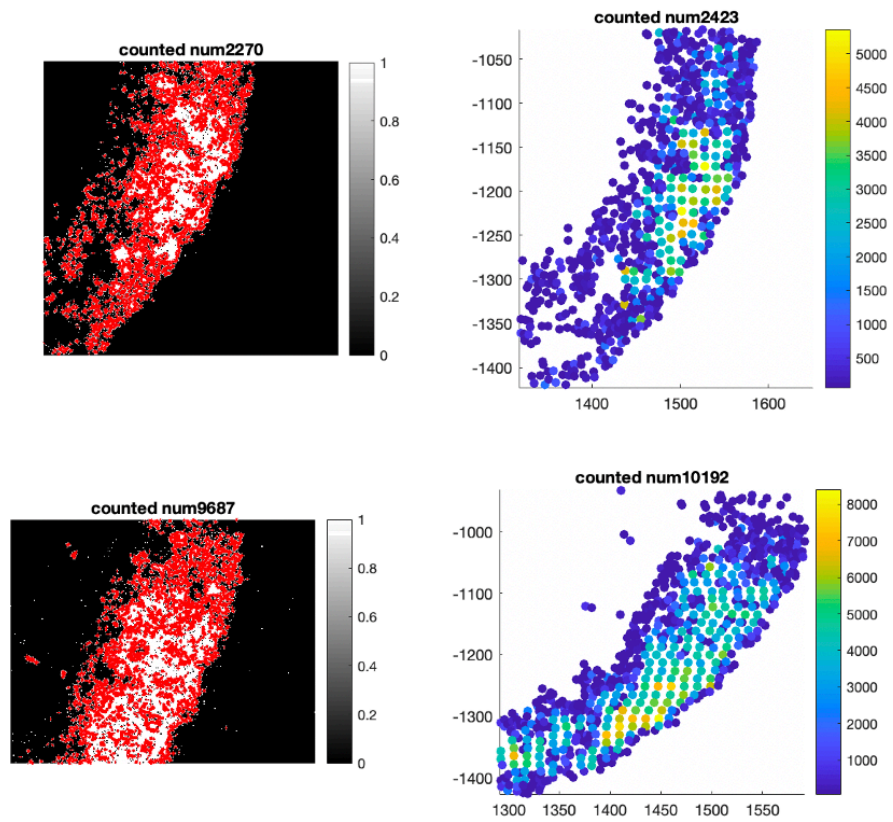


Figure S3. Big mRNA spots separation

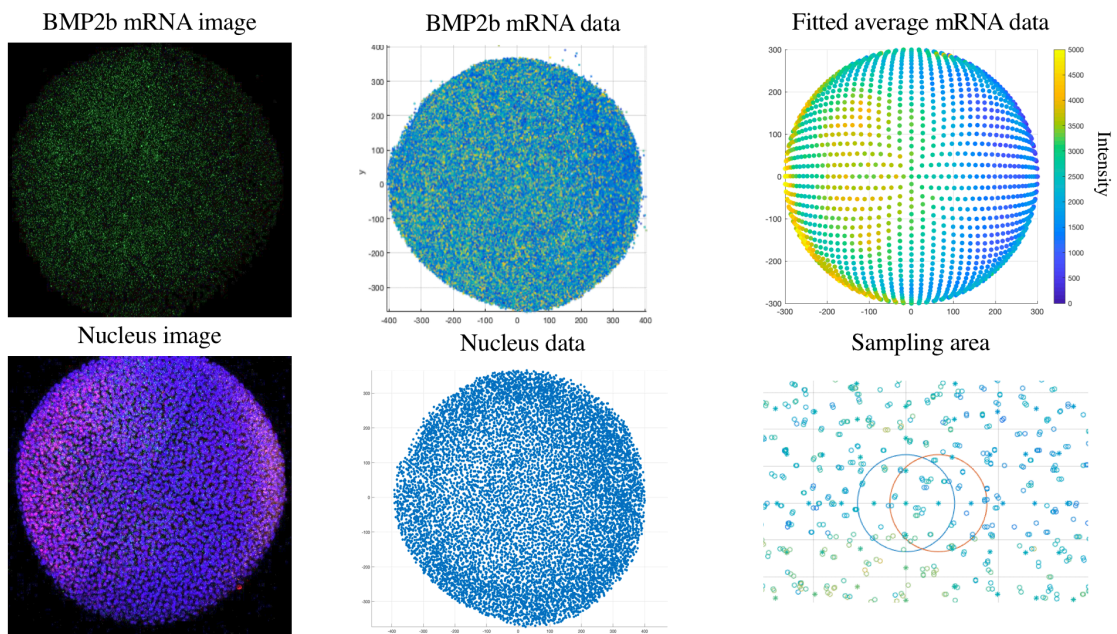


Figure S4. Data processing steps for BMP2b mRNA data

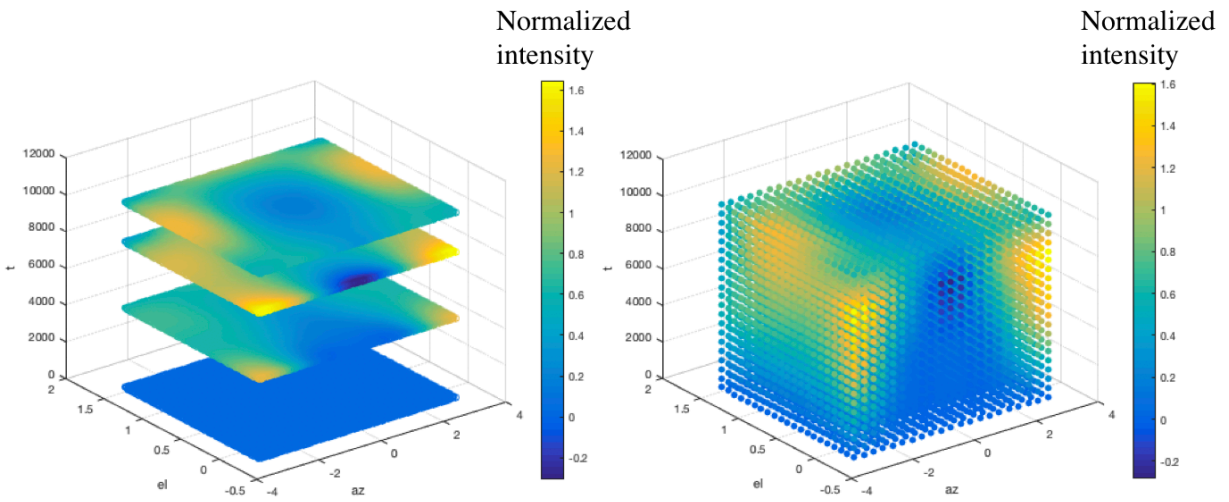


Figure S5. Dynamic map of BMP expression in 2D spherical coordinate

Table S2. Averaged Embryo number for mRNA in different stages

mRNA	4.7hpf	5.7hpf	6.3hpf	8hpf
<i>bmp2b</i>	5	4	3	4
<i>chd</i>	11	15	9	13
<i>nog</i>	3	4	3	5
<i>sizzled</i>	3	7	3	4

REFERENCES

- [1] P. K. Maini and M. Solursh, “Cellular mechanisms of pattern formation in the developing limb,” *Int. Rev. Cytol.*, vol. 129, pp. 91–133, 1991.
- [2] T. Lecuit and S. M. Cohen, “Dpp receptor levels contribute to shaping the Dpp morphogen gradient in the *Drosophila* wing imaginal disc,” *Development*, vol. 125, no. 24, pp. 4901–7, Dec. 1998.
- [3] S. N. Sansom and F. J. Livesey, “Gradients in the brain: the control of the development of form and function in the cerebral cortex,” *Cold Spring Harb. Perspect. Biol.*, vol. 1, no. 2, p. a002519, Aug. 2009.
- [4] C. A. Rushlow and S. Y. Shvartsman, “Temporal dynamics, spatial range, and transcriptional interpretation of the Dorsal morphogen gradient,” *Curr. Opin. Genet. Dev.*, vol. 22, no. 6, pp. 542–546, Dec. 2012.
- [5] F. B. Tuazon and M. C. Mullins, “Temporally coordinated signals progressively pattern the anteroposterior and dorsoventral body axes,” *Semin. Cell Dev. Biol.*, vol. 42, pp. 118–133, 2015.
- [6] A. M. Turing, “The Chemical Basis of Morphogenesis,” *Philos. Trans. R. Soc. B Biol. Sci.*, vol. 237, no. 641, pp. 37–72, Aug. 1952.
- [7] A. D. Lander, Q. Nie, and F. Y. . Wan, “Do Morphogen Gradients Arise by Diffusion?,” *Dev. Cell*, vol. 2, no. 6, pp. 785–796, 2002.
- [8] D. M. Umulis and H. G. Othmer, “The Role of Mathematical Models in Understanding Pattern Formation in Developmental Biology,” *Bull. Math. Biol.*, vol. 77, no. 5, pp. 817–845, 2015.
- [9] Leah Edelstein-Keshet, *Mathematical Models in Biology*, vol. XXXIII, no. 2. 2012.
- [10] J. A. Tucker, K. A. Mintzer, and M. C. Mullins, “The BMP Signaling Gradient Patterns Dorsoventral Tissues in a Temporally Progressive Manner along the Anteroposterior Axis,” *Dev. Cell*, vol. 14, no. 1, pp. 108–119, 2008.
- [11] E. M. De Robertis and Y. Sasai, “A common plan for dorsoventral patterning in Bilateria,” *Nature*, vol. 380, no. 6569, pp. 37–40, Mar. 1996.
- [12] S. A. Holley and E. L. Ferguson, “Fish are like flies are like frogs: Conservation of dorsal-ventral patterning mechanisms,” *BioEssays*, vol. 19, no. 4, pp. 281–284, Apr. 1997.
- [13] C. H. Hsu, Z. H. Wen, C. S. Lin, and C. Chakraborty, “The zebrafish model: use in studying cellular mechanisms for a spectrum of clinical disease entities,” *Curr Neurovasc Res*, vol. 4, no. 2, pp. 111–120, 2007.

- [14] C. B. Kimmel, W. W. Ballard, S. R. Kimmel, B. Ullmann, and T. F. Schilling, “Stages of embryonic development of the zebrafish,” *Dev Dyn*, vol. 203, no. 3, pp. 253–310, 1995.
- [15] S. E. Lepage and A. E. E. Bruce, “Zebrafish epiboly: Mechanics and mechanisms,” *Int. J. Dev. Biol.*, vol. 54, no. 8–9, pp. 1213–1228, 2010.
- [16] R. M. Warga and C. B. Kimmel, “Cell movements during epiboly and gastrulation in zebrafish,” *Development*, vol. 108, no. 4, pp. 569–580, 1990.
- [17] R. N. Wang *et al.*, “Bone Morphogenetic Protein (BMP) signaling in development and human diseases,” *Genes Dis.*, vol. 1, no. 1, pp. 87–105, 2014.
- [18] T. D. Mueller and J. Nickel, “Promiscuity and specificity in BMP receptor activation,” *FEBS Letters*, vol. 586, no. 14, pp. 1846–1859, 04-Jul-2012.
- [19] M. Nikaido, M. Tada, T. Saji, and N. Ueno, “Conservation of BMP signaling in zebrafish mesoderm patterning,” *Mech. Dev.*, vol. 61, no. 1–2, pp. 75–88, Jan. 1997.
- [20] N. Tiso, A. Filippi, S. Pauls, M. Bortolussi, and F. Argenton, “BMP signalling regulates anteroposterior endoderm patterning in zebrafish,” *Mech. Dev.*, vol. 118, no. 1, pp. 29–37, 2002.
- [21] H. Bauer *et al.*, “The type I serine/threonine kinase receptor Alk8/Lost-a-fin is required for Bmp2b/7 signal transduction during dorsoventral patterning of the zebrafish embryo,” *Development*, vol. 128, no. 6, pp. 849–58, Mar. 2001.
- [22] A. Hemmati-Brivanlou and G. H. Thomsen, “Ventral mesodermal patterning in *Xenopus* embryos: Expression patterns and activities of BMP-2 and BMP-4,” *Dev. Genet.*, vol. 17, no. 1, pp. 78–89, 1995.
- [23] H. Zou and L. Niswander, “Requirement for BMP signaling in interdigital apoptosis and scale formation,” *Science*, vol. 272, no. 5262, pp. 738–41, May 1996.
- [24] T. Kobayashi, K. M. Lyons, A. P. McMahon, H. M. Kronenberg, and G. R. Martin, “BMP signaling stimulates cellular differentiation at multiple steps during cartilage development,” *Proc. Natl. Acad. Sci.*, vol. 102, no. 50, pp. 18023–18027, Dec. 2005.
- [25] K. Miyazono, S. Maeda, and T. Imamura, “BMP receptor signaling: Transcriptional targets, regulation of signals, and signaling cross-talk,” *Cytokine and Growth Factor Reviews*, vol. 16, no. 3 SPEC. ISS. pp. 251–263, 2005.
- [26] J. A. Dutko and M. C. Mullins, “SnapShot: BMP Signaling in Development,” *Cell*, vol. 145, no. 4, pp. 636-636.e2, 2011.
- [27] B. Bragdon, O. Moseychuk, S. Saldanha, D. King, J. Julian, and A. Nohe, “Bone Morphogenetic Proteins: A critical review,” *Cell. Signal.*, vol. 23, no. 4, pp. 609–620, 2011.

- [28] Y. Shi and J. Massagué, “Mechanisms of TGF-beta signaling from cell membrane to the nucleus,” *Cell*, vol. 113, no. 6, pp. 685–700, 2003.
- [29] S. C. Little and M. C. Mullins, “Extracellular modulation of BMP activity in patterning the dorsoventral axis,” *Birth Defects Res. Part C Embryo Today Rev.*, vol. 78, no. 3, pp. 224–242, Sep. 2006.
- [30] S. C. Little and M. C. Mullins, “Extracellular modulation of BMP activity in patterning the dorsoventral axis,” *Birth Defects Res. Part C Embryo Today Rev.*, vol. 78, no. 3, pp. 224–242, Sep. 2006.
- [31] Z. Lele, J. Bakkers, and M. Hammerschmidt, “Morpholino phenocopies of the swirl, snailhouse, somitabun, minifin, silberblick, and pipetail mutations,” *genesis*, vol. 30, no. 3, pp. 190–194, Jul. 2001.
- [32] V. H. Nguyen, B. Schmid, J. Trout, S. A. Connors, M. Ekker, and M. C. Mullins, “Ventral and Lateral Regions of the Zebrafish Gastrula, Including the Neural Crest Progenitors, Are Established by *abmp2b/swirl* Pathway of Genes,” *Dev. Biol.*, vol. 199, no. 1, pp. 93–110, 1998.
- [33] M. C. Mullins *et al.*, “Genes establishing dorsoventral pattern formation in the zebrafish embryo: the ventral specifying genes,” *Development*, vol. 123, pp. 81–93, Dec. 1996.
- [34] H. Bauer, Z. Lele, G. J. Rauch, R. Geisler, and M. Hammerschmidt, “The type I serine/threonine kinase receptor *Alk8/Lost-a-fin* is required for *Bmp2b/7* signal transduction during dorsoventral patterning of the zebrafish embryo,” *Development*, vol. 128, no. 6, 2001.
- [35] M. Hild *et al.*, “The *smad5* mutation *somitabun* blocks *Bmp2b* signaling during early dorsoventral patterning of the zebrafish embryo,” *Development*, vol. 126, no. 10, pp. 2149–59, May 1999.
- [36] S. Fisher, S. L. Amacher, and M. E. Halpern, “Loss of *cerebum* function ventralizes the zebrafish embryo,” *Development*, vol. 124, no. 7, pp. 1301–11, Apr. 1997.
- [37] S. A. Connors, J. Trout, M. Ekker, and M. C. Mullins, “The role of *tolloid/mini fin* in dorsoventral pattern formation of the zebrafish embryo,” *Development*, vol. 126, no. 14, pp. 3119–30, Jun. 1999.
- [38] S. C. Little and M. C. Mullins, “Twisted gastrulation promotes BMP signaling in zebrafish dorsal-ventral axial patterning,” *Development*, vol. 131, no. 23, pp. 5825–35, Dec. 2004.
- [39] Y. Kishimoto, K. H. Lee, L. Zon, M. Hammerschmidt, and S. Schulte-Merker, “The molecular nature of zebrafish swirl: BMP2 function is essential during early dorsoventral patterning,” *Development*, vol. 124, no. 22, 1997.
- [40] B. Schmid *et al.*, “Equivalent genetic roles for *bmp7/snailhouse* and *bmp2b/swirl* in dorsoventral pattern formation,” *Development*, vol. 127, no. 5, 2000.

- [41] C. Kramer *et al.*, “Maternally Supplied Smad5 Is Required for Ventral Specification in Zebrafish Embryos Prior to Zygotic Bmp Signaling,” *Dev. Biol.*, vol. 250, no. 2, pp. 263–279, Oct. 2002.
- [42] M. Hammerschmidt *et al.*, “Dino and Mercedes, Two Genes Regulating Dorsal Development in the Zebrafish Embryo,” *Development*, vol. 123, pp. 95–102, Dec. 1996.
- [43] F. J. van Eeden *et al.*, “Mutations affecting somite formation and patterning in the zebrafish, *Danio rerio*,” *Development*, vol. 123, pp. 153–64, Dec. 1996.
- [44] M. K. Khokha, J. Yeh, T. C. Grammer, and R. M. Harland, “Depletion of Three BMP Antagonists from Spemann’s Organizer Leads to a Catastrophic Loss of Dorsal Structures,” *Dev. Cell*, vol. 8, no. 3, pp. 401–411, 2005.
- [45] S. Piccolo, Y. Sasai, B. Lu, and E. M. De Robertis, “Dorsoventral Patterning in *Xenopus*: Inhibition of Ventral Signals by Direct Binding of Chordin to BMP-4,” *Cell*, vol. 86, no. 4, pp. 589–598, 1996.
- [46] W. C. Smith and R. M. Harland, “Expression cloning of noggin, a new dorsalizing factor localized to the Spemann organizer in *Xenopus* embryos,” *Cell*, vol. 70, no. 5, pp. 829–840, 1992.
- [47] D. S. Wagner and M. C. Mullins, “Modulation of BMP Activity in Dorsal-Ventral Pattern Formation by the Chordin and Ogon Antagonists,” *Dev. Biol.*, vol. 245, no. 1, pp. 109–123, 2002.
- [48] O. Muraoka *et al.*, “Sizzled controls dorso-ventral polarity by repressing cleavage of the Chordin protein,” *Nat. Cell Biol.*, vol. 8, no. 4, pp. 329–338, Apr. 2006.
- [49] H. X. Lee, A. L. Ambrosio, B. Reversade, and E. M. De Robertis, “Embryonic dorso-ventral signaling: secreted frizzled-related proteins as inhibitors of tolloid proteinases,” *Cell*, vol. 124, no. 1, pp. 147–59, Jan. 2006.
- [50] H. Inomata, T. Shibata, T. Haraguchi, and Y. Sasai, “Scaling of Dorsal-Ventral Patterning by Embryo Size-Dependent Degradation of Spemann’s Organizer Signals,” *Cell*, vol. 153, no. 6, pp. 1296–1311, 2013.
- [51] F. B. Tuazon, X. Wang, J. L. Andrade, D. Umulis, and M. C. Mullins, “Proteolytic Restriction of Chordin Range Underlies BMP Gradient Formation,” *Cell Rep.*, vol. 32, no. 7, p. 108039, 2020.
- [52] E. M. De Robertis, “Spemann’s organizer and self-regulation in amphibian embryos,” *Nat. Rev. Mol. Cell Biol.*, vol. 7, no. 4, pp. 296–302, Apr. 2006.
- [53] V. Willot *et al.*, “Cooperative Action of ADMP- and BMP-Mediated Pathways in Regulating Cell Fates in the Zebrafish Gastrula,” *Dev. Biol.*, vol. 241, no. 1, pp. 59–78, 2002.

- [54] J. Garcia Abreu, C. Coffinier, J. Larraín, M. Oelgeschläger, and E. M. De Robertis, “Chordin-like CR domains and the regulation of evolutionarily conserved extracellular signaling systems,” *Gene*, vol. 287, no. 1, pp. 39–47, 2002.
- [55] D. Umulis, M. B. O’Connor, and S. S. Blair, “The extracellular regulation of bone morphogenetic protein signaling,” *Development*, vol. 136, no. 22, pp. 3715–28, Nov. 2009.
- [56] D. W. Walsh, C. Godson, D. P. Brazil, and F. Martin, “Extracellular BMP-antagonist regulation in development and disease: tied up in knots,” *Trends Cell Biol.*, vol. 20, no. 5, pp. 244–256, 2010.
- [57] M. Serpe *et al.*, “The BMP-Binding Protein Crossveinless 2 Is a Short-Range, Concentration-Dependent, Biphasic Modulator of BMP Signaling in *Drosophila*,” *Dev. Cell*, vol. 14, no. 6, pp. 940–953, 2008.
- [58] L. Zakin, C. A. Metzinger, E. Y. Chang, C. Coffinier, and E. M. De Robertis, “Development of the vertebral morphogenetic field in the mouse: Interactions between Crossveinless-2 and Twisted Gastrulation,” *Dev. Biol.*, vol. 323, no. 1, pp. 6–18, 2008.
- [59] A. L. Ambrosio, V. F. Taelman, H. X. Lee, C. A. Metzinger, C. Coffinier, and E. M. De Robertis, “Crossveinless-2 Is a BMP Feedback Inhibitor that Binds Chordin/BMP to Regulate *Xenopus* Embryonic Patterning,” *Dev. Cell*, vol. 15, no. 2, pp. 248–260, 2008.
- [60] E. M. De Robertis, M. Oelgeschläger, J. Larraín, and D. Geissert, “The evolutionarily conserved BMP-binding protein Twisted gastrulation promotes BMP signalling,” *Nature*, vol. 405, no. 6788, pp. 757–763, Jun. 2000.
- [61] D. Horbelt, A. Denkis, and P. Knaus, “A portrait of Transforming Growth Factor β superfamily signalling: Background matters,” *Int. J. Biochem. Cell Biol.*, vol. 44, no. 3, pp. 469–474, 2012.
- [62] Y. Yan *et al.*, “The BMP ligand Pinhead together with Admp supports the robustness of embryonic patterning,” *Sci. Adv.*, vol. 5, no. 12, 2019.
- [63] E. Klipp *et al.*, “Mathematical modeling of intracellular signaling pathways,” *BMC Neurosci.*, vol. 7, no. Suppl 1, p. S10, 2006.
- [64] S. Kondo and T. Miura, “Reaction-Diffusion Model as a Framework for Understanding Biological Pattern Formation,” *Science*, vol. 329, no. 5999, pp. 1616–1620, Sep. 2010.
- [65] A. D. Lander, “Morpheus Unbound: Reimagining the Morphogen Gradient,” *Cell*, vol. 128, no. 2, pp. 245–256, 2007.
- [66] L. Wolpert, “Positional information and the spatial pattern of cellular differentiation,” *J. Theor. Biol.*, vol. 25, no. 1, pp. 1–47, 1969.
- [67] O. Wartlick, A. Kicheva, and M. González-Gaitán, “Morphogen gradient formation,” *Cold Spring Harb. Perspect. Biol.*, vol. 1, no. 3, p. a001255, Sep. 2009.

- [68] D. M. Umulis, O. Shimmi, M. B. O'Connor, and H. G. Othmer, "Organism-Scale Modeling of Early *Drosophila* Patterning via Bone Morphogenetic Proteins," *Dev. Cell*, vol. 18, no. 2, pp. 260–274, 2010.
- [69] S. Bergmann *et al.*, "Pre-Steady-State Decoding of the Bicoid Morphogen Gradient," *PLoS Biol.*, vol. 5, no. 2, p. e46, Feb. 2007.
- [70] D. Umulis, M. B. O'Connor, and H. G. Othmer, "Robustness of Embryonic Spatial Patterning in *Drosophila melanogaster*," *Curr. Top. Dev. Biol.*, vol. 81, pp. 65–111, 2008.
- [71] J. Lewis, "From signals to patterns: space, time, and mathematics in developmental biology.," *Science*, vol. 322, no. 5900, pp. 399–403, Oct. 2008.
- [72] M. H. Swat, G. L. Thomas, J. M. Belmonte, A. Shirinifard, D. Hmeljak, and J. A. Glazier, "Chapter 13 – Multi-Scale Modeling of Tissues Using CompuCell3D," in *Methods in Cell Biology*, vol. 110, 2012, pp. 325–366.
- [73] S. Tanaka and Simon, "Simulation Frameworks for Morphogenetic Problems," *Computation*, vol. 3, no. 2, pp. 197–221, Apr. 2015.
- [74] P. Macklin, M. E. Edgerton, J. S. Lowengrub, and V. Cristini, "Discrete cell modeling," in *V. Cristini and J.S. Lowengrub, Multiscale Modeling of Cancer: An Integrated Experimental and Mathematical Modeling Approach*, .
- [75] P. Müller *et al.*, "Morphogen transport.," *Development*, vol. 140, no. 8, pp. 1621–38, Apr. 2013.
- [76] T. B. Kornberg and A. Guha, "Understanding morphogen gradients: a problem of dispersion and containment," *Curr. Opin. Genet. Dev.*, vol. 17, no. 4, pp. 264–271, 2007.
- [77] Y. Lou, Q. Nie, and F. Y. M. Wan, "Effects of Sog on Dpp-Receptor Binding.," *SIAM J. Appl. Math.*, vol. 65, no. 5, pp. 1748–1771, 2005.
- [78] A. Eldar, R. Dorfman, D. Weiss, H. Ashe, B.-Z. Shilo, and N. Barkai, "Robustness of the BMP morphogen gradient in *Drosophila* embryonic patterning," *Nature*, vol. 419, no. 6904, pp. 304–308, Sep. 2002.
- [79] W. Driever and C. Nüsslein-Volhard, "The bicoid protein determines position in the *Drosophila* embryo in a concentration-dependent manner," *Cell*, vol. 54, no. 1, pp. 95–104, 1988.
- [80] V. F. Irish and W. M. Gelbart, "The decapentaplegic gene is required for dorsal-ventral patterning of the *Drosophila* embryo.," *Genes Dev.*, vol. 1, no. 8, pp. 868–79, Oct. 1987.
- [81] D. Nellen, M. Affolter, and K. Basler, "Receptor serine/threonine kinases implicated in the control of *Drosophila* body pattern by decapentaplegic," *Cell*, vol. 78, no. 2, pp. 225–237, Jul. 1994.

- [82] Y.-C. Wang and E. L. Ferguson, “Spatial bistability of Dpp–receptor interactions during *Drosophila* dorsal–ventral patterning,” *Nature*, vol. 434, no. 7030, pp. 229–234, Mar. 2005.
- [83] D. M. Umulis, M. Serpe, M. B. O’Connor, and H. G. Othmer, “Robust, bistable patterning of the dorsal surface of the *Drosophila* embryo,” *Proc. Natl. Acad. Sci.*, vol. 103, no. 31, pp. 11613–11618, Aug. 2006.
- [84] D. M. Umulis, “The importance of geometry in mathematical models of developing systems,” *Curr Opin Genet Dev.*, vol. 22, no. 6, pp. 547–552, 2012.
- [85] J. Zinski, Y. Bu, X. Wang, W. Dou, D. Umulis, and M. C. Mullins, “Systems biology derived source-sink mechanism of bmp gradient formation,” *Elife*, vol. 6, pp. 1–32, 2017.
- [86] J. B. Hengenus, M. Gribskov, A. E. Rundell, C. C. Fowlkes, and D. M. Umulis, “Analysis of Gap Gene Regulation in a 3D Organism-Scale Model of the *Drosophila melanogaster* Embryo,” *PLoS One*, vol. 6, no. 11, p. e26797, Nov. 2011.
- [87] Y. T. Zhang, A. D. Lander, and Q. Nie, “Computational analysis of BMP gradients in dorsal-ventral patterning of the zebrafish embryo,” *J. Theor. Biol.*, vol. 248, no. 4, pp. 579–589, 2007.
- [88] J. Zinski, Y. Bu, X. Wang, W. Dou, D. Umulis, and M. C. Mullins, “Systems biology derived source-sink mechanism of BMP gradient formation,” *Elife*, 2017.
- [89] D. M. Umulis and H. G. Othmer, “Mechanisms of scaling in pattern formation.,” *Development*, vol. 140, no. 24, pp. 4830–43, 2013.
- [90] O. Wartlick *et al.*, “Dynamics of Dpp signaling and proliferation control.,” *Science*, vol. 331, no. 6021, pp. 1154–9, Mar. 2011.
- [91] D. M. Umulis and H. G. Othmer, “Mechanisms of scaling in pattern formation.,” *Development*, vol. 140, no. 24, pp. 4830–43, Dec. 2013.
- [92] Y. Huang and D. M. Umulis, “scale invariance of BMP signaling gradients in zebrafish.”
- [93] P. J. Keller, A. D. Schmidt, J. Wittbrodt, and E. H. K. Stelzer, “Reconstruction of zebrafish early embryonic development by scanned light sheet microscopy.,” *Science*, vol. 322, no. 5904, pp. 1065–1069, 2008.
- [94] R. B. Bird, W. E. Stewart, and E. N. Lightfoot, *Transport Phenomena, Revised 2nd Edition*. 2006.
- [95] Y. Shi and J. Massagué, “Mechanisms of TGF- β Signaling from Cell Membrane to the Nucleus,” *Cell*, vol. 113, no. 6, pp. 685–700, 2003.
- [96] B. Schmierer, A. L. Tournier, P. a Bates, and C. S. Hill, “Mathematical modeling identifies Smad nucleocytoplasmic shuttling as a dynamic signal-interpreting system.,” *PNAS*, vol. 105, no. 18, pp. 6608–13, 2008.

- [97] J. Zinski, F. Tuazon, Y. Huang, M. Mullins, and D. Umulis, “Imaging and Quantification of P-Smad1/5 in Zebrafish Blastula and Gastrula Embryos.”
- [98] H. Greenfeld, J. Lin Id, and M. C. Mullins Id, “The BMP signaling gradient is interpreted through concentration thresholds in dorsal-ventral axial patterning,” 2021.
- [99] A. Raj, P. van den Bogaard, S. A. Rifkin, A. van Oudenaarden, and S. Tyagi, “Imaging individual mRNA molecules using multiple singly labeled probes,” *Nat. Methods*, vol. 5, no. 10, pp. 877–879, 2008.
- [100] S. C. Little, M. Tikhonov, and T. Gregor, “Precise developmental gene expression arises from globally stochastic transcriptional activity,” *Cell*, vol. 154, no. 4, pp. 789–800, 2013.
- [101] Y. Oka and T. N. Sato, “Whole-mount single molecule FISH method for zebrafish embryo,” *Sci. Rep.*, vol. 5, pp. 1–8, 2015.
- [102] T. Gross-Thebing, A. Paksa, and E. Raz, “Simultaneous high-resolution detection of multiple transcripts combined with localization of proteins in whole-mount embryos,” *BMC Biol.*, vol. 12, no. 1, Aug. 2014.
- [103] F. Mueller *et al.*, “FISH-quant: Automatic counting of transcripts in 3D FISH images,” *Nat. Methods*, vol. 10, no. 4, pp. 277–278, 2013.
- [104] L. Carine Stapel *et al.*, “Automated detection and quantification of single RNAs at cellular resolution in zebrafish embryos,” *Dev.*, vol. 143, no. 3, pp. 530–539, 2016.
- [105] C. Bökel and M. Brand, “Generation and interpretation of FGF morphogen gradients in vertebrates,” *Curr. Opin. Genet. Dev.*, vol. 23, no. 4, pp. 415–422, Aug. 2013.
- [106] K. W. Rogers and A. F. Schier, “Morphogen Gradients: From Generation to Interpretation,” *Annu. Rev. Cell Dev. Biol.*, vol. 27, no. 1, pp. 377–407, Nov. 2011.
- [107] S. Dal-Pra, M. Fürthauer, J. Van-Celst, B. Thisse, and C. Thisse, “Noggin1 and Follistatin-like2 function redundantly to Chordin to antagonize BMP activity,” *Dev. Biol.*, vol. 298, no. 2, pp. 514–526, 2006.
- [108] D. O. Wagner *et al.*, “BMPs: from bone to body morphogenetic proteins.,” *Sci. Signal.*, vol. 3, no. 107, p. mr1, 2010.
- [109] S. Piccolo, E. Agius, B. Lu, S. Goodman, L. Dale, and E. M. De Robertis, “Cleavage of Chordin by Xolloid Metalloprotease Suggests a Role for Proteolytic Processing in the Regulation of Spemann Organizer Activity,” *Cell*, vol. 91, no. 3, pp. 407–416, Oct. 1997.
- [110] P. Blader, S. Rastegar, N. Fischer, and U. Strähle, “Cleavage of the BMP-4 antagonist chordin by zebrafish tolloid,” *Science (80-.)*, vol. 278, no. 5345, pp. 1937–1940, 1997.
- [111] A. von Bubnoff and K. W. Y. Cho, “Intracellular BMP Signaling Regulation in Vertebrates: Pathway or Network?,” *Dev. Biol.*, vol. 239, no. 1, pp. 1–14, 2001.

- [112] J.-Y. Luo, Y. Zhang, L. Wang, and Y. Huang, “Regulators and effectors of bone morphogenetic protein signalling in the cardiovascular system,” *J. Physiol.*, vol. 593, no. 14, pp. 2995–3011, Jul. 2015.
- [113] A. P. Pomreinke, G. H. Soh, K. W. Rogers, J. K. Bergmann, A. J. Bläßle, and P. Müller, “Dynamics of BMP signaling and distribution during zebrafish dorsal-ventral patterning,” *Elife*, vol. 6, no. Model 1, 2017.
- [114] N. Bhat, H.-J. Kwon, and B. B. Riley, “A gene network that coordinates preplacodal competence and neural crest specification in zebrafish,” *Dev. Biol.*, vol. 373, no. 1, pp. 107–117, Jan. 2013.
- [115] M. Hashiguchi and M. C. Mullins, “Anteroposterior and dorsoventral patterning are coordinated by an identical patterning clock,” *Development*, vol. 140, no. 9, pp. 1970–1980, May 2013.
- [116] E. Crampin, E. A. Gaffney, and P. K. Maini, “Reaction and Diffusion on Growing Domains: Scenarios for Robust Pattern Formation,” *Bull. Math. Biol.*, vol. 61, no. 6, pp. 1093–1120, Oct. 1999.
- [117] V. Klika and E. A. Gaffney, “History dependence and the continuum approximation breakdown: The impact of domain growth on Turing’s instability,” *Proc. R. Soc. A Math. Phys. Eng. Sci.*, vol. 473, no. 2199, p. 20160744, Mar. 2017.
- [118] A. Madzvamuse, P. K. Maini, and A. J. Wathen, “A Moving Grid Finite Element Method for the Simulation of Pattern Generation by Turing Models on Growing Domains,” *J. Sci. Comput.*, vol. 24, no. 2, 2005.
- [119] P. Fried and D. Iber, “Dynamic scaling of morphogen gradients on growing domains,” *Nat. Commun.*, vol. 5, p. 5077, Oct. 2014.
- [120] P. J. Keller, A. D. Schmidt, J. Wittbrodt, and E. H. K. Stelzer, “Reconstruction of zebrafish early embryonic development by scanned light sheet microscopy,” *Science*, vol. 322, no. 5904, pp. 1065–9, Nov. 2008.
- [121] J. Thibault, S. Bergeron, and H. W. Bonin, “ON FINITE-DIFFERENCE SOLUTIONS OF THE HEAT EQUATION IN SPHERICAL COORDINATES,” *Numer. Heat Transf.*, vol. 12, no. 4, pp. 457–474, Dec. 1987.
- [122] J. B. Hengeniuss, M. Gribskov, A. E. Rundell, and D. M. Umulis, “Making models match measurements: Model optimization for morphogen patterning networks,” *Seminars in Cell and Developmental Biology*, vol. 35. Elsevier Ltd, pp. 109–123, 01-Nov-2014.
- [123] M. Alber *et al.*, “Integrating machine learning and multiscale modeling—perspectives, challenges, and opportunities in the biological, biomedical, and behavioral sciences,” *npj Digit. Med.*, vol. 2, no. 1, pp. 1–11, Dec. 2019.
- [124] M. Sugiyama, *Introduction to Statistical Machine Learning*. Elsevier Inc., 2015.

- [125] J. Hastie, Trevor, Tibshirani, Robert, Friedman, *The Elements of Statistical Learning The Elements of Statistical Learning Data Mining, Inference, and Prediction, Second Edition*. 2009.
- [126] R. J. Williams, “Simple statistical gradient-following algorithms for connectionist reinforcement learning,” *Mach. Learn.*, 1992.
- [127] V. Mnih, K. Kavukcuoglu, D. Silver, and et al, “Human-level control through deep reinforcement learning,” *Nature*, 2015.
- [128] I. Goodfellow, Y. Bengio, and A. Courville, *Deep learning*. MIT press, 2016.
- [129] G. C. Y. Peng *et al.*, “Multiscale Modeling Meets Machine Learning: What Can We Learn?,” *Arch. Comput. Methods Eng.*, pp. 1–21, Feb. 2020.
- [130] Leah Edelstein-Keshet, *Mathematical Models in Biology*, vol. XXXIII, no. 2. 2012.
- [131] A. Krizhevsky, I. Sutskever, and G. E. Hinton, “Imagenet classification with deep convolutional neural networks,” *NIPS*, 2012.
- [132] D. E. Rumelhart, G. E. Hinton, and R. J. Williams, “Learning representations by back-propagating errors,” *Nature*, 1986.
- [133] J. Duchi, E. Hazan, and Y. Singer, “Adaptive subgradient methods for online learning and stochastic optimization,” *JMLR*, 2011.
- [134] G. Hinton, “Overview of mini-batch gradient descent.” 2012.
- [135] D. P. Kingma and J. L. Ba, “Adam: a method for stochastic optimization,” *ICLR*, 2015.
- [136] S. Sengupta *et al.*, “A review of deep learning with special emphasis on architectures, applications and recent trends,” *Knowledge-Based Syst.*, vol. 194, p. 105596, Apr. 2020.
- [137] X. Wang, Y. Zhao, and F. Pourpanah, “Recent advances in deep learning,” *International Journal of Machine Learning and Cybernetics*, vol. 11, no. 4. Springer, pp. 747–750, 01-Apr-2020.
- [138] S. Hochreiter and J. Schmidhuber, “Long short-term memory,” *Neural Comput.*, 1997.
- [139] Y. LeCun, L. Bottou, Y. Bengio, and P. Haffner, “Gradient-based learning applied to document recognition,” *Proc. IEEE*, 1998.
- [140] E. Mjolsness and D. DeCoste, “Machine learning for science: State of the art and future prospects,” *Science*, vol. 293, no. 5537. American Association for the Advancement of Science, pp. 2051–2055, 14-Sep-2001.
- [141] M. Rupp, A. Tkatchenko, K.-R. Muller, and O. A. von Lilienfeld, “Fast and accurate modeling of molecular atomization energies with machine learning,” *Phys. Rev. Lett.*, 2012.

- [142] V. L. Deringer *et al.*, “Realistic Atomistic Structure of Amorphous Silicon from Machine-Learning-Driven Molecular Dynamics,” *J. Phys. Chem. Lett.*, vol. 9, no. 11, pp. 2879–2885, Jun. 2018.
- [143] H. Chan *et al.*, “Machine Learning Classical Interatomic Potentials for Molecular Dynamics from First-Principles Training Data,” *Journal of Physical Chemistry C*, vol. 123, no. 12. American Chemical Society, pp. 6941–6957, 28-Mar-2019.
- [144] J. S. Smith, O. Isayev, and A. E. Roitberg, “ANI-1: an extensible neural network potential with DFT accuracy at force field computational cost,” *Chem. Sci.*, 2017.
- [145] Y. Wang, W.-L. Chao, D. Garg, B. Hariharan, M. Campbell, and K. Q. Weinberger, “Pseudo-LiDAR from Visual Depth Estimation: Bridging the Gap in 3D Object Detection for Autonomous Driving,” *CVPR*, 2019.
- [146] W. Ye, C. Chen, Z. Wang, I.-H. Chu, and S. P. Ong, “Deep neural networks for accurate predictions of crystal stability,” *Nat. Commun.*, 2018.
- [147] C. J. Pretorius, M. C. du Plessis, and C. B. Cilliers, “Simulating Robots Without Conventional Physics: A Neural Network Approach,” *J. Intell. Robot. Syst.*, 2013.
- [148] D. Nguyen-Tuong, M. Seeger, and J. Peters, “Model learning with local Gaussian process regression,” in *Advanced Robotics*, 2009, vol. 23, no. 15, pp. 2015–2034.
- [149] P. G. Breen, C. N. Foley, T. Boekholt, and S. P. Zwart, “Newton vs the machine: solving the chaotic three-body problem using deep neural networks,” *MNRAS*, 2019.
- [150] R. Wang, E. Kalnay, and B. Balachandran, “Neural machine-based forecasting of chaotic dynamics,” *Nonlinear Dyn.*, vol. 98, no. 4, pp. 2903–2917, Dec. 2019.
- [151] T. Hagge, P. Stinis, E. Yeung, and A. M. Tartakovsky, “Solving differential equations with unknown constitutive relations as recurrent neural networks,” Oct. 2017.
- [152] S. Wang *et al.*, “Massive computational acceleration by using neural networks to emulate mechanism-based biological models,” *Nat. Commun.*, 2019.
- [153] M. Raissi, P. Perdikaris, and G. E. Karniadakis, “Physics-informed neural networks: A deep learning framework for solving forward and inverse problems involving nonlinear partial differential equations,” *J. Comput. Phys.*, vol. 378, pp. 686–707, Feb. 2019.
- [154] D. Zhang, L. Guo, and G. E. Karniadakis, “Learning in modal space: Solving time-dependent stochastic PDEs using physics-informed neural networks,” *SIAM J. Sci. Comput.*, vol. 42, no. 2, pp. A639–A665, Mar. 2020.
- [155] S. Karumuri, R. Tripathy, I. Billionis, and J. Panchal, “Simulator-free solution of high-dimensional stochastic elliptic partial differential equations using deep neural networks,” *J. Comput. Phys.*, vol. 404, p. 109120, Mar. 2020.

- [156] T. Lee, S. Y. Turin, A. K. Gosain, I. Billionis, and A. Buganza Tepole, “Propagation of material behavior uncertainty in a nonlinear finite element model of reconstructive surgery,” *Biomech. Model. Mechanobiol.*, vol. 17, no. 6, pp. 1857–1873, Dec. 2018.
- [157] T. Lee, I. Billionis, and A. B. Tepole, “Propagation of uncertainty in the mechanical and biological response of growing tissues using multi-fidelity Gaussian process regression,” *Comput. Methods Appl. Mech. Eng.*, vol. 359, p. 112724, Feb. 2020.
- [158] M. J. Thompson, H. G. Othmer, and D. M. Umlis, “A Primer on Reaction-Diffusion Models in Embryonic Development,” in *eLS*, Chichester, UK: John Wiley & Sons, Ltd, 2018, pp. 1–16.
- [159] M. Pargett, A. E. Rundell, G. T. Buzzard, and D. M. Umlis, “Model-Based Analysis for Qualitative Data: An Application in *Drosophila* Germline Stem Cell Regulation,” *PLoS Comput. Biol.*, vol. 10, no. 3, 2014.
- [160] L. Li, X. Wang, M. C. Mullins, and D. M. Umlis, “Evaluation of BMP-mediated patterning in a 3D mathematical model of the zebrafish blastula embryo,” *J. Math. Biol.*, vol. 80, no. 1–2, pp. 505–520, Jan. 2020.
- [161] B. Zoph, V. Vasudevan, J. Shlens, and Q. V Le, “Learning Transferable Architectures for Scalable Image Recognition,” *CVPR*, 2018.
- [162] T. Brochu and R. Bridson, “Robust Topological Operations for Dynamic Explicit Surfaces,” *SIAM J. Sci. Comput.*, vol. 31, no. 4, pp. 2472–2493, Jan. 2009.
- [163] D. J. Benson, “Introduction to Arbitrary Lagrangian-Eulerian in Finite Element Methods,” *Arbitrary Lagrangian-Eulerian and Fluid-Structure Interaction*, John Wiley & Sons, Inc., Hoboken, NJ USA, pp. 1–50, 07-Mar-2013.
- [164] D. Iber, S. Tanaka, P. Fried, P. Germann, and D. Menshykau, “Simulating tissue morphogenesis and signaling,” *Tissue Morphog. Methods Protoc.*, no. 1, pp. 323–338, 2014.
- [165] P. Campinho, M. Behrndt, J. Ranft, T. Risler, N. Minc, and C.-P. Heisenberg, “Tension-oriented cell divisions limit anisotropic tissue tension in epithelial spreading during zebrafish epiboly,” *Nat. Cell Biol.*, vol. 15, no. 12, pp. 1405–1414, 2013.
- [166] Y. Du, C. Lü, W. Chen, and M. Destrade, “Modified multiplicative decomposition model for tissue growth: Beyond the initial stress-free state,” *J. Mech. Phys. Solids*, vol. 118, pp. 133–151, Sep. 2018.

PUBLICATIONS

Peer-Reviewed Journal Articles

1. **Li, L.**, Wang, X., Mullins, M.C., Umulis, D. Evaluation of BMP-mediated patterning in a 3D mathematical model of the zebrafish blastula embryo. *J. Math. Biol.* 80, 505–520 (2020). <https://doi.org/10.1007/s00285-019-01449-x>
3. Burzawa, L. and **Li, L.**, Wang, X., Buganza-Tepole, A., Umulis,D., "Acceleration of PDE-Based Biological Simulation Through the Development of Neural Network Metamodels." Accepted by *Current Pathobiology Reports* 2020
4. Wu, T., Wang, X., **Li, L.**, Bu, Y., Umulis, D. WaveletSEG: Automatic wavelet-based 3D nuclei segmentation and analysis for multicellular embryo quantification *bioRxiv* 2020.07.24.220285; doi: <https://doi.org/10.1101/2020.07.24.220285> (Submitted to *Scientific Reports*)

Selective Conference Podium Presentations and Poster Presentations

1. Li, L., Wang, X., Buganza-Tepole, A., Umulis, D., “Three-dimensional Finite Element Modeling of Dynamic BMP Gradient Formation in Zebrafish Embryonic Development”, 13th World Congress on Computational Mechanics 2018
2. **Li, L.**, Wang, X., Buganza-Tepole, A., Umulis,D.,. Integrating Dynamic Cell Imaging Data into Moving Mesh Finite Element Models of Developing Zebrafish Embryos. Cellular and Molecular Bioengineering Conference (CMBE) Jan 2020. Puerto Rico
3. **Li, L.**, Xu Wang, Tzu-Ching Wu, Mary C. Mullins, Adrian Buganza-Tepole, David Umulis. Three-dimensional finite element model of dynamic BMP- mediated patterning during epiboly in Zebrafish embryo. BMES Annual Meeting, October 2019, Philadelphia, Pennsylvania
4. **Li, L.**, Wang, X., Buganza-Tepole, A., Umulis,D.,, Three-Dimensional Finite Element Modeling of Dynamic BMP Gradient Formation in Zebrafish Embryonic Development. 2018 AIChE Annual Meeting. Oct 2018, Pittsburg
5. **Li, L.**, Wang, X., Buganza-Tepole, A., Umulis,D., Three-dimensional growing finite element model of BMP gradient formation during epiboly of the early zebrafish embryo. Annual Conference on Quantitative Approaches in Biology. November 16-17, 2018 at Northwestern University